

ANALYSIS OF THE DECAY $D^0 \rightarrow K_s^0 K^+ K^-$ WITH THE BESIII EXPERIMENT

PETER WEIDENKAFF

geboren am 21.07.1984 in Heidelberg

28. Juli 2016

Dissertation

zur Erlangung des Grades "Doktor der Naturwissenschaften"
am Fachbereich Physik, Mathematik und Informatik
der Johannes Gutenberg-Universität in Mainz



JOHANNES GUTENBERG
UNIVERSITÄT MAINZ

Peter Weidenkaff: *Analysis of the decay $D^0 \rightarrow K_S^0 K^+ K^-$ with the BESIII experiment*, Doktorarbeit, Mainz, 28. Juli 2016

MÜNDLICHE PRÜFUNG: 24. November 2016

FOREWORD

Humans have always observed their natural environment and tried to conclude the underlying mechanisms of phenomena. This human behavior is the cornerstone of physics. Physics is therefore strongly connected with the human abilities of curiosity, creativity and the ability to cooperate. Those abilities in basic forms also belong to other creatures too, but its extent is unique to humans.

The curious man investigates a phenomenon from an intrinsic impulse. This intrinsic impulse is important to mention since the solutions to a problem are sometimes not immediately advantageous. To find a explanation for a phenomenon, creativity is needed. Those explanations are called theories in the following. Many phenomena are too complex for an individual to solve them. Here the ability to cooperate among a large group of individuals and over large time scales is essential. In many cases the investigation of a phenomenon leads to new questions and so in iterative processes leads to a new, more detailed view of the world.

The philosophy of science deals with the Methodology of this process. If this process is rational and intersubjective we can call its outcome knowledge. In this term knowledge denotes the outcome of empirical science. Today, the widespread view how a problem can be solved undogmatically and rationally, has its root in the Critical rationalism of Karl Popper [1]. The basic assumption is that each scientific theory is fallible. Therefore the requirement is mandatory that a theory is disprovable by observations. The extent to which a theory is disprovable and how attempts to disprove it fail, is a measure for its quality. In contrast, the widespread view until the beginning of the 20th century was that a theory is accepted if it was confirmed for one or more special cases. One assumed that the common case can be proven by induction from a special case.

The change of paradigm in philosophy of science was triggered by the transition of classical physics to modern physics. Albert Einstein's theory of relativity (1905) superseded Newton's law of gravity which was experimentally proven for more than 200 years. Max Planck developed his theory of quantized radiation which also superseded previous ideas. From this, quantum mechanics was developed which is, combined with special relativity, the theoretical basis of the standard model of particle physics.

During the last century the previously mentioned iterative process of constructing or extending existing theories and its experimental falsification led to a model that describes nature extremely well. Today, the standard model of particle physics consists of six quarks and six leptons as fundamental particles. These are ordered into three generations which differ in mass. Each particle has its anti-particle which is identical except it has the opposite discrete quantum numbers. Three leptons, the neutrinos, are considered mass-less in the standard

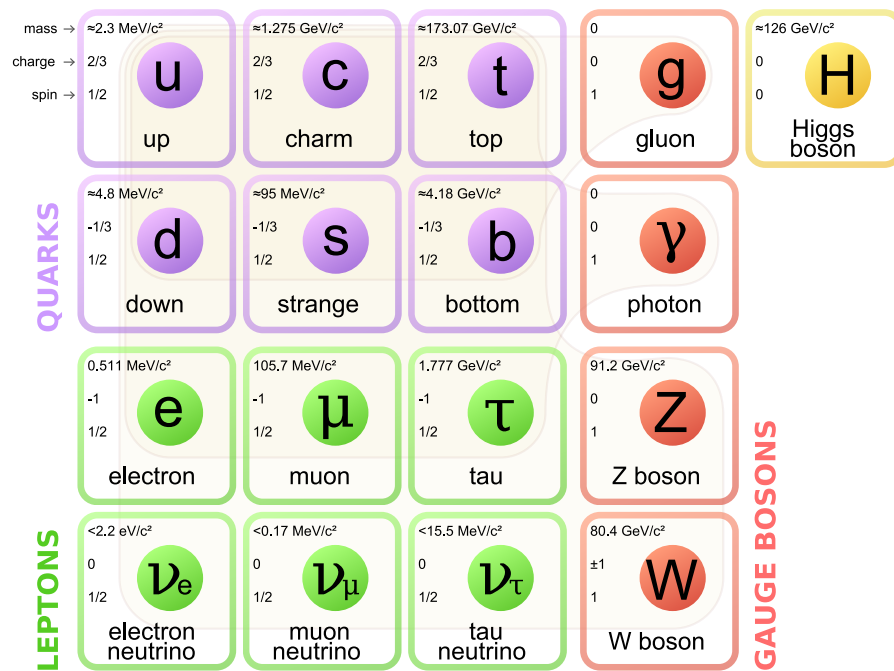


Figure 0.1: The Standard Model of elementary particles [4].

model, which is already disproven by experiment. All fundamental particles are fermions ¹.

The standard model incorporates three out of four fundamental interactions. Gravity is not included but, on common scales of particle physics, its effect is orders of magnitude smaller. The standard model is a local gauge theory with gauge bosons as exchange particles of the interactions. In the case of the strong interaction the gauge boson is the gluon, in the case of the electro-magnetic interaction the photon and the weak interaction is mediated via the massive W^\pm and Z^0 bosons. The gluon couples to color charge which is carried by the quarks only. The photon couples to the electric charge which includes all particles except the neutrinos, and W^\pm and Z^0 bosons couple to the weak charge.

The last constituent of the standard model which was experimentally proven in 2013, is the Higgs boson [2, 3]. The masses of particles and exchanges bosons are generated via the coupling to the scalar Higgs field with the Higgs boson as the exchange boson. All constituents of the standard model are illustrated in fig. 0.1.

Despite its success, the standard model contradicts to several observations. We already mentioned the finite neutrino mass which can not be incorporated within the model. From cosmology there is evidence for dark matter as well as dark energy, and our universe consists of almost no anti-matter. The standard model does not provide a candidate for a dark matter particle and it predicts a universe with almost the same amount of matter and anti-matter. Therefore it

¹ Particles with half-integer and integer spin are called fermions and bosons, respectively. In contrast to Bosons, Fermions obey the Pauli exclusion principle.

is justified to assume that the standard model is only the low-energy limit of a more comprehensive theory.

It is the challenge of experimental particle physics to reproduce those contradictions in a laboratory. This would make it possible to study the underlying mechanism in a controlled environment. Furthermore theoretical predictions based on the standard model need precise experimental input. The topic of this thesis is part of the latter challenge.

ABSTRACT

The study of mesons and baryons containing one or more charm quark is referred to as open charm physics. Mesons containing one charm and one light quark (u, d, s) are called D mesons. The lightest D mesons, D^0 and D^\pm , can only decay via a weak transition $c \rightarrow (d, s)$. The charm quark is together with the u and t quark a so-called ‘up-type’ quark. Since the u quark is the lightest quark and the t quark is too heavy to form bound states, D decays provide a unique laboratory to study ‘up-type’ quark transitions. The weak transition of bound states is also influenced by strong interaction effects which are important to understand, among others, the oscillation of D^0 and \bar{D}^0 . The precise measurement of branching fractions can help to improve the theoretical understanding in this field. Furthermore, D mesons are expected to decay via subsequent two-body decays, and in decays with three or more final state particles intermediate resonances can be studied. Due to the phase-space limitations of D decays so-called ‘light mesons’ can be observed.

The Beijing Electron-Positron collider II (BEPCII) is located at the Institute for High Energy Physics (IHEP) in Beijing. It provides collisions in the energy range from 2 GeV to 4.6 GeV. At an energy of 3.773 GeV the $\psi(3770)$ resonance is produced which predominantly decays to $D\bar{D}$. The BESIII detector has collected a data sample of 2931.8 pb^{-1} at this energy which corresponds to approximately $10.7 \times 10^6 D^0\bar{D}^0$ and $8.5 \times 10^6 D^+D^-$ decays. Each event contains two recoiling D decays in a almost background free environment. $D^0\bar{D}^0$ pair’s are furthermore produced in a quantum entangled state. This provides the possibility to ‘tag’ properties of one D decay from the reconstruction of the opposite D . In this work the flavour of the signal decay is obtained in this way.

The topic of this thesis is the study of the $D^0 \rightarrow K_s^0 K^+ K^-$ Dalitz plot using a flavour tagged data sample. Using an untagged event sample, the branching fraction is measured.

The Dalitz plot analysis is performed using 1856 ± 45 flavour tagged signal events with a purity of 96.4 %. We find that the Dalitz plot is well described by a set of 4 resonances: $a_0(980)^0$, $\phi(1020)$, $a_0(980)^+$ and $a_2(1320)^-$. We determine their magnitudes, phases and fit fractions. Furthermore we measure the $a_0(980)$ coupling to $K\bar{K}$ to be $g_{K\bar{K}} = (2.88 \pm 0.25 \text{ (stat.)} \pm 0.56 \text{ (sys.)}) \text{ GeV}$. The branching fraction is measured with 11384 ± 115 untagged signal decays and we obtain a value of $(4.45 \pm 0.05 \text{ (stat.)} \pm 0.18 \text{ (sys.)}) \times 10^{-3}$. The measurement yields a relative precision of 4.21 % which improves the current best measurement significantly. Both measurements are limited by the systematic uncertainty. As part of this work the reconstruction of displaced vertices is studied using $J/\psi \rightarrow \Lambda\bar{\Lambda}$ decays. A comparison of data and simulation yields no significant differences.

ZUSAMMENFASSUNG

Die Untersuchung von Mesonen und Baryonen, die mindestens ein Charm-Quark enthalten, wird als (offene) Charm-Physik bezeichnet. Mesonen, die sowohl ein c als auch ein leichtes quark (u, d, s) enthalten, werden als D Mesonen bezeichnet. Die leichtesten Mesonen, D^0 und D^\pm , können nur durch den schwachen Übergang $c \rightarrow (d, s)$ zerfallen. Das Charm-Quark ist zusammen mit dem u und t Quark ein sogenanntes „up-type“ Quark. Zerfälle von Charm-Mesonen und Baryonen bieten die einzige Möglichkeit Quarkübergänge dieser Art zu studieren. Der schwache Zerfall gebundener Zustände wird durch Effekte der starken Wechselwirkung beeinflusst, welche, unter anderem, für das Verständnis der Oszillation von D^0 und \bar{D}^0 wichtig sind. Die präzise Vermessung von Verzweigungsverhältnissen kann helfen Unsicherheiten in den theoretischen Vorhersagen zu reduzieren. Desweiteren ist es möglich in D Zerfällen Zwischenzustände zu beobachten. In dem zugänglichen Massenbereich können sogenannte „leichte Mesonen“ beobachtet werden.

Der Beijing Electron Positron Collider (BEPCII) wird am Institut für Hochenergiephysik (IHEP) in Peking in einem Energiebereich zwischen 2 GeV und 4.6 GeV betrieben. Bei einer Schwerpunktsenergie von 3.773 GeV wird die $\psi(3770)$ Resonanz erzeugt, welche fast ausschließlich in ein Paar von D Mesonen zerfällt. Der bisher aufgezeichnete Datensatz bei dieser Energie von 2931.8 pb^{-1} entspricht ungefähr $10.7 \times 10^6 D^0 \bar{D}^0$ und $8.5 \times 10^6 D^+ D^-$ Zerfällen in einer nahezu untergrundfreien Umgebung. $D^0 \bar{D}^0$ Paare werden darüber hinaus in einem Zustand der Quantenverschränkung erzeugt, welche es ermöglicht Rückschlüsse vom Zerfall eines Mesons auf den Zerfall des anderen zu ziehen. Dies wird in dieser Arbeit zur Bestimmung der Teilchenart genutzt.

Im Rahmen dieser Arbeit wird der Zerfall $D^0 \rightarrow K_S^0 K^+ K^-$ untersucht. Das Dalitz-Diagramm wird analysiert und das Verzweigungsverhältnis wird gemessen.

Die Analyse des Dalitz-Diagramms erfolgt anhand von $1856 \pm 45 D^0$ Signalzerfällen mit einer Reinheit von 96.4%. Es stellt sich heraus, dass die Substruktur durch ein Model mit vier Resonanzen gut beschrieben werden kann: $a_0(980)^0$, $\phi(1020)$, $a_0(980)^+$ und $a_2(1320)^-$. Wir bestimmen Magnitude, Phase sowie die partiellen Verzweigungsverhältnisse. Außerdem wird für die Kopplungsstärke des $a_0(980)$ im Kanal $K\bar{K}$ ein Wert von $g_{K\bar{K}} = (2.88 \pm 0.25 \text{ (stat.)} \pm 0.56 \text{ (sys.)}) \text{ GeV}$ bestimmt. Das Verzweigungsverhältnis wird durch 11384 ± 115 Signalzerfälle gemessen. Wir bestimmen einen Wert von $(4.45 \pm 0.05 \text{ (stat.)} \pm 0.18 \text{ (sys.)}) \times 10^{-3}$. Mit einer relativen Präzision von 4.21% übertrifft diese Messung bisherige Messungen deutlich. Beide Messungen sind durch systematische Unsicherheiten geprägt. Außerdem wird im Rahmen dieser Arbeit die Rekonstruktion von Teilchenzerfällen mit signifikanter Fluglänge, im Zerfall $J/\psi \rightarrow \Lambda \bar{\Lambda}$ untersucht. Der Vergleich von Daten und Simulation zeigt keine signifikanten Unterschiede.

CONTENTS

i	INTRODUCTION	1
1	MESON SPECTROSCOPY	3
1.1	The Constituent quark model	3
1.2	Light scalar meson spectroscopy	4
2	CHARM PHYSICS	7
3	MOTIVATION FOR THE ANALYSIS OF $D^0 \rightarrow K_S^0 K^+ K^-$	9
3.1	Previous measurement	10
ii	THEORY	13
4	PARTICLE INTERACTIONS	15
4.1	The isobar model	15
4.2	Mandelstam variables	15
4.2.1	Kinematics of two-particle vertices	16
4.2.2	Scattering and helicity angle	17
4.3	The Dalitz plot	18
4.4	Transition amplitude	19
4.4.1	Probability conservation and causality	21
4.5	The helicity formalism	21
4.5.1	Introduction to rotation operators and Wigner D-matrix	22
4.5.2	Plane-wave helicity states	24
4.5.3	Spherical-wave helicity states	24
4.5.4	Parity	25
4.6	Partial wave expansion	26
4.6.1	Two-body scattering	27
4.6.2	Two-body decay	28
5	RESONANCES	31
5.1	What is a resonance?	31
5.2	The Breit-Wigner ansatz	33
5.3	The Flatté formalism	35
5.4	Blatt-Weisskopf barrier factors	36
6	QUANTUM ENTANGLED $D^0 \bar{D}^0$ DECAYS	39
6.1	Decay amplitude of entangled $D^0 \bar{D}^0$ pairs	40
6.2	Branching-fractions in entangled $D^0 \bar{D}^0$ decays	41
7	AMPLITUDE MODEL FOR $D^0 \rightarrow K_S^0 K^+ K^-$	45
iii	THE BESIII EXPERIMENT	49
8	THE BEPCII STORAGE RING	51
8.1	Synchrotron Radiation Facility	52
9	THE BESIII DETECTOR	53
9.1	Multi-wire drift chamber	53
9.2	Time-of-flight system	55

9.2.1	Time resolution	55
9.3	Electromagnetic calorimeter	56
9.4	Muon system	57
10	DATA ANALYSIS AT BESIII	59
10.1	Simulation	59
10.2	Reconstruction	60
10.2.1	Event start time	60
10.2.2	Charged tracks	60
10.2.3	Electromagnetic showers	61
10.3	Analysis	61
10.3.1	Kinematic fitting	62
10.3.2	Particle identification	62
10.3.3	D tagging	63
10.4	Data samples	65
10.5	Partial wave analysis framework	65
iv	ANALYSIS OF THE DECAY $D^0 \rightarrow K_S^0 K^+ K^-$	67
11	EVENT RECONSTRUCTION AND SELECTION	69
11.1	Monte-Carlo simulation	69
11.2	Reconstruction and selection of the final state particles	71
11.2.1	Charged kaons and pions	71
11.2.2	Photons	73
11.2.3	π^0 and η candidates	73
11.2.4	K_S^0 candidates	73
11.3	Tag candidates	73
11.4	Signal candidates	74
11.4.1	Signal region	75
11.4.2	Multivariate discrimination	75
11.5	Background	77
11.6	Signal and background models	78
12	DALITZ PLOT ANALYSIS	81
12.1	Signal purity	82
12.2	Background	83
12.3	Likelihood function	85
12.4	Efficiency correction	86
12.5	Goodness-of-fit	88
12.5.1	Point-to-Point dissimilarity test	89
12.5.2	Likelihood ratio test	91
12.6	Resonances	93
12.7	Model selection	96
12.7.1	Penalty term	96
12.8	Systematics	99
12.8.1	Background	99
12.8.2	Amplitude model	99
12.8.3	Monte-Carlo simulation	100
12.8.4	External parameters	100

12.8.5	Fitting procedure	100
12.9	Result	102
13	BRANCHING-FRACTION MEASUREMENT	107
13.1	Correction for quantum entangled $D^0\bar{D}^0$ decays	108
13.2	Signal yield	108
13.3	Efficiency correction	109
13.4	Validation	110
13.5	Study of systematic uncertainties	111
13.5.1	Mass resolution	111
13.5.2	Substructure of $K_S^0 K^+ K^-$	111
13.5.3	Signal and background models	112
13.5.4	Selection variables	112
13.5.5	K_S^0 reconstruction efficiency	113
13.5.6	Track reconstruction and particle identification	113
13.5.7	Overview of systematic uncertainties	114
13.6	Result	114
V	SUMMARY AND OUTLOOK	117
VI	APPENDIX	121
A	THEORY	123
A.1	Properties of the Wigner D-matrix	123
A.2	The optical theorem	124
A.3	The mixing parameter γ	124
B	ANALYSIS OF THE DECAY $D^0 \rightarrow K_S^0 K^+ K^-$	127
B.1	Signal and background models	127
B.2	Tagged signal fraction for the Dalitz plot analysis	127
B.3	Statistical uncertainty of fit fractions	128
B.4	Efficiency differences between data and simulation	128
B.5	Systematic uncertainties of the Dalitz plot analysis	131
B.6	Dalitz plot fit result	131
B.7	Untagged signal yield for branching fraction measurement	131
C	SYSTEMATIC STUDIES OF DISPLACED VERTEX RECONSTRUCTION	137
C.1	Introduction	137
C.2	Selection	139
C.3	Branching fraction	143
C.4	Reconstruction efficiency	144
C.5	Conclusion	147
	BIBLIOGRAPHY	151

Part I

INTRODUCTION

The main scope of this thesis concerns the analysis of the decay $D^0 \rightarrow K_s^0 K^+ K^-$. The physics interest of this analysis is on the one hand a better understanding of light mesons, in particular light scalar mesons, that occur in the substructure of the decay, and on the other hand a contribution to a better theoretical understanding of the D^0 meson, by a precise measurement of its branching fraction to $K_s^0 K^+ K^-$.

In the following we will give an introduction to meson spectroscopy (chapter 1) and charm physics (chapter 2). In part ii we deal with the theoretical background which is necessary to describe the decay. Chapter 7 summarizes the relevant formula. The BESIII experiment is introduced in part iii. Part iv describes the analysis which consists of the analysis of the Dalitz plot (chapter 12) and the branching fraction measurement (chapter 13). Finally we conclude the results and give an outlook in part v.

MESON SPECTROSCOPY

The pion was introduced in 1935 [5] as an exchange particle of the force between nucleons. In the following time, a large number of mesons and baryons were discovered and groups of particles could be organized according to their quantum numbers to resemble the symmetry of the underlying interaction. The nonets of pseudo-scalar and vector mesons arising from this grouping are shown in figs. 1.1 and 1.2. From the mid 1970s on Quantum Chromodynamics (QCD) is accepted as the theory of the strong interaction and mesons were identified as the bound states of QCD. The symmetries that were found before and the success of Quantum Electrodynamics (QED) were the basis for QCD. The theoretical prediction of bound states and their properties is difficult in QCD, yet without the knowledge of its bound states a theory cannot be considered to be complete. The experimental search for bound states and the measurement of their properties are the goals of hadron (meson and baryon) spectroscopy.

1.1 THE CONSTITUENT QUARK MODEL

Since an a priori prediction from QCD is difficult, a phenomenological model is used to predict the meson spectrum and compare it with experiment. The constituent quark model was proposed long before the success of QCD. It assumes that mesons and baryons consist of constituent objects, so-called (valence-) quarks. Hence mesons are bound states of quark and anti-quark. The spins of the quarks can couple to a total spin s of zero and one, and the quarks can have orbital angular momentum l . The quantum numbers of the quark system are:

- **Meson spin:** $|l - s| \leq J \leq |l + s|$
- **Parity:** $P = (-1)^{l+1}$
- **Charge parity:** $C = (-1)^{l+s}$

Not all quantum numbers are allowed within this model. Quantum numbers like $J^{PC}=0^{--}, 0^{+-}, 1^{-+}, 2^{+-}, 3^{-} \dots$ are termed as ‘exotic’ because they cannot be accommodated by the constituent quark model. From the light quarks u, d and s , nine $q\bar{q}$ combinations can be constructed and grouped into an octet and a singlet. If the $q\bar{q}$ spins are anti-aligned we find the pseudo-scalar meson nonet of fig. 1.1 and in case of aligned spins the vector meson nonet of fig. 1.2. In both cases the $q\bar{q}$ pair does not have orbital angular momentum.

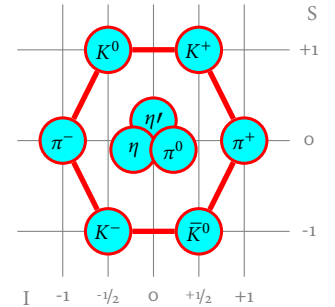


Figure 1.1: Pseudo-scalar meson nonet.

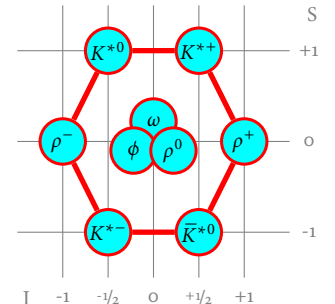


Figure 1.2: Vector meson nonet. K^* denotes the K^* (892).

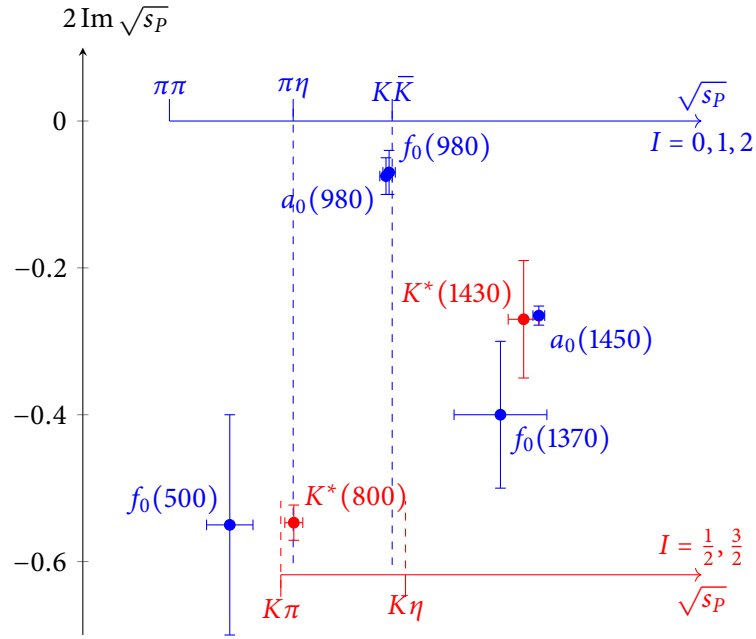


Figure 1.3: Overview of the light scalar meson spectrum. We plot the experimental average values provided by the particle data group [7]. The resonance pole is parametrized as $\sqrt{s_P} = M_R + i\Gamma_R/2$. We assume that the Breit-Wigner parameters and the pole parameters are identical which is certainly not true for some resonances e. g. $f_0(500)$ and $K^*(800)$. With this assumption the imaginary part of the pole position is linked to the resonance width via $\Gamma = 2 \text{Im}(\sqrt{s_P})$. The integer isospin states are shown in blue and the half-integer isospin states in red. Units are in GeV. Note that some results shown here are only rough estimates from the particle data group.

The goal is to experimentally map out the spectrum of QCD bound states and to search for states with ‘exotic’ quantum numbers that cannot be explained in the constituent quark model. A candidate for such a state is the $\pi_1(1600)$ which was observed by the COMPASS experiment [6]. Quantum numbers of $J^{PC} = 1^{-+}$ were observed.

1.2 LIGHT SCALAR MESON SPECTROSCOPY

The meson spectrum below 2 GeV is referred to as light meson spectrum. In this mass range mesons consist of u, d and s quarks. The spectra for pseudo-scalar, vector and tensor mesons are rather well-known, in contrast to the spectrum for scalar mesons ($J^P = 0^+$). In the following we give a short overview of the resonances which are observed in this region. Since this chapter focuses mainly on the general understanding, we also include some results that are not free of doubt. We follow the overview from the particle data group [7, pp. 784-791].

The light scalar meson spectrum is shown in fig. 1.3. Since we are dealing with the strong interaction, isospin is a good symmetry and we can divide the spectrum into integer isospin states ($\pi\pi, \pi\eta$ and $K\bar{K}$) and half-integer isospin

states ($K\pi$ and $K\eta$). The range up to 2 GeV involves several thresholds which makes the investigations difficult since close to thresholds the resonance shape deviates significantly from the expected Breit-Wigner form and its mass and width parameter are different from the pole parameters (in fig. 1.3 we assume that both are identical). The nature of most states in the light scalar meson spectrum is not unequivocally proven since on the one hand many states are close to thresholds and on the other hand the masses of the observed states cannot be calculated within a constituent quark model. There are several models that go beyond the constituent quark model to explain the observed spectrum of 0^+ states: four-quark states, meson-meson bound states or scalar glue balls. These states are allowed within QCD, and therefore they are expected to exist somewhere. Note that all these states are compatible with quantum number 0^+ . Since states with the same quantum numbers are expected to convert to each other (if kinematically allowed) those states most likely consist of a combination of several models.

Close to the lowest thresholds $\pi\pi$ and $K\pi$ the broad resonances $f_0(500)$ and the $K^*(800)$ are located. Their widths is expected to be larger than 500 MeV. Many experiments have seen them, yet the quantitative results spread over a wide range. Just below the $K\bar{K}$ threshold, the $a_0(980)$ and the $f_0(980)$ appear. The mass is rather well known but the experimental results on the width are not consistent. Above the $K\bar{K}$ threshold the $f_0(1370)$ and the $a_0(1450)$ show up in the integer spin spectrum and the $K^*(1430)$ shows up in the spectrum of half-integer spin.

A possible interpretation is that the states $K^*(800)$, $f_0(500)$, $f_0(980)$ and $a_0(980)$ form a nonet as shown in fig. 1.4. This could be a nonet of states that cannot entirely be explained in the constituent quark model.

The light quark spectrum offers various candidates for new resonant states beyond the constituent quark model. Unfortunately those broad and overlapping resonances in combination with several thresholds make it difficult to study an isolated state and investigate its nature. The search within the charmonium region above $\sqrt{s} = 3$ GeV seems to be more promising. In this region BESIII discovered the $Z_c(3900)^\pm$ in the reaction $e^+e^- \rightarrow J/\psi \pi^+ \pi^-$ [8]. Currently the natural quantum number assignment $J^P = 1^+$ is favoured [9], but a charged particle that decays to a $c\bar{c}$ state cannot be explained within the constituent quark model.

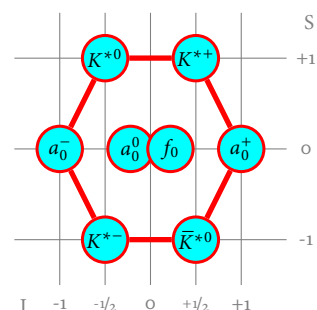


Figure 1.4: Hypothetical scalar meson nonet. K^* denotes the $K^*(800)$.

2

CHARM PHYSICS

The field of Charm physics was born in 1974 with the discovery of the J/ψ [10, 11]. The charm quark was predicted as the fourth quark from the non-existence of flavour changing neutral currents in conjunction with neutral kaon mixing. Another important discovery in charm physics were the D_{sJ} [12] states in 2003 which were not predicted by QCD. The most recent milestone was the observation of neutral D meson mixing. First evidence was found by *BABAR* [13] and *Belle* [14] in 2007, and in 2012 D^0 mixing was observed by *LHCb* [15].

The charm quark is an ‘up-type quark’ with a mass that is neither ‘light’ (u, d, s -quarks) nor ‘heavy’ (t, b -quarks). In theoretical models it cannot be treated properly in any mass limit, making it a difficult object to study. Particles that contain at least one charm quark are the objects of interest in charm physics. One class of these particles are the charmonium resonances (e. g. J/ψ or $\psi(2S)$) which we will not discuss further at this point. The second class are open charm mesons and baryons. Due to the scope of this thesis, we focus in the following on open charm mesons, in particular D^0 mesons.

D^0 mesons mostly decay via the charged weak current. They provide therefore a unique laboratory to study weak transitions of ‘up-type’ quarks. The main topics of this field are the precise measurement and prediction of the D^0 mixing parameters and the search for charge-parity (CP) violation.

Mixing between particle and anti-particle has been observed in several neutral meson systems: K^0 , B_d^0 , B_s^0 and D^0 . The fundamental mechanism is the same for these systems, yet they differ in the oscillation parameters. This mechanism will be outlined in the following. We rely on [16].

When we investigate short-lived particles we reconstruct them from their decay products. The reconstructed particle states are therefore eigenstates of the interaction that is responsible for their decay. In case of neutral D mesons this interaction is the weak interaction and we denote these eigenstates with a well defined quark content as $|D^0\rangle$ and $|\bar{D}^0\rangle$. Yet these particles can be produced in a different interaction. For instance in e^+e^- collisions at a center-of-mass energy of 3.773 GeV a $c\bar{c}$ pair is produced, which hadronizes into a pair of D mesons. The D^0 mesons are therefore produced via the strong interaction in so-called mass eigenstates denoted by $|D_1, D_2\rangle$. Since D^0 mesons are neutral, the quark content can change over time using so-called long and short distance processes, as shown in fig. 2.1. An initially produced pure state $|\bar{c}u\rangle$ can evolve to a pure $|c\bar{u}\rangle$ state or to a superposition of both. Therefore, if we investigate the decay of D^0 mesons the quark content that we measure changes, depending on the

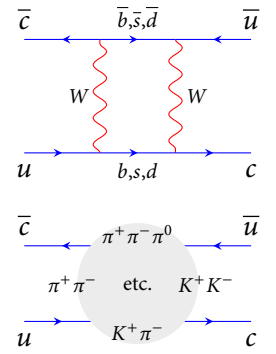


Figure 2.1: Diagrams for short- and long-distance contributions to D^0 - \bar{D}^0 oscillation.

decay time of the particle. Written in formula, $|D_{1,2}\rangle$ are linear combinations of $|D^0, \bar{D}^0\rangle$:

$$|D_{1,2}\rangle = p|D^0\rangle \pm q|\bar{D}^0\rangle. \quad (2.1)$$

The complex coefficients p, q satisfy unitarity: $|p|^2 + |q|^2 = 1$. Mixing occurs if there is a mass or width difference of the mass eigenstates $D_{1,2}$. In this case the mixing parameters

$$x = (m_2 - m_1)/\Gamma \quad y = (\Gamma_2 - \Gamma_1)/(2\Gamma) \quad (2.2)$$

are different from zero. In this definition $m_{1,2}$ and $\Gamma_{1,2}$ denote mass and width of $|D_{1,2}\rangle$. Γ is the D^0 width. The probability that an initially pure $|D^0\rangle$ state evolves after a certain time t into a pure final $|\bar{D}^0\rangle$ or $|D^0\rangle$ state is given by:

$$\begin{aligned} P(D^0 \rightarrow \bar{D}^0)(t) &= \frac{1}{2} \left| \frac{q}{p} \right|^2 e^{-\Gamma t} (\cosh(y\Gamma t) - \cos(x\Gamma t)) \\ P(D^0 \rightarrow D^0)(t) &= \frac{1}{2} e^{-\Gamma t} (\cosh(y\Gamma t) + \cos(x\Gamma t)). \end{aligned} \quad (2.3)$$

To explain the influence of charge-parity symmetry violation (*CPV*), we introduce another quantity:

$$\lambda_j = \frac{pA_j}{q\bar{A}_j} \propto \left| \frac{p}{q} \right| \left| \frac{A_j}{\bar{A}_j} \right| e^{-i\phi_{CP}}, \quad (2.4)$$

where A_j and \bar{A}_j are the decay amplitude of D^0 to a final state j and \bar{D}^0 to the *CP* conjugate state \bar{j} . If these amplitudes differ one speaks of direct *CPV*. In case of different mixing parameters for D^0 and \bar{D}^0 , *CPV* occurs in the mixing process and additionally *CPV* can happen in the interference of mixing and decay ($\phi_{CP} \neq 0$).

Describing the mixing of D^0 and \bar{D}^0 and the amount of *CP* violation within theoretical models is difficult since, as mentioned above, the *c* quark can neither be treated as a 'light' nor as a 'heavy' quark. A precise measurement of the D^0 branching fractions can help to improve theoretical predictions and constrain corresponding models.

3

MOTIVATION FOR THE ANALYSIS OF $D^0 \rightarrow K_S^0 K^+ K^-$

The topic of this thesis is the investigation of the decay $D^0 \rightarrow K_S^0 K^+ K^-$. The objective of this work is between meson spectroscopy and charm physics. We aim to contribute to the knowledge of light mesons by the investigation of the $K_S^0 K^+ K^-$ Dalitz plot. The mass range of the meson spectrum that can be investigated is roughly between 1 GeV and 1.5 GeV. The second part is the measurement of the absolute branching fraction which can help to refine theoretical predictions in the charm sector. Both measurements, the Dalitz plot analysis and the branching fraction measurement, will improve future Monte-Carlo simulations.

The decay of the D^0 meson to the final state $K_S^0 K^+ K^-$ is mediated via the weak interaction, as shown fig. 3.1. The decay is suppressed by a small phase-space. The mass difference between the three kaons and the D^0 meson is about 380 MeV and the branching fraction is $\mathcal{O}(10^{-3})$.

We analyze the decay using a data sample of 2.932 fb^{-1} of $e^+ e^-$ collisions which were collected by the BESIII detector at a center-of-mass energy of $\sqrt{s} = 3.773 \text{ GeV}$. A detailed description of the detector can be found in chapter 9 and an overview of all data samples that were collected with the BESIII detector is given in section 10.4. In $e^+ e^-$ collisions with $\sqrt{s} = 3.773 \text{ GeV}$, the $\psi(3770)$ resonance is produced besides a small QCD background. Since its mass is close to the threshold of a D meson pair it decays predominantly to it. This leads to a special kind of event topology which is illustrated in fig. 3.2. Each event consists of two D mesons in a quantum entangled state and therefore the sample provides a very clean laboratory to study charm decays. For neutral D mesons the quantum entanglement is important since the measurement of the flavour¹ or the CP quantum number of one D meson can be used to conclude the respective properties of the D meson. This technique is denoted by D tagging. More details are given in section 10.3.3. Exploiting the quantum entanglement is mandatory for some analyses, e. g. the measurement of the relative strong phase between $D^0 \rightarrow K_S^0 K^+ K^-$ and $\bar{D}^0 \rightarrow K_S^0 K^+ K^-$ as it was performed by CLEO-c [17].

We use D tagging to measure the flavour of the signal decay for the Dalitz plot analysis. The branching fraction measurement does not rely on the knowledge of the particle flavour and therefore we do not reconstruct the full event in this case.

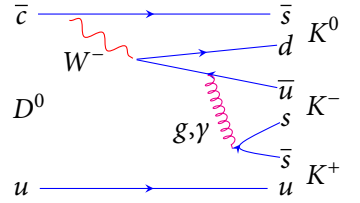
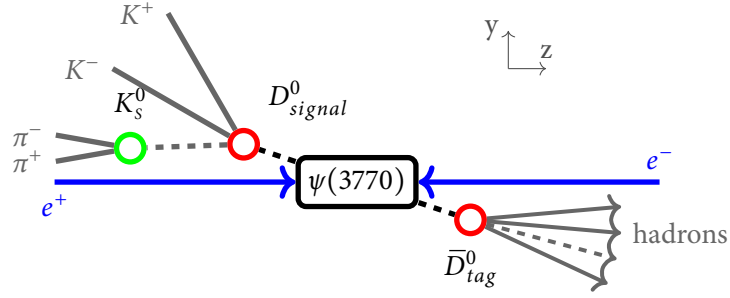
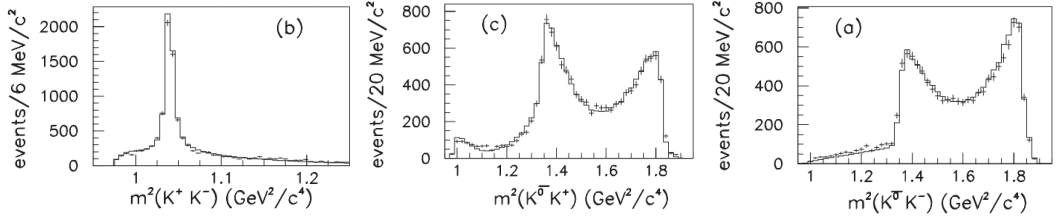


Figure 3.1: Feynman diagram of leading order for the decay $D^0 \rightarrow K_S^0 K^+ K^-$.

¹ The flavour of a meson refers to its quark content. In this context it indicates if a neutral D meson contains a charm (D^0) or an anti-charm (\bar{D}^0) quark.

Figure 3.2: $\psi(3770)$ decay topology in the $\psi(3770)$ rest frame.Figure 3.3: Dalitz plot projections of the *BABAR* data sample and the amplitude model [18].

3.1 PREVIOUS MEASUREMENT

Currently, the most precise measurement of the branching fraction of the $D^0 \rightarrow K_S^0 K^+ K^-$ decay is published by *BABAR* [18]:

$$\begin{aligned} \mathcal{B}_{\text{rel}} &= \frac{\Gamma(D^0 \rightarrow K_S^0 K^+ K^-)}{\Gamma(D^0 \rightarrow K_S^0 \pi^+ \pi^-)} \\ &= (15.8 \pm 0.2(\text{stat.}) \pm 0.5(\text{sys.})) \times 10^{-2}. \end{aligned} \quad (3.1)$$

The measurement is performed relative to the final state $D^0 \rightarrow K_S^0 \pi^+ \pi^-$. The PDG value [7] is derived from that measurement:

$$\mathcal{B}(D^0 \rightarrow K_S^0 K^+ K^-) = (4.47 \pm 0.34) \times 10^{-3} \quad (3.2)$$

The relative error is 7.6% which includes the uncertainty on the branching fraction of $D^0 \rightarrow K_S^0 \pi^+ \pi^-$. To date there is no absolute measurement of the branching fraction. The particle data group also lists results for the branching fraction which were published more than 20 years ago. Since these results are not used for the PDG average we also omit them here.

The above-mentioned *BABAR* analysis uses 12500 flavour tagged signal decays with a purity of 97.3%. Besides the branching fraction measurement, a partial wave analysis was performed and the $D^0 \rightarrow K_S^0 K^+ K^-$ Dalitz plot was analyzed using an isobar model. It was found that the Dalitz plot is well described by the coherent sum of four intermediate states: $a_0(980)^0$, $\phi(1020)$, $a_0(980)^+$ and $f_0(1370)$. The Dalitz plot projections of the data sample and the amplitude model are shown in fig. 3.3. The results in terms of fit parameters and fit fractions

Table 3.1: Fit parameters and fit fractions for the *BABAR* amplitude model [18].

Final state	Amplitude	Phase (rad)	Fit fraction (%)
$\bar{K}^0 a_0(980)^0$	1.0(Fix)	0.0(Fix)	66.4±1.6±7.0
$\bar{K}^0 \phi(1020)$	0.437±0.006±0.060	1.91±0.02±0.10	45.9±0.7±0.7
$K^- a_0(980)^+$	0.460±0.017±0.056	3.59±0.05±0.20	13.4±1.1±3.7
$\bar{K}^0 f_0(1400)$	0.35±0.033±0.162	-2.63±0.10±0.71	3.8±0.7±2.3
$\bar{K}^0 f_0(980)$			0.4±0.2±0.8
$K^+ a_0(980)^-$			0.8±0.3±0.8
Total			130.7±2.2±8.4

are listed in table 3.1. The channel was reanalysed with the full *BABAR* data sample [19] but since systematic uncertainties were not studied we will compare our result with the preceding measurement.

Part II

THEORY

In this part we discuss the theoretical background on the decay kinematics and decay dynamics. We introduce the basic ideas to describe and represent particle interactions. We construct two-particle angular momentum eigenstates using the helicity formalism and show the expansion of the transition amplitude in angular momentum partial waves. Later on we focus on the dynamics in particle interactions. We discuss what is considered to be a resonance and we motivate the Breit-Wigner and Flatté formulae for the description of a resonance. Furthermore we study the effect of the quantum entanglement on the decay of a D^0 meson. Finally we apply the concepts introduced before to the decay $D^0 \rightarrow K_s^0 K^+ K^-$.

4

PARTICLE INTERACTIONS

In this chapter we introduce the fundamentals to describe particle interactions.

We introduce the Mandelstam variables and the Mandelstam plane in section 4.2. A special representation of the Mandelstam variables of three-body decays is the so-called Dalitz plot as explained in section 4.3. We introduce the transition amplitude in section 4.4 and explain in section 4.5 how the transition amplitude can be constructed using the helicity formalism. The series expansion of the amplitude is finally given in section 4.6.

4.1 THE ISOBAR MODEL

The isobar model denotes the very common assumption that particles interact via two-body vertices. Applied to particle decays this means that a heavy particle decays via subsequent two-body decays to a set of final state particles. This is illustrated in fig. 4.1. The isobar model is widely used in partial wave analysis and works extremely well for many reactions. Yet it has some limitations. For instance it cannot describe final state interactions, which are illustrated in fig. 4.2.

4.2 MANDELSTAM VARIABLES

A particle interaction is usually described by a set of Lorentz invariant variables. In the isobar model we have to deal with vertices of two incoming particles, denoted by A and B, and two outgoing particles, denoted by C and D. The most common set of variables are the Mandelstam variables [20]:

$$s = (\mathbf{p}_A + \mathbf{p}_B)^2 \quad t = (\mathbf{p}_A + \mathbf{p}_C)^2 \quad u = (\mathbf{p}_A + \mathbf{p}_D)^2, \quad (4.1)$$

where \mathbf{p}_i is the four-momentum of the corresponding particle i . Four-momentum conservation imposes the requirement that

$$s + t + u = m_A^2 + m_B^2 + m_C^2 + m_D^2, \quad (4.2)$$

where the particle masses are denoted by m_i . Figure 4.3 shows the Mandelstam plane. The arrows on the axes indicate the positive and therefore physical region for each Mandelstam variable. Depending on the reaction, different

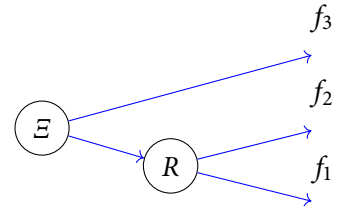


Figure 4.1: The isobar model.

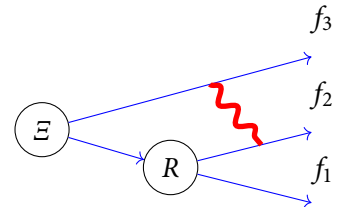


Figure 4.2: Final state interaction in a particle decay.

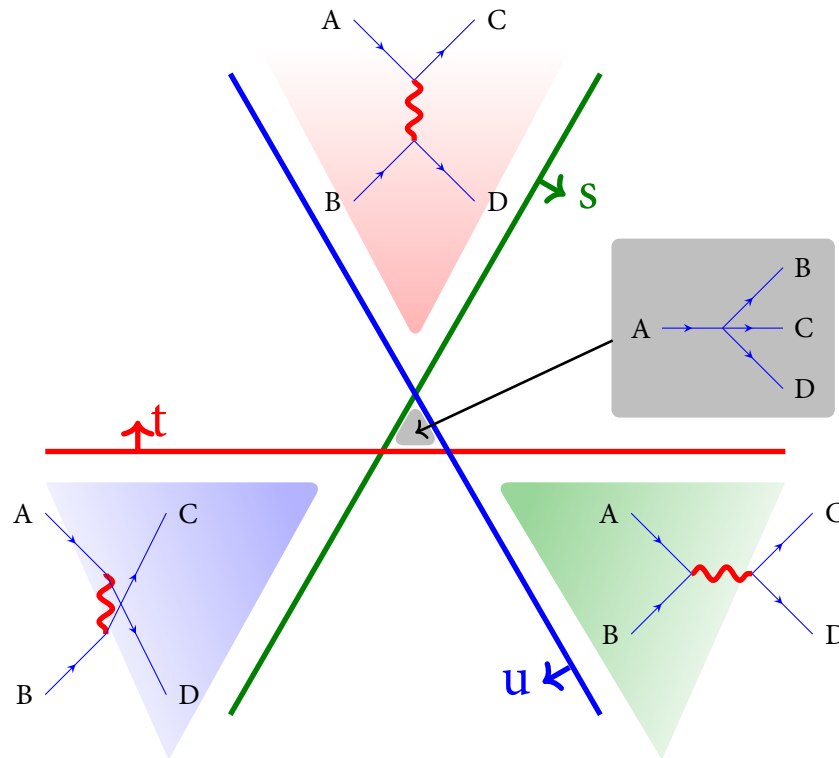


Figure 4.3: The Mandelstam plane spanned by the Mandelstam variables s , t and u which are defined in eq. (4.1). The central region is the physically allowed phase-space for particle decays. The other shaded regions indicate phase-space regions for particle scattering. Their exact size and shape depend on the particle masses.

regions on the plane are physically allowed. In case of a particle decay, the Mandelstam variables are positive and the phase-space region is located in the center triangle. This is the so-called Dalitz plot which we discuss in detail later on in section 4.3. For scattering processes only one variable of (s, t, u) can be positive. The calculation of the exact phase-space boundary for each channel is outlined in [21, Chapter 3.2].

The fundamental assumption, the so-called Mandelstam hypothesis [20–22], is that the amplitudes for all processes including the decay in the center of the Mandelstam plane, are represented by the same analytic function. And if we determine the amplitude in one channel we can conclude properties of the amplitude in another channel. This is called crossing and is described in detail in [21, Chapter 7.2].

4.2.1 Kinematics of two-particle vertices

In the following we introduce some quantities that are necessary to describe the kinematics of two-particle vertices. The **break-up momentum** q_{AB} denotes

the momentum of two particles A and B with masses m_A and m_B in their rest frame for a given center-of-mass energy \sqrt{s} . It is given by [7, eq. 46.20a]:

$$q_{AB}^2(s) = \frac{(s - (m_A + m_B)^2)(s - (m_A - m_B)^2)}{4s}. \quad (4.3)$$

The energy of particle B in the common rest-frame of A and B is given by:

$$E_{cms,B} = \frac{s - m_A^2 + m_B^2}{2\sqrt{s}}. \quad (4.4)$$

Using the break-up momentum we can calculate the **phase-space factor**:

$$\hat{\rho}_{AB}(s) = \frac{1}{16\pi} \frac{2\sqrt{|q_{AB}(s)|^2}}{\sqrt{s}}. \quad (4.5)$$

The phase-space factor denotes the particle momentum relative to the center-of-mass energy. It is zero at threshold $s_{th} = (m_A + m_B)^2$ and rises with higher center-of-mass energies. The function behavior at and below threshold can lead to problems with resonances outside the phase-space regions. This issue is addressed in chapter 7.

4.2.2 Scattering and helicity angle

Using the Mandelstam variables and the break-up momenta from eq. (4.3) q_{AB} and q_{CD} , the scattering angle is illustrated in fig. 4.4 and is given by [21, Equation 4.83]:

$$\cos \theta_{CB} = \frac{s(t - u) + (m_A^2 - m_B^2)(m_C^2 - m_D^2)}{4sq_{AB}q_{CD}}. \quad (4.6)$$

In a decay the corresponding angle is called helicity angle. We consider a decay of a particle Ξ to three final state particles f_1, f_2 and f_3 . The decay is illustrated in fig. 4.5. The helicity angle can be calculate via a sequence of Lorentz transformations from the final state four-momenta:

1. Lorentz transformation of the momenta of f_1 and f_2 to the common rest frame. The direction of the decay axis is denoted with (θ_R, ϕ_R) .
2. Lorentz transformation of the combined momentum of f_1 and f_2 and the momentum of f_3 to their rest frame. The direction of the decay axis is denoted with (θ_Ξ, ϕ_Ξ) .
3. Calculate the angle between the directions (θ_R, ϕ_R) and (θ_Ξ, ϕ_Ξ) .

The helicity angle has also a closed-form [23]:

$$\cos \theta_{12} = -\frac{m_{23}^2 - m_2^2 - m_3^2 - 2E_{12}^* E_3^*}{2q_{12}^* q_3^*}, \quad (4.7)$$

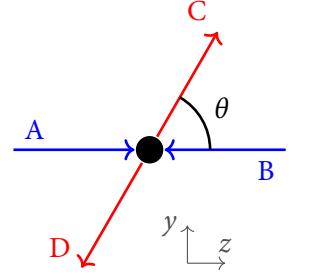


Figure 4.4: Scattering angle θ in a two-body reaction.

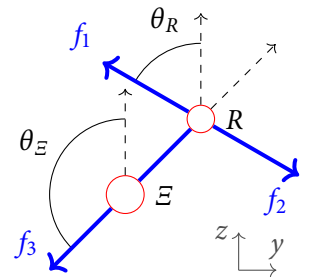


Figure 4.5: Sequential two-body decay. The angles are measured in the rest frame of the respective decay.

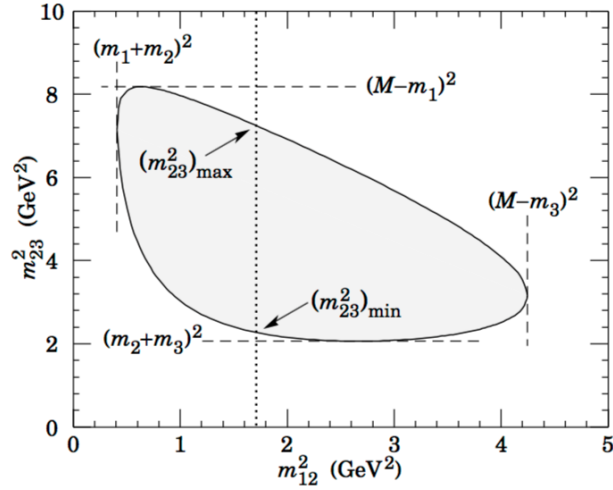


Figure 4.6: Phase-space boundary for the decay of a particle with mass M to three particles with masses m_1, m_2 and m_3 [7].

where m_{ij}^2 is the invariant mass of particle i and j . Quantities marked with (*) are measured in the rest frame of the particles f_1 and f_2 , see eqs. (4.3) and (4.4). For decays with more than three final state particles the Lorentz boosts have to be adapted, but the procedure is equivalent.

4.3 THE DALITZ PLOT

We focus on three-body decays of particles: $\Xi \rightarrow f_1 f_2 f_3$. For simplicity we assume that the decaying particle Ξ as well as the final state particles f_i are spinless. We already have seen that for a particle decay the Mandelstam variables s, t, u are always positive. Since s, t, u fulfill eq. (4.2) these variables over constrain the problem - we need only two variables to describe the process. An analysis of the intermediate decay substructure using a representation of two variables was first performed by R.H. Dalitz in 1954 [24] in the analysis of kaon decays (formerly known as τ and Θ mesons) to three pions. He used the particle energies to represent the decay in a two-dimensional plane. This representation is not invariant under Lorentz transformation and therefore nowadays the representation by two (Lorentz invariant) Mandelstam variables is usually used. This is known as Dalitz plot. It is also possible to use one Mandelstam variable and the corresponding helicity angle to represent the decay. Since angular momentum is conserved, this representation can be of advantage.

The phase-space boundary of the decay of a particle with mass M to three final state particles with mass m_1, m_2 and m_3 is shown in fig. 4.6. The differential decay rate within the phase-space boundary is given by [7]:

$$\frac{d\Gamma}{dm_{13}^2 dm_{23}^2} = \frac{1}{8\pi^3} \frac{1}{32M^3} |\mathcal{M}|^2. \quad (4.8)$$

The Dalitz plot is a very simple and intuitive way to display the dynamics of the matrix element \mathcal{M} . For illustration purposes we show in fig. 4.7 an artificial

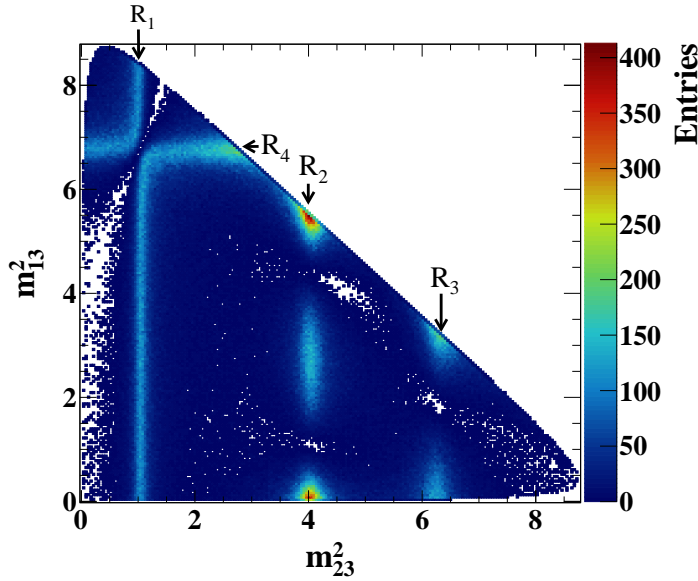


Figure 4.7: Artificial Dalitz amplitude model with four resonances.

model containing four resonances. The parameters are chosen to show many physical properties that can be derived from a Dalitz plot. From the phase-space boundary we can derive that final state particle 3 has to be mass-less since the phase-space boundary approaches zero in both variables. The resonance R_1 occurs in the invariant mass of particle 2 and 3 and is spin-less as indicated by the uniform population along the band. The resonance R_2 and R_3 appear in the same subsystem but have higher spins. The spin can be derived from the number of dips. In this case R_2 has spin 2 and R_3 has spin 1. The 4th resonance is spin-less and shows up in the subsystem of particle 1 and 3. It interferes with R_1 destructively, since at the intersection of both bands the intensity vanishes.

As outlined before many properties of a decay can be observed without further analysis. Yet a full amplitude analysis of the Dalitz plot is necessary for several reasons. Sometimes resonances only contribute a small fraction to the intensity, and are therefore not visible by eye. Nevertheless they can have strong influence due to interference with other resonances. The result of an amplitude analysis is the amount of intensity that is contributed by a single resonance or a set of resonances (so-called fit fractions) and the resonance parameters, e. g. mass and width. Such quantitative results can be compared among different reactions and/or different experiments.

The Dalitz plot analysis for the decay $D^0 \rightarrow K_s^0 K^+ K^-$ is presented in chapter 12. In the next chapter we discuss the dynamics of particle scattering and particle decay.

4.4 TRANSITION AMPLITUDE

In the following we outline the basis for a mathematical description of particle scattering from a free initial $|i\rangle$ state to a free final state $|f\rangle$. Since we require

initial and final state particles which do not interact with each other, this description is only strictly valid for the strong interactions. In general the description is valid for an arbitrary number of particles, yet for simplicity we will restrict ourself to the interaction of two initial-state particles to two final state particles. The mathematical object that encodes the propagation is the scattering operator S which is defined by its matrix elements:

$$S_{fi} = \langle f | S | i \rangle. \quad (4.9)$$

S_{fi} contains elements for all possible initial and final states. It also includes the case that particles do not interact at all. We separate that case from the scattering matrix and obtain the transition matrix T :

$$\langle f | S | i \rangle = \langle f | i \rangle + i \langle f | T | i \rangle. \quad (4.10)$$

If a quantity is conserved in the interaction its operator commutes with the scattering operator:

$$[X, S] = 0. \quad (4.11)$$

The state vector $|i\rangle$ contains all relevant information and we write it as $|\mathcal{P}_i, \alpha_i\rangle$, \mathcal{P}_i contains all four-momenta and α_i all other information such as particle spins. Since four-momentum is conserved we can separate it:

$$\langle f | S | i \rangle = \langle f | i \rangle + i \langle \mathcal{P}_f | \mathcal{P}_i \rangle \langle \alpha_f | T_{\mathcal{P}} | \alpha_i \rangle. \quad (4.12)$$

The transition operator can still depend on the momentum and we denote it with $T_{\mathcal{P}}$. In case of scattering of two spin-less particles the transition amplitude is a scalar function of two Lorentz-invariant quantities. For instance the Mandelstam variables s and t :

$$\langle \alpha_f | T_{\mathcal{P}} | \alpha_i \rangle = T(s, t). \quad (4.13)$$

If particles with spin are involved we can use the conservation of angular momentum to simplify the problem. In section 4.5 we show how to construct two-particle states which are eigenstates of the angular momentum operator. The particles states are described by the angular momentum J , its projection M onto a quantization axis, and the helicities λ_i and λ_f . The helicity of a particle is defined in eq. (4.19). The transition matrix element is connected to the helicity amplitudes $T_{\lambda_i \lambda_f}(s, t)$ via:

$$\begin{aligned} \langle \alpha_f | T_{\mathcal{P}} | \alpha_i \rangle &= \langle J_f M_f, \lambda_f | T_{\mathcal{P}} | J_i M_i, \lambda_i \rangle \\ &= \delta_{J_f J_i} \delta_{M_f M_i} T_{\lambda_i \lambda_f}(s, t). \end{aligned} \quad (4.14)$$

The helicity amplitudes will be derived in section 4.5.

4.4.1 Probability conservation and causality

We already mentioned conserved quantities like four-momentum and angular momentum. In this part we want to introduce two other physical postulates: the **conservation of probability** and **causality**. Conservation of probability implies that a system in initial state $|i\rangle$ evolves to a state $|n\rangle$ with probability P_n and $|n\rangle$ is part of a complete set:

$$\begin{aligned} 1 = \sum_n P_n &= \sum_n |\langle n|S|i\rangle|^2 \\ &= \sum_n \langle i|S^\dagger|n\rangle \langle n|S|i\rangle = \langle i|S^\dagger S|i\rangle. \end{aligned} \quad (4.15)$$

From this expression one can obtain the unitarity relation [21, Chapter 5] for the scattering operator S and its implication on the transition operator T :

$$S^\dagger S = SS^\dagger = \mathbb{1} \quad (4.16)$$

$$T - T^\dagger = iT^\dagger T. \quad (4.17)$$

The conservation of probability leads to the optical theorem which connects the imaginary part of the scattering amplitude in forward direction with the total cross section of a process:

$$\text{Im } T(s, t = 0) = \frac{q\sqrt{s}}{8\pi^2} \sigma_{tot}. \quad (4.18)$$

The derivation is outlined in appendix A.2.

The second physical postulate that we want to mention here quickly is **causality**. We presume the cause precedes its effect. It can be proven that amplitudes respecting causality are complex analytic functions [21]. A function is called analytic if it is locally given by a convergent power series.

Probability conservation and causality are fundamental postulates in physics. In practise we have to develop models for decay and scattering amplitudes. This involves approximations which can lead to a violation of unitarity and/or analyticity. An example is the Flatté formula (section 5.3) which does not strictly preserve unitarity.

4.5 THE HELICITY FORMALISM

We need a formalism to construct angular distributions in particle reactions. The angular distribution is determined by the helicity of the particles that are involved and by the angular momentum between them. An overview of various so-called ‘spin formalisms’ is given in [25]. There are basically three classes:

- Formalisms based on Lorentz invariants
- (Covariant) Tensor formalisms
- Spin-projection formalisms

The first approach usually depends strongly on the decay under study and we list it for completeness only. Tensor formalisms can be formulated in a covariant manner and is therefore the preferred formalism for highly relativistic problems. Tensor formalisms are efficient and elegant but for reactions involving high angular momenta or many subsequent decays they are complicated.

On the contrary, spin-projection formalisms are not strictly covariant but sufficiently precise for many reactions. Common representatives are the canonical (orbital) and the helicity formalism. Among those, single particle states are defined by their four-momentum \mathbf{p} , their spin s and its projection to an arbitrary axis. The canonical formalism uses an arbitrary, but fixed projection axis (usually the z -axis of the laboratory coordinate system) and the helicity formalism uses the direction of the particle momentum. In that case the projection of the spin is the particle helicity which is defined as:

$$\lambda = \frac{\vec{s} \cdot \vec{p}}{|\vec{p}|}. \quad (4.19)$$

The choice of the projection axis determines the symmetries of the formalism. The parity operation on a helicity amplitude is more complicated than on a canonical amplitude, since the helicity is not invariant under parity operation. On the other hand the helicity is invariant under rotations and Lorentz boosts which simplifies the construction of a relativistic basis.

The helicity formalism was originally developed by Jacob & Wick [26]. In the following we derive it in detail by relying on [21, 27, 28]. We give a short introduction on rotation operators and the Wigner D-matrix, followed by the construction of single and two-particle states in the plane-wave and spherical basis. Finally we apply the result on two-body scattering and decay processes.

4.5.1 Introduction to rotation operators and Wigner D-matrix

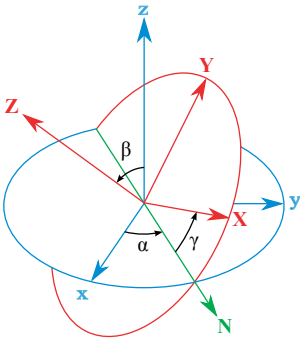


Figure 4.8: Euler rotation [29].

We consider a fixed coordinate system xyz and a rotated system XYZ . The rotation is then given by the Euler angles $(\alpha\beta\gamma)$. The rotation operator $R(\alpha\beta\gamma)$ can be seen as three successive rotations (illustrated in fig. 4.8):

1. Rotation around the z -axis by α
2. Rotation around the N -axis by β
3. Rotation around the Z -axis by γ

And therefore

$$\begin{aligned} R(\alpha\beta\gamma) &= R_Z(\gamma)R_N(\beta)R_z(\alpha) \\ &= e^{-i\gamma J_Z} e^{-i\beta J_N} e^{-i\alpha J_z}. \end{aligned} \quad (4.20)$$

In this definition the angles β and γ are not measured in the fixed coordinate system xyz . This is not desired for practical use and therefore we want to define the rotation with angles $(\alpha\beta\gamma)$ with respect to the original system xyz . Recall that an operator transforms under rotation as $J' = RJR^\dagger$. J_Z can be expressed by

the operator J_z followed by a rotation around the N -axis. The rotation around N can in turn be expressed by the rotation operator J_y followed by a rotation around z :

$$\begin{aligned}
 R(\alpha\beta\gamma) &= R_Z(\gamma)R_N(\beta)R_z(\alpha) \\
 &= (R_N(\beta)e^{-i\gamma J_z}R_N^\dagger(\beta))R_N(\beta)R_z(\alpha) \\
 &= (R_z(\alpha)e^{-i\beta J_y}R_z^\dagger(\alpha)e^{-i\gamma J_z}R_N^\dagger(\beta))R_N(\beta)R_z(\alpha) \\
 &= e^{-i\alpha J_z}e^{-i\beta J_y}e^{-i\gamma J_z}. \tag{4.21}
 \end{aligned}$$

Note that the order of the rotations has changed. We have rotated the operators J_Z and J_N to J_z and J_y and the angles $(\alpha\beta\gamma)$ are now measured with respect to the original system xyz . In this derivation we used the unitarity of the rotation operators

$$e^{-i\gamma R(\beta)}R^\dagger(\beta) = R(\beta)e^{-i\gamma J}R^\dagger(\beta) \tag{4.22}$$

and that a rotation around the z -axis does not change the operator J_z .

Equation (4.21) is where the Wigner D-matrix [30] originates from. The Wigner D-matrix is the matrix representation of the operator $R(\alpha\beta\gamma)$ with angles $(\alpha\beta\gamma)$ measured in the fixed coordinate system xyz [30, Chapter XV].

Let us consider the rotation of an angular momentum eigenstate $|jm\rangle$. The angular momentum operator commutes with the rotation operator ($[R, J^2] = 0$) and the rotation can be represented as:

$$R(\alpha\beta\gamma)|jm\rangle = \sum_{m'=-j}^j D_{m'm}^j(\alpha\beta\gamma)|jm'\rangle. \tag{4.23}$$

Written in a different way, we obtain the definition of the Wigner D-matrix:

$$\begin{aligned}
 D_{m''m}^j(\alpha\beta\gamma) &= \sum_{m'=-j}^j D_{m'm}^j(\alpha\beta\gamma) \langle jm'' | \cancel{jm'} \rangle \delta_{m''m} \\
 &= \langle jm'' | R(\alpha\beta\gamma) | jm \rangle \\
 &= \langle jm'' | e^{-i\alpha J_z} e^{-i\beta J_y} e^{-i\gamma J_z} | jm \rangle \\
 &= \langle jm'' | e^{-i\alpha J_z} | jm'' \rangle \langle jm'' | e^{-i\beta J_y} | jm \rangle \langle jm | e^{-i\gamma J_z} | jm \rangle \\
 &= e^{-i\alpha m''} d_{m''m}^j(\beta) e^{-i\gamma m}. \tag{4.24}
 \end{aligned}$$

The (small) Wigner D-matrix is denoted by $d_{m''m}^j(\beta)$. Its definition and some properties are given in appendix A.1.

In the following we construct plane wave two-particle states $|p, \theta\phi\rangle$. A better basis for practical use are spherical wave helicity states $|p, JM\rangle$ since they depend on conserved quantities. The Wigner-D functions are used to transform from the plane wave basis to the spherical helicity basis.

4.5.2 *Plane-wave helicity states*

We start from a single particle in its rest frame¹ with spin s and the spin-projection λ to an arbitrary axis. The spin-projection in the rest frame is identical to the particle helicity. A state with arbitrary momentum can be obtained from the state at rest by a Lorentz boost $L(\vec{p})$ with a 3-momentum \vec{p} which we can express in spherical coordinates as (p, θ, ϕ) . This transformation can be composed from a boost along the (arbitrary) z -axis and a rotation around $(\theta\phi)$:

$$|\vec{p}, s\lambda\rangle = L(\vec{p})|0, s\lambda\rangle \quad (4.25)$$

$$= R(\phi, \theta, -\phi)L_z(p)|0, s\lambda\rangle. \quad (4.26)$$

A Lorentz invariant normalization of the single particle states $|\vec{p}, s\lambda\rangle$ is chosen:

$$\langle \vec{p}', s'\lambda' | \vec{p}, s\lambda \rangle = (2\pi)^3 2E \delta^3(\vec{p}' - \vec{p}) \delta_{s's} \delta_{\lambda'\lambda}. \quad (4.27)$$

The two particle plane-wave states are given by the direct product of two single particle states:

$$|\vec{p}_1 \vec{p}_2, s_1 s_2 \lambda_1 \lambda_2\rangle = |\vec{p}_1, s_1 \lambda_1\rangle \otimes |\vec{p}_2, s_2 \lambda_2\rangle. \quad (4.28)$$

The particle spins are fixed and we suppress them. We choose the center-of-mass frame which simplifies the problem, since the particle momenta are $\vec{p}_1 = -\vec{p}_2 = \vec{p} = (p, \theta, \phi)$. Furthermore the magnitude of the momentum is completely determined by the masses of particle 1 and 2 and the center-of-mass energy. Therefore, it can be factored out. The two-particle state with proper normalization is given by [27, Equation 3.13]:

$$|\vec{p}_1 \vec{p}_2, s_1 s_2 \lambda_1 \lambda_2\rangle_{cm} = |p\theta\phi\lambda_1\lambda_2\rangle \quad (4.29)$$

$$= (2\pi)^3 \left[\frac{4\sqrt{s}}{p} \right]^{1/2} |\theta\phi, \lambda_1\lambda_2\rangle |p\rangle. \quad (4.30)$$

4.5.3 *Spherical-wave helicity states*

The plane-wave helicity states $|p\theta\phi\lambda_1\lambda_2\rangle$ are eigenstates of θ and ϕ . These are in general not conserved in particle interactions. A better basis would be an eigenstate basis of conserved quantities only. Therefore, it is convenient to apply a basis transformation from plane-wave helicity states to angular momentum eigenstates which we call spherical helicity states in the following.

We expand the plane-wave helicity states in an angular momentum eigenbasis:

$$|p, \theta\phi, \lambda_1\lambda_2\rangle = \sum_{JM} c_{JM}(p, \theta\phi, \lambda_1\lambda_2) |p, JM, \lambda_1\lambda_2\rangle. \quad (4.31)$$

¹ For photons another approach is necessary, see [27, B.6]

We determine the coefficients $c_{JM}(p, \theta\phi, \lambda_1\lambda_2)$ starting from the special case $\theta = \phi = 0$. In that scenario the direction of the particle momenta is along z -axis and the eigenvalue of the spin-projection operator J_z is $\lambda = \lambda_1 - \lambda_2$, as illustrated in fig. 4.9. This writes as:

$$|p, 00, \lambda_1\lambda_2\rangle = \sum_{JM} c_{JM}(p, 00, \lambda_1\lambda_2) |p, JM, \lambda_1\lambda_2\rangle \quad (4.32)$$

$$= \sum_J c_{J\lambda}(p, 00, \lambda_1\lambda_2) |p, J\lambda, \lambda_1\lambda_2\rangle. \quad (4.33)$$

Then we rotate the decay axis to arbitrary values of θ and ϕ :

$$\begin{aligned} & |p, \theta\phi, \lambda_1\lambda_2\rangle \\ &= R(\phi, \theta, -\phi) |p, 00, \lambda_1\lambda_2\rangle \\ &= R(\phi, \theta, -\phi) \sum_J c_{J\lambda}(p, 00, \lambda_1\lambda_2) |p, J\lambda, \lambda_1\lambda_2\rangle \\ &= \sum_{JM} c_{J\lambda}(p, 00, \lambda_1\lambda_2) D_{M\lambda}^J(\phi, \theta, -\phi) |p, JM, \lambda_1\lambda_2\rangle. \end{aligned} \quad (4.34)$$

We adopt the definition from [26] $(\alpha, \beta, \gamma) = (\phi, \theta, -\phi)$ and we use eq. (4.23) to obtain:

$$c_{JM}(p, \theta\phi, \lambda_1\lambda_2) = \sqrt{\frac{2J+1}{4\pi}} c_{J\lambda}(p, 00, \lambda_1\lambda_2) D_{M\lambda}^J(\phi, \theta, -\phi). \quad (4.35)$$

The coefficients are normalized to $|c_{JM}| = 1$. Then the transformation from plane-wave helicity states to spherical helicity states is given by:

$$|p, \theta\phi, \lambda_1\lambda_2\rangle = \sum_{JM} \sqrt{\frac{2J+1}{4\pi}} D_{M\lambda}^J(\phi, \theta, -\phi) |p, JM, \lambda_1\lambda_2\rangle. \quad (4.36)$$

4.5.4 Parity

The strong and electromagnetic interaction are parity conserving. This can be exploited to reduce the number of independent amplitude contributions for a reaction. We shortly outline how single-particle states and two-particles states transform under parity operation.

The parity operator \mathcal{P} applies a sign flip in all spatial coordinates (a point reflection). A single particle at rest is an eigenstate of the parity operator:

$$\mathcal{P} |p = 0, s\lambda\rangle = \eta |p = 0, s\lambda\rangle. \quad (4.37)$$

Its intrinsic parity is denoted by η . A particle with a momentum along the z -axis transforms under parity operation as:

$$\mathcal{P} |p_z, s\lambda\rangle = \eta (-1)^{s-\lambda} e^{i\pi J_y} |p_z, s, -\lambda\rangle \quad (4.38)$$

$$\mathcal{P} |-p_z, s\lambda\rangle = \eta (-1)^{s+\lambda} e^{i\pi J_y} |-p_z, s, -\lambda\rangle. \quad (4.39)$$

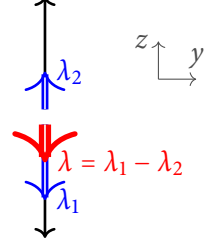


Figure 4.9: Spin-projection in the center of mass system of two particles with helicities λ_1 and λ_2 . The momentum direction (black) is chosen along the z -axis.

The derivation of these relations can be found in [27, Chapter 6.1]. We use them to study the behavior of two-particle states under parity operation. **Two-particle plane-wave helicity states** in forward direction ($\theta = \phi = 0$) transform as:

$$\begin{aligned}
& \mathcal{P} |p, 00, \lambda_1 \lambda_2\rangle \\
&= \mathcal{P} |p_z, s_1 \lambda_1\rangle \mathcal{P} |-p_z, s_2 \lambda_2\rangle \\
&= \eta_1 (-1)^{s_1 - \lambda_1} e^{i\pi J_y} |p_z, s_1, -\lambda_1\rangle \eta_2 (-1)^{s_2 + \lambda_2} e^{i\pi J_y} |p_z, s_2, -\lambda_2\rangle \\
&= \eta_1 \eta_2 (-1)^{s_1 - \lambda_1 + s_2 + \lambda_2} e^{i\pi J_y} (|p_z, s_1, -\lambda_1\rangle |p_z, s_2, -\lambda_2\rangle) \\
&= \mathcal{N} e^{i\pi J_y} |p, 00, -\lambda_1, -\lambda_2\rangle. \tag{4.40}
\end{aligned}$$

For brevity we merge the pre-factors:

$$\mathcal{N} = \eta_1 \eta_2 (-1)^{s_1 - \lambda_1 + s_2 + \lambda_2}. \tag{4.41}$$

The transformation from plane-wave helicity states to **spherical helicity states** is obtained by inserting eq. (4.36) on both sides of eq. (4.40).

$$\begin{aligned}
& \mathcal{P} \sum_{JM} c_J D_{M\lambda}^J(0, 0, 0) |p, JM, \lambda_1 \lambda_2\rangle \\
&= \mathcal{N} e^{i\pi J_y} \sum_{JM} c_J D_{M, -\lambda}^J(0, 0, 0) |p, JM, -\lambda_1, -\lambda_2\rangle \\
& \mathcal{P} \sum_J c_J |p, J\lambda, \lambda_1 \lambda_2\rangle \\
&= \mathcal{N} e^{i\pi J_y} \sum_J c_J |p, J(-\lambda), -\lambda_1, -\lambda_2\rangle \\
&= \mathcal{N} \sum_J c_J \sum_{M'} D_{M', -\lambda}^J(0, -\pi, 0) |p, JM', -\lambda_1, -\lambda_2\rangle \\
&= \mathcal{N} \sum_J c_J (-1)^{J-\lambda} |p, J\lambda, -\lambda_1 - \lambda_2\rangle. \tag{4.42}
\end{aligned}$$

We have used relations from A.1. The last equation holds term by term in J and therefore we get the transformation of spherical helicity states under parity:

$$\mathcal{P} |p, J\lambda, \lambda_1 \lambda_2\rangle = \eta_1 \eta_2 (-1)^{s_1 - \lambda_1 + s_2 + \lambda_2} (-1)^{J-\lambda} |p, J\lambda, -\lambda_1, -\lambda_2\rangle. \tag{4.43}$$

This equation was derived for $\lambda = \lambda_1 - \lambda_2$ but we can now use the raising and lowering operators $J_{\pm} = J_x \pm iJ_y$ to step to values of M between $-J$ and J and therefore:

$$\mathcal{P} |p, JM, \lambda_1 \lambda_2\rangle = \eta_1 \eta_2 (-1)^{s_1 - \lambda_1 + s_2 + \lambda_2} (-1)^{J-\lambda} |p, JM, -\lambda_1, -\lambda_2\rangle. \tag{4.44}$$

4.6 PARTIAL WAVE EXPANSION

We expressed two-body particles states in a basis of angular momentum eigenstates. We use this result to expand the transition matrix element $T_{fi} = \langle f | T | i \rangle$ in angular momentum eigenstates. The summands of the series are called partial waves. The idea behind this is that we want to investigate the spectrum of QCD

bound states which have defined quantum numbers. The goal is to find new states and to determine their quantum numbers. Therefore, an expansion of the total amplitude in partial waves with defined quantum numbers is convenient since a new bound state would only contribute to a single partial wave and it is therefore easier to isolate.

In the following we show this expansion for the case of a two-body scattering process and for the case of a particle decay.

4.6.1 Two-body scattering

The scattering process $i_1 i_2 \rightarrow f_1 f_2$ is illustrated in fig. 4.10. Without loss of generality we assume that the collision axis of i_1 and i_2 is along the z -axis. The transition amplitude from an initial state $|i\rangle$ to a final state $|f\rangle$ can be written using eq. (4.30) as:

$$\langle f|T|i\rangle = 4(2\pi)^6 \sqrt{\frac{s}{p_f p_i}} \langle p_f | \langle \theta_f \phi_f, \lambda_{f_1} \lambda_{f_2} | T | 00, \lambda_{i_1} \lambda_{i_2} \rangle | p_i \rangle. \quad (4.45)$$

The transition is independent of the initial and final momenta, but can depend on the center-of-mass energy s . Conventionally the delta function is factored out as shown in eq. (4.12), and we obtain:

$$\begin{aligned} \langle f|T|i\rangle &= (2\pi)^4 \delta^4(p_f - p_i) \\ &\times 4(2\pi)^2 \sqrt{\frac{s}{p_f p_i}} \langle \theta_f \phi_f, \lambda_{f_1} \lambda_{f_2} | T_{\mathcal{P}} | 00, \lambda_{i_1} \lambda_{i_2} \rangle. \end{aligned} \quad (4.46)$$

We use the Mandelstam variable s to express the dependence of the transition amplitude on the four-momenta:

$$\langle f|T_{\mathcal{P}}|i\rangle = 4(2\pi)^2 \sqrt{\frac{s}{p_f p_i}} \langle \theta_f \phi_f, \lambda_{f_1} \lambda_{f_2} | T(s) | 00, \lambda_{i_1} \lambda_{i_2} \rangle. \quad (4.47)$$

Now we change the basis from plane-wave helicity states $|\theta\phi, \lambda_1\lambda_2\rangle$ to spherical helicity states $|JM, \lambda_1\lambda_2\rangle$ by inserting two times the unity matrix:

$$\begin{aligned} \langle f|T_{\mathcal{P}}|i\rangle &= 4(2\pi)^2 \sqrt{\frac{s}{p_f p_i}} \sum_{JM'} \sum_{J'M'} \langle \theta_f \phi_f, \lambda_c \lambda_d | |JM, \lambda_c \lambda_d\rangle \\ &\times \langle JM, \lambda_c \lambda_d | T(s) | J'M', \lambda_a \lambda_b \rangle \langle J'M', \lambda_a \lambda_b | |00, \lambda_a \lambda_b\rangle. \end{aligned} \quad (4.48)$$

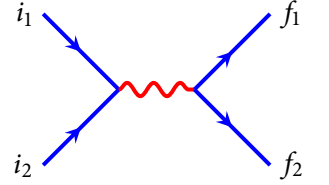


Figure 4.10: Two-body scattering in s -channel.

Using eq. (4.36) we obtain:

$$\begin{aligned}
\langle f | T_{\mathcal{P}} | i \rangle &= 4(2\pi)^2 \sqrt{\frac{s}{p_f p_i}} \sum_{JM} \sum_{J'M'} \delta_{JJ'} \delta_{MM'} \sqrt{\frac{2J+1}{4\pi}} \sqrt{\frac{2J'+1}{4\pi}} \\
&\quad \times D_{M\lambda_f}^{J*}(\phi_f, \theta_f, -\phi_f) \langle \lambda_c \lambda_d | T^J(s) | \lambda_a \lambda_b \rangle \overset{1}{D_{M\lambda_i}^{J'}(\theta, 0, 0)} \\
&= 4\pi \sqrt{\frac{s}{p_f p_i}} \sum_{JM} (2J+1) \\
&\quad \times D_{M\lambda_f}^{J*}(\phi_f, \theta_f, -\phi_f) \langle \lambda_c \lambda_d | T^J(s) | \lambda_a \lambda_b \rangle \\
&= 4\pi \sqrt{\frac{s}{p_f p_i}} \sum_J (2J+1) \\
&\quad \times D_{\lambda_i \lambda_f}^{J*}(\phi_f, \theta_f, -\phi_f) \langle \lambda_c \lambda_d | T^J(s, t) | \lambda_a \lambda_b \rangle. \tag{4.49}
\end{aligned}$$

The angular momentum is conserved and therefore the two-particle states do not depend on it, but the matrix $T^J(s, t)$ can depend on it. We have expanded the transition matrix element in partial waves using the helicity formalism. The dynamics of the decay is encoded in the helicity amplitudes $\langle \lambda_c \lambda_d | T^J(s, t) | \lambda_a \lambda_b \rangle$.

4.6.2 Two-body decay

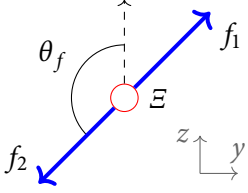


Figure 4.11: Two-body decay in its rest frame. The decay angle θ_f is measured versus the z -axis.

Now we want to do the same exercise for a two-body decay. We consider the decay of a particle Ξ in its rest frame with spin $J = s_{\Xi}$ and spin-projection $M = \lambda_{\Xi}$ as initial state $|i\rangle$. The final state $|f\rangle$ contains the particles f_1 and f_2 and can be written as $|\theta_f \phi_f, \lambda_{f_1} \lambda_{f_2}\rangle$. The decay is illustrated in fig. 4.11 and its amplitude can be expressed as:

$$\langle f | T_{\mathcal{P}} | \Xi \rangle = A_{\Xi} = \langle \theta_f \phi_f, \lambda_{f_1} \lambda_{f_2} | T | JM \rangle. \tag{4.50}$$

In analogy to eq. (4.49) we get:

$$\begin{aligned}
\langle f | T_{\mathcal{P}} | \Xi \rangle &= \sum_{J'M'} \langle \theta_f \phi_f, \lambda_{f_1} \lambda_{f_2} | J'M', \lambda_{f_1} \lambda_{f_2} \rangle \langle J'M', \lambda_{f_1} \lambda_{f_2} | T(s, t) | JM \rangle \\
&= \sum_{J'M'} \sqrt{\frac{2J'+1}{4\pi}} D_{M'\lambda}^{J'*}(\phi_f, \theta_f, -\phi_f) \\
&\quad \times \delta_{JJ'} \delta_{MM'} \langle JM \lambda_{f_1} \lambda_{f_2} | T(s, t) | JM \rangle \\
&= \sqrt{\frac{2J+1}{4\pi}} D_{M\lambda}^{J*}(\phi_f, \theta_f, -\phi_f) \langle \lambda_{f_1} \lambda_{f_2} | T(s, t) | M \rangle \\
&= \sqrt{\frac{2J+1}{4\pi}} D_{M\lambda}^{J*}(\phi_f, \theta_f, -\phi_f) A_{\lambda_{f_1} \lambda_{f_2}}. \tag{4.51}
\end{aligned}$$

In a particle decay the angular momentum and the center-of-mass energy are fixed. The helicity amplitude $A_{\lambda_{f_1} \lambda_{f_2}}$ must be rotationally invariant (no

dependence on M) and therefore it can only depend on the helicities of the final state particles.

In experiments the helicities of the final state particles usually cannot be measured. In that case we have to sum over the helicities:

$$\langle f | T_{\mathcal{P}} | \Xi \rangle = \sum_{\lambda_{f_1} \lambda_{f_2}} \sqrt{\frac{2J+1}{4\pi}} D_{M\lambda}^{J*}(\phi_f, \theta_f, -\phi_f) A_{\lambda_{f_1} \lambda_{f_2}}. \quad (4.52)$$

4.6.2.1 Sequential two-body decay

In the next step we want to describe a sequential two-body decay. A particle Ξ decays to an intermediate resonance R with spin s_R and helicity λ_R and a final state particle f_3 . The resonance R in turn decays to the final state particle f_1 and f_2 . For simplicity we assume that the helicities λ_i of the final state particles and the helicity of the decaying particle λ_{Ξ} are known. Otherwise we would have to sum over them. Then the sequential decay amplitude can be written as:

$$\begin{aligned} A_{\Xi}^{(f_1 f_2) R f_3} &= \sum_{\lambda_R} \langle \theta_R \phi_R, \lambda_{f_1} \lambda_{f_2} | T_{\mathcal{P}} | s_R \lambda_R \rangle \\ &\quad \times \langle \theta_{\Xi} \phi_{\Xi}, \lambda_R \lambda_{f_3} | T_{\mathcal{P}} | s_{\Xi} \lambda_{\Xi} \rangle \\ &= \sqrt{\frac{2s_{\Xi}+1}{4\pi}} D_{\lambda_R \lambda_{f_3}}^{s_{\Xi}*}(\phi_{\Xi}, \theta_{\Xi}, -\phi_{\Xi}) A_{\lambda_R \lambda_{f_3}}^{\Xi} \\ &\quad \times \sum_{\lambda_R} \sqrt{\frac{2s_R+1}{4\pi}} D_{\lambda_R \lambda_f}^{s_R*}(\phi_R, \theta_R, -\phi_R) A_{\lambda_{f_1} \lambda_{f_2}}^R. \end{aligned} \quad (4.53)$$

The angles θ_R , ϕ_R and θ_{Ξ} , ϕ_{Ξ} are measured in the respective rest frames of the decay of R and the decay of Ξ . This is illustrated in fig. 4.12. Equation (4.53) is the decay amplitude for a resonating state in the final state particles f_1 and f_2 . The coherent sum of the amplitude over all possible intermediate states gives the total decay amplitude.

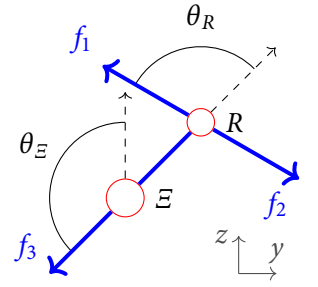


Figure 4.12: Sequential two-body decay. The angles are measured in the rest frame of the respective decay.

5

RESONANCES

In the previous chapter we focused on the kinematic constraints imposed by four-momentum and angular momentum conservation on scattering processes and particle decays. In this chapter we spotlight the dynamics of particle scattering and decay induced by the underlying interaction. We will shortly discuss what a resonance is and motivate afterwards the most common parameterizations: The Breit-Wigner (section 5.2) and Flatté formula (section 5.3). A Breit-Wigner parametrization is suitable for narrow and isolated resonances and the Flatté parametrization is used for resonances that are located close to the threshold of a decay channel.

5.1 WHAT IS A RESONANCE?

Today this question is still under discussion and a comprehensive overview is beyond the scope of this thesis. Nevertheless we want to give a quick introduction without any claim for completeness. We mainly follow Martin & Spearman [21].

The basic idea is that the transition matrix $\langle \alpha_f | T_{\mathcal{P}} | \alpha_i \rangle$ is a complex analytic function which is defined all over the Mandelstam plane (fig. 4.3). The behavior of the amplitude in the physical regions is defined by its structure in the unphysical regions. This is the so-called Mandelstam hypothesis [20–22]. Previously we introduced the expansion of the transition matrix in partial waves. Instead of the transition matrix we refer to its partial wave amplitudes in the following. Furthermore we assume that we have a elastic scattering process $AB \rightarrow AB$ of spin-less particles. Then the process can be described by one kinematic variable. We choose the Mandelstam variable s and denote the partial wave amplitudes of $\langle \alpha_f | T_{\mathcal{P}} | \alpha_i \rangle$ with $A_{if}^J(s)$. We drop the indices in the following.

A resonance is considered to be a pole of $A^J(s)$ in the complex energy plane. We have to evaluate $A^J(s)$ for complex values of s and therefore we have to evaluate the square-root of the break-up momentum eq. (4.3) which in turn reduces to the complex square-root of s . The complex square-root function is multivalued in the complex plane with sets of solutions which differ by integer multiples of $\pm i\pi$. Figure 5.1 shows the complex energy plane and the argument of the complex square root function. The physical region is along the real s -axis starting from threshold s_{th1} . The domains with one set of solutions are the so-called Riemann sheets. With each threshold the number of Riemann sheets doubles. Above the elastic threshold s_{th1} there are two solutions of the

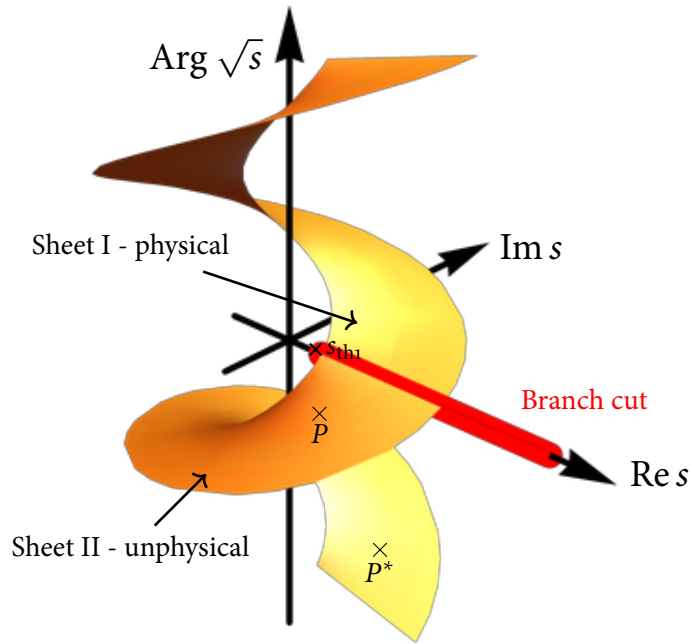


Figure 5.1: Argument of the complex square-root function. The domains with ambiguous solutions are so-called Riemann sheets. The red line indicates the physical region starting from threshold. Resonances are pairs of singularities on the second sheet.

square-root function, and therefore two sheets. The first and second sheet are conventionally labeled by physical and unphysical sheet. As mentioned before, resonances are considered to be poles of the transition amplitude in the complex energy plane. On the real axis poles are possible only below the threshold. These are identified as bound states. Resonances are poles above the threshold with a negative imaginary part. We consider a pole P at $s_P = s_R - i\gamma$. Since a resonant state has to decay with time according to $e^{-itE} = e^{-it\sqrt{s_P}}$ the pole position must have a negative imaginary part¹ and therefore the pole reside on the unphysical sheet. Due to unitarity each pole has a complex conjugate partner². Since this pole is far away from the real axis (compare with fig. 5.1) we neglect its influence.

The main challenge for spectroscopy is to determine the landscape of singularities in the complex energy plane from its 'projection' to the real energy axis for a certain process. If the singularities are known, their influence on other processes can be calculated. Yet the determination of the pole position can be difficult and we have to construct models that describe the cross section along the physical region depending on the singularities close by. Common problems are ambiguities in the description and model dependencies.

In the most simple case of a resonance far away from any thresholds and separated from other resonances, the resonance shape is well described by a

¹ The complex square root can be separated into real and imaginary part:
 $\sqrt{2s_P} = \sqrt{|s_P| + s_R + i \operatorname{sgn}(\gamma)} \sqrt{|s_P| - s_R}$.

² From unitarity follows that $A(s) = A^*(s^*)$.

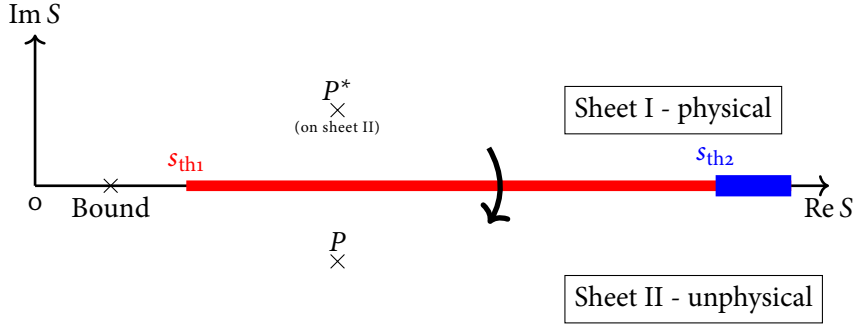


Figure 5.2: Complex energy plane. The physical region for an elastic scattering process $AB \rightarrow AB$ opens at s_{th1} . Below threshold poles can exist on the real axis and are identified as AB bound states. Poles above the threshold reside on the unphysical sheet. A resonance pole R and its complex conjugate partner on the unphysical sheet are sketched. The unphysical sheet is reached from the physical sheet by crossing the branch cut from above. At the threshold to the inelastic region s_{th2} another pair of Riemann sheets opens up.

Breit-Wigner formula (see section 5.2) which can be used to extract the pole position. The width is then given by the imaginary part of the pole position and the mass is given by the real part. Another special case is a resonance that is located close to a channel threshold but isolated from other resonances. Such a case is usually approximated by the Flatté formula (section 5.3). We discuss both cases in the following. In general the resonance shape on the real axis can be significantly distorted from a Breit-Wigner shape depending on the presence of thresholds and other resonances close by.

5.2 THE BREIT-WIGNER ANSATZ

Originally the Breit-Wigner model was developed by Breit & Wigner [31] for slow neutron capture in nuclei. We give a short derivation based on the ideas of the previous section and illustration fig. 5.2. We consider a pole P at position $s_P = s_R - i\gamma$ and assume that resonances are poles of first order in $A^J(s)$. Then $A^J(s)$ diverges close to the pole with $\mathcal{O}(1/(s - s_P))$ and we parametrize it as:

$$A^J(s) = \frac{g(s)}{(s - s_P)}. \quad (5.1)$$

According to the Mandelstam hypothesis $A^J(s)$ is an analytic function and therefore $g(s)$ is analytic and without poles. We require furthermore that $g(s_P) \neq 0$. The value of $g(s)$ close to the pole can be approximated by an expansion around $s = s_P$:

$$\begin{aligned} g(s) &= g(s_P) + (s - s_P) \left. \frac{dg(s)}{ds} \right|_{s_P} + \mathcal{O}(s^2) \\ &= g(s_P) + (s - s_R + i\gamma) g'(s_P) + \mathcal{O}(s^2). \end{aligned} \quad (5.2)$$

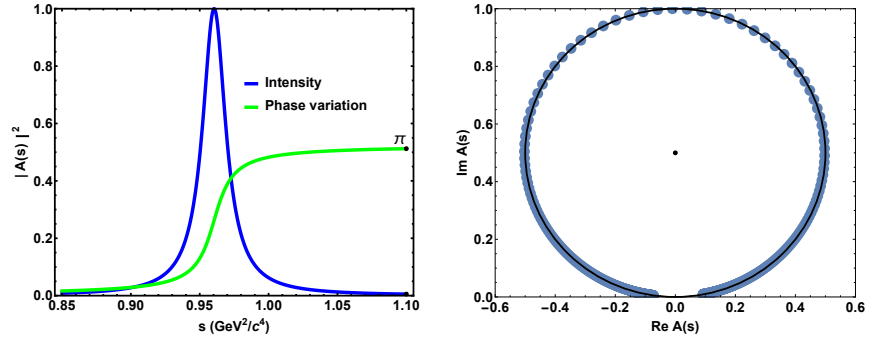


Figure 5.3: Breit-Wigner model for an isolated resonance with a mass of 0.98 GeV and a width of 20 MeV. The intensity with phase variation by $\pi/2$ at the resonance pole is on the left and the Argand diagram on the right.

Using eq. (5.1) we find:

$$A^J(s) = \frac{g(s_{\mathbf{P}})}{s - s_{\mathbf{P}}} + g'(s_{\mathbf{P}}) + \mathcal{O}(s) \approx \frac{g(s_{\mathbf{P}})}{s - s_{\mathbf{P}}}. \quad (5.3)$$

In a certain proximity around $s_{\mathbf{P}}$ the function $g(s)$ is analytic without poles and therefore the term $g'(s_{\mathbf{P}})$ can be neglected. In the context of resonances the approximation is valid for narrow resonances (γ small) and for real (physical) s close to $s_{\mathbf{R}}$. From the half width maximum of the intensity $|A^J(s)|^2$ one can derive the connection between the apparent width along the real axis, denoted by Γ , and the imaginary part of the pole position γ [21, Chapter 8.3.1]:

$$\Gamma = \gamma / \sqrt{s_{\mathbf{R}}}. \quad (5.4)$$

This leads to the well-known Breit-Wigner formula:

$$A^J(s) \approx \frac{-g(s_{\mathbf{P}})}{s_{\mathbf{R}} - s - i\sqrt{s_{\mathbf{R}}}\Gamma}. \quad (5.5)$$

The phase variation can be calculated from eq. (5.5):

$$\tan \delta(s) = \frac{\text{Im}(A^J(s))}{\text{Re}(A^J(s))} = \left(\frac{-\gamma}{s_{\mathbf{R}} - s} \right). \quad (5.6)$$

The resonance shape and its phase variation are shown in fig. 5.3(a). At the position of the resonance the phase rapidly increases by π with a slope depending on the resonance width. A different representation of the phase variation is shown in fig. 5.3(b). The so-called Argand diagram shows the imaginary part versus the real part of the amplitude. In the simple case we are dealing with, the curve follows the unit circle. This is a direct consequence of the unitarity condition of the S -matrix (which is automatically fulfilled since the S -matrix is in this case simply a complex number).

The phase variation of π at the position of the resonance and the pole in the transition matrix are directly connected to each other. Mathematically it is possible to prove that a simple pole in a complex analytical function corresponds to a phase change of π at the position of the pole [21, Chapter 6.1].

In this simple derivation some aspects of particle decays were not considered. Firstly the amplitude in eq. (5.5) is not Lorentz invariant and secondly the angular momentum barrier is not taken into account. These issues are considered in the parametrization suggested by the PDG [7]:

$$A^J(s) = -\frac{g^{i \rightarrow R} g_{R \rightarrow f}}{m_R^2 - s + i\sqrt{s}\Gamma(s)}. \quad (5.7)$$

The mass depended width $\Gamma(s)$ is given by:

$$\Gamma(s) = \Gamma_R \left(\frac{q}{q_R} \right)^{2J+1} \frac{F_J^2(q, q_0)}{F_J^2(q_R, q_0)}. \quad (5.8)$$

The break-up momentum $q = q(s)$ is defined in eq. (4.3) and the Blatt-Weisskopf angular barrier factors $F_J^2(q, q_0)$ are discussed in section 5.4. The coupling constants for the production and decay g_i are related to the partial width Γ_i via:

$$g_{R \rightarrow c} = \frac{1}{q_c^J F_J(q_c, q_0)} \sqrt{\frac{m_R \Gamma_{R \rightarrow c}}{\rho_c}}. \quad (5.9)$$

The last relation holds for narrow, isolated resonances.

Equation (5.7) describes the resonance structure along the real s axis close to the pole position and with the assumption that all (other) poles and thresholds are sufficiently far away. In practice these assumptions are strictly fulfilled only in very rare cases. Nevertheless the Breit-Wigner model serves as a good approximation in many cases.

5.3 THE FLATTÉ FORMALISM

We want to discuss a slightly more complicated situation which involves a resonance close to a channel threshold. The S matrix is therefore a 2×2 matrix with one resonance pole. The difficulty is to parametrize the S -matrix in such a way that unitarity is preserved. A correct treatment in that respect is usually done using the K -Matrix formalism [21, Chapter 4]. Since this is beyond the scope of this thesis we restrict ourselves to the result. The so-called Flatté formula [32] was firstly introduced to describe $\pi\eta$ and $K\bar{K}$ states close to the $K\bar{K}$ threshold. We use a slightly different version:

$$A_{2ch}^J(s) = -\frac{g_{a \rightarrow R} g_{R \rightarrow b}}{m_R^2 - s + i\sqrt{s}/m_R (g_1^2 \rho_1 + g_2^2 \rho_2)}. \quad (5.10)$$

The coupling constants are denoted by g_i and the phase-space factor ρ_i is given in eq. (4.5). The resonance shape for both channels and the Argand diagram are shown in fig. 5.4. At the $K\bar{K}$ threshold a kink is visible in the intensity of the

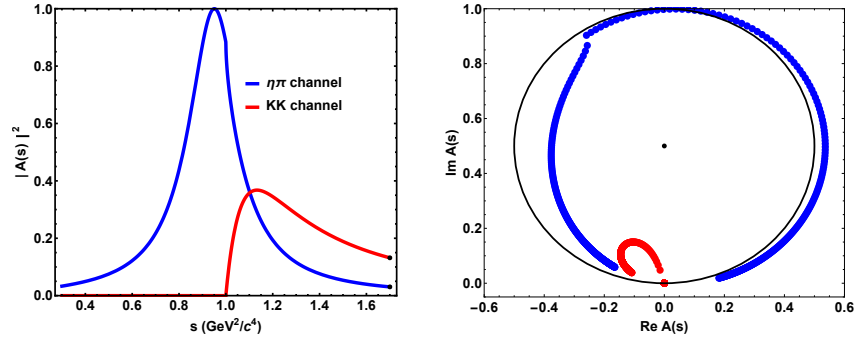


Figure 5.4: Flatté model for a two-channel resonance. The resonance pole is close to the $K\bar{K}$ threshold and couples strongly to $K\bar{K}$ and to the second channel $\pi\eta$. The intensity of both channels is shown on the right and the Argand diagram on the left.

second channel $\eta\pi$. In the Argand diagram the curve for the second channel drifts away from the unitarity circle after the opening of the $K\bar{K}$ channel.

5.4 BLATT-WEISSKOPF BARRIER FACTORS

As mentioned before, the Breit-Wigner Ansatz assumes a point-like object. An extended object introduces a centrifugal barrier which leads in general to a reduced resonance width. The radial Schrödinger equation in absence of a Coulomb potential and for distances larger than the size of the barrier potential is given by:

$$\frac{d^2}{dz^2} \psi(z) - \frac{J(J+1)}{r^2} \psi(z) = \psi(z). \quad (5.11)$$

The parameter z should be seen as normalized distance. As a measure for the distance we use the break-up momentum q , as defined in eq. (4.3), and we normalize it to the range of the interaction q_0 . The range of interaction is in turn approximated by the size of the object and we choose $q_0 = 1/R$ with the meson size R . Therefore, z is defined as:

$$z = \frac{q}{q_0}. \quad (5.12)$$

In principle the parameter q_0 depends on the resonance. Practice shows that its effect is rather small.

The solutions for eq. (5.11) are proportional to the spherical Hankel functions $h_J(z)$ [33, Chapter 11.7]:

$$\psi(z) \propto z h_J^{(1)}(z). \quad (5.13)$$

The form factor $F_J(z)$ is related to Hankel functions via

$$F_J^2(z) = \frac{z^2 |h_J^{(1)}(z)|^2}{|h_J^{(1)}(1)|^2} \quad (5.14)$$

which leads to the following expressions for angular momenta up to three:

$$\begin{aligned} F_0^2(z) &= 1 \\ F_1^2(z) &= \frac{z}{z+1} \\ F_2^2(z) &= \frac{13z^2}{(z-3)^2 + 9z} \\ F_3^2(z) &= \frac{277z^3}{z(z-15)^2 + 9(2z-5)^2}. \end{aligned} \quad (5.15)$$

This type of parametrization of the angular momentum barrier was introduced by Blatt & Weisskopf [34]. Further details can be found in [28, 35].

6

QUANTUM ENTANGLED $D^0\bar{D}^0$ DECAYS

We analyze D^0 mesons produced in the strong decay of $\psi(3770)$ to $D^0\bar{D}^0$. The $\psi(3770)$ is an excited $c\bar{c}$ state which hadronizes into a pair of D^0 mesons, as sketched in fig. 6.1. The D^0 mesons are produced in a quantum entangled state. In contrast to an isolated decay, this has implication on the decay rate since fundamental physical conservation laws needs to hold for the combined $D^0\bar{D}^0$ decay amplitude, not just for the decay amplitude of one D^0 . We mention especially the conservation of charge-parity (CP) which we assume to be strictly conserved in the D^0 system. We follow the phase convention

$$CP|D^0\rangle = -|\bar{D}^0\rangle \quad (6.1)$$

and denote the transition amplitude of an isolated D^0 decay $\langle j|\mathcal{H}|D^0\rangle$ by \mathcal{A}_j . From CP conservation follows:

$$\begin{aligned} \mathcal{A}_j &= \langle j|\mathcal{H}|D^0\rangle = -\langle \bar{j}|\mathcal{H}|\bar{D}^0\rangle = -\bar{\mathcal{A}}_{\bar{j}} \\ \bar{\mathcal{A}}_{\bar{j}} &= \langle j|\mathcal{H}|\bar{D}^0\rangle = -\langle \bar{j}|\mathcal{H}|D^0\rangle = -\mathcal{A}_{\bar{j}}. \end{aligned} \quad (6.2)$$

In case that j is a CP eigenstate we have $j = \bar{j}$ and we have to multiply by the CP eigenvalue of the final state. Another useful definition is the amplitude ratio of D^0 and \bar{D}^0 to the same final state:

$$\lambda_j = \frac{\mathcal{A}_j}{\bar{\mathcal{A}}_j} = -\sqrt{r_j}e^{-i\delta_j}. \quad (6.3)$$

The amplitudes \mathcal{A}_j depend on the phase-space position, only for two-body decays \mathcal{A}_j is constant. We use a normalization in which $|\mathcal{A}_j|^2$ integrated over the phase-space is the branching fraction of an isolated D^0 decay to the final state j . We denote those final states with $r_j \leq 1$ by j and its charge-conjugate with $r_{\bar{j}} > 1$ by \bar{j} .

A general introduction to charm physics is given in chapter 2. In the following we derive the decay amplitude of a quantum entangled $D^0\bar{D}^0$ pair and the influence of the quantum entanglement on branching fraction measurements. We follow [36, 37].

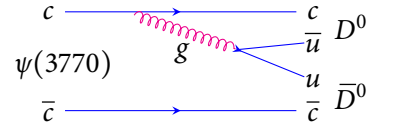


Figure 6.1: Feynman diagram for the decay of $\psi(3770)$ to $D^0\bar{D}^0$.

6.1 DECAY AMPLITUDE OF CORRELATED $D^0\bar{D}^0$ PAIRS

$D^0\bar{D}^0$ pairs can be produced in e^+e^- collisions: $e^+e^- \rightarrow D^0\bar{D}^0 + m\gamma + n\pi^0$. The reaction is illustrated in fig. 6.2. The $D^0\bar{D}^0$ pair has the charge parity quantum number $(-1)^{m+1}$. In our case the D^0 mesons are produced by the decay of a $\psi(3770)$ with quantum numbers $J^{PC} = 1^{--}$. The available phase-space does not allow for an additional pion and the emission of a photon is suppressed due to the heavy c -quark. D^0 mesons have quantum numbers $J^P = 0^-$ and the relative angular momentum between both D^0 mesons is therefore $L = 1$. In consequence $D^0\bar{D}^0$ are produced in a state of negative charge-parity. The wave function is therefore anti-symmetric:

$$|\psi(3770)\rangle = \frac{1}{\sqrt{2}} (|D^0\bar{D}^0\rangle - |\bar{D}^0D^0\rangle). \quad (6.4)$$

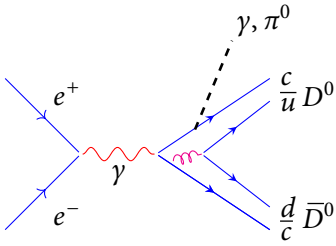


Figure 6.2: Production of $D^0\bar{D}^0$ pairs in e^+e^- reaction.

The decay is mediated by the decay operator \mathcal{H} . The transition matrix element for D^0 and \bar{D}^0 going to the final states i and j at decay times t_1 and t_2 respectively, is given by:

$$\begin{aligned} \mathcal{M}_{ij}(t_1, t_2) = & \frac{1}{\sqrt{2}} [\langle i | \mathcal{H} | D^0(t_1) \rangle \langle j | \mathcal{H} | \bar{D}^0(t_2) \rangle \\ & - \langle i | \mathcal{H} | \bar{D}^0(t_1) \rangle \langle j | \mathcal{H} | D^0(t_2) \rangle]. \end{aligned} \quad (6.5)$$

The transition actually only depends on the decay time difference $\Delta t = t_2 - t_1$. We use the time-evolution of the physical states $|D^0(t)\rangle$, as given in eq. (2.3), to calculate the norm of the transition matrix element [7, Chapter 13.1]:

$$\begin{aligned} |\mathcal{M}_{ij}(\Delta t)|^2 = & \frac{\Gamma}{4} e^{-\Gamma|\Delta t|} [(|a_+|^2 + |a_-|^2) \cosh(y\Gamma\Delta t) \\ & + (|a_+|^2 - |a_-|^2) \cos(x\Gamma\Delta t) \\ & - 2 \operatorname{Re}(a_+^* a_-) \sinh(y\Gamma\Delta t) \\ & + 2 \operatorname{Im}(a_+^* a_-) \sin(x\Gamma\Delta t)]. \end{aligned} \quad (6.6)$$

The mixing parameters (x, y) and the CP violation parameters (q, p) were introduced in chapter 2. We use the abbreviations

$$a_+ = \bar{\mathcal{A}}_j \mathcal{A}_i - \mathcal{A}_j \bar{\mathcal{A}}_i \quad \text{and} \quad a_- = -\frac{q}{p} \bar{\mathcal{A}}_j \bar{\mathcal{A}}_k + \frac{p}{q} \mathcal{A}_j \mathcal{A}_k. \quad (6.7)$$

The BESIII experiment does not give access to the D^0 decay time and therefore we are interested on the time-integrated transition matrix element. The integration of eq. (6.6) over the D^0 decay time difference yields:

$$\begin{aligned} |\mathcal{M}_{ij}|^2 = & \int_{-\infty}^{\infty} d(\Delta t) |\mathcal{M}_{ij}(\Delta t)|^2 \\ = & \frac{(|a_+|^2 + |a_-|^2)}{1 - y^2} + \frac{(|a_+|^2 - |a_-|^2)}{1 + x^2} \\ \approx & |a_+|^2 = |\bar{\mathcal{A}}_j \mathcal{A}_i - \mathcal{A}_j \bar{\mathcal{A}}_i|^2. \end{aligned} \quad (6.8)$$

In eq. (6.6) we choose the normalization so that $|\mathcal{M}_{ij}|^2$ and $|\mathcal{A}_i|^2$ are branching fractions if integrated over the phase-space. The mixing parameters x and y are of the order $\mathcal{O}(10^{-3})$ and can be neglected in second order.

Using eq. (6.3) we can write eq. (6.8) as:

$$\begin{aligned} |\mathcal{M}_{ij}|^2 &\approx |\bar{\mathcal{A}}_j\mathcal{A}_i - \mathcal{A}_j\bar{\mathcal{A}}_i|^2 = 2|\bar{\mathcal{A}}_i\bar{\mathcal{A}}_j(\lambda_i - \lambda_j)|^2 \\ &= |\bar{\mathcal{A}}_i|^2|\bar{\mathcal{A}}_j|^2[\lambda_i^2 + \lambda_j^2 - \lambda_i^*\lambda_j - \lambda_i\lambda_j^*] \\ &= |\bar{\mathcal{A}}_i|^2|\bar{\mathcal{A}}_j|^2[r_i + r_j - \sqrt{r_i r_j}(e^{i(\delta_i - \delta_j)} + e^{-i(\delta_i - \delta_j)})] \\ &= |\bar{\mathcal{A}}_i|^2|\bar{\mathcal{A}}_j|^2[r_i + r_j - \sqrt{r_i r_j}2\cos(\delta_i - \delta_j)]. \end{aligned} \quad (6.9)$$

This amplitude is used for the Dalitz plot analysis of $D^0 \rightarrow K_s^0 K^+ K^-$ in chapter 12. In case that one of the D^0 mesons decays to a conjugate final state we derive in the same way:

$$\begin{aligned} |\mathcal{M}_{i\bar{j}}|^2 &\approx |\bar{\mathcal{A}}_j\mathcal{A}_i - \mathcal{A}_j\bar{\mathcal{A}}_i|^2 = |\mathcal{A}_i\mathcal{A}_j - \bar{\mathcal{A}}_j\bar{\mathcal{A}}_i|^2 \\ &= |\bar{\mathcal{A}}_i|^2|\bar{\mathcal{A}}_j|^2[1 + r_i r_j - \sqrt{r_i r_j}2\cos(\delta_i + \delta_j)]. \end{aligned} \quad (6.10)$$

The ratio of the decay amplitudes of D^0 and \bar{D}^0 to the same final state j denoted by λ_j depends on the type of final state. We distinguish three different types:

- **Hadronic final states** f that can be reached from D^0 and \bar{D}^0 . For example a D^0 can decay to the final states $K^- \pi^+$ via a Cabibbo-favoured (CF) ($V_{cs}V_{ud}$) transition while the \bar{D}^0 decays via a doubly Cabibbo-suppressed (DCS) ($V_{cd}V_{us}$) transition. This category also includes self-conjugate final states, in particular the decay $D^0 \rightarrow K_s^0 K^+ K^-$.
- The decay amplitudes of D^0 and \bar{D}^0 are equal for **CP eigenstates** S^\pm (in the limit of conserved CP symmetry). CP eigenstates are for example $\pi^+ \pi^-$ and $K^+ K^-$.
- **(Semi-) leptonic D^0 decays** l^+ unambiguously determine the flavour of the decaying meson. They are accessible by either D^0 or \bar{D}^0 . It is also possible that a D^0 oscillated to a \bar{D}^0 beforehand, or vice versa.

For those categories we list magnitude and phase of the ratio of D^0 to \bar{D}^0 amplitude to the same final states in table 6.1.

Table 6.1: Magnitudes and phases of the ratio λ_j of D^0 to \bar{D}^0 amplitude to the same final states [37].

Final state j	r_j	δ_j
f	r_f	δ_f
\bar{f}	r_f	δ_f
l^+	0	-
S^+	1	π
S^-	1	0

6.2 BRANCHING-FRACTIONS IN ENTANGLED $D^0\bar{D}^0$ DECAYS

The branching fraction of a D^0 meson decaying to a final state f is influenced, with respect to the decay of an isolated D^0 , by the quantum entanglement between D^0 and \bar{D}^0 . The branching fraction of an isolated D^0 is what we want to measure. This can be achieved by a so-called **single-tag** or **double-tag** measurements. We introduce those in the following.

The **single-tag** measurement is based on the reconstruction of the signal decay and the normalization to the number of $D^0\bar{D}^0$ decays. The number of

$D^0\bar{D}^0$ decays is obtained from the integrated luminosity and the corresponding cross section. The transition matrix element that one D^0 goes to a specific channel j and \bar{D}^0 goes to any final state is given by:

$$\begin{aligned} |\mathcal{M}_{jX}|^2 &= \sum_i (|\mathcal{M}_{ji}|^2 + |\mathcal{M}_{\bar{j}\bar{i}}|^2) \\ &= \sum_i |\bar{\mathcal{A}}_j|^2 |\bar{\mathcal{A}}_i|^2 [1 + r_i + r_j + r_i r_j - 2\sqrt{r_i r_j} [\cos(\delta_i - \delta_j) + \cos(\delta_i + \delta_j)]] \\ &= \sum_i |\bar{\mathcal{A}}_j|^2 |\bar{\mathcal{A}}_i|^2 [1 + r_i + r_j + r_i r_j - 4\sqrt{r_i r_j} \cos \delta_i \cos \delta_j]. \end{aligned} \quad (6.11)$$

The transition matrix element $|\mathcal{M}_{jX}|^2$, the amplitudes of isolated D^0 decays \mathcal{A}_j as well as the parameters r_i and δ_i implicitly depend on the phase-space position. We obtain branching fractions via integration over the phase-space:

$$\begin{aligned} \mathcal{B}_{ij} &= \int d\xi_i \int d\xi_j |\mathcal{M}_{ij}|^2 \\ \mathcal{B}_i &= \int d\xi_i |\mathcal{A}_i|^2. \end{aligned} \quad (6.12)$$

The infinitesimal phase-space element of channel j is denoted by $d\xi_j$. For the parameters r_i and δ_i we calculate averaged values

$$\langle w_i \rangle = \frac{\int d\xi_i w_i |\mathcal{M}_{ij}|^2}{\int d\xi_i |\mathcal{M}_{ij}|^2}, \quad (6.13)$$

with $w_i = (r_i, \delta_i)$ and can then rewrite eq. (6.11):

$$\mathcal{B}_{jX} = \sum_i \bar{\mathcal{B}}_j \bar{\mathcal{B}}_i [1 + \langle r_i \rangle + \langle r_j \rangle + \langle r_i \rangle \langle r_j \rangle - \langle 2\sqrt{r_i} \cos \delta_i \rangle \langle 2\sqrt{r_j} \cos \delta_j \rangle]. \quad (6.14)$$

The branching fractions of isolated D^0 decays sum up to one:

$$\sum_i (\bar{\mathcal{B}}_i + \bar{\mathcal{B}}_i \langle r_i \rangle) = \sum_i (\bar{\mathcal{B}}_i + \mathcal{B}_i) = 1, \quad (6.15)$$

where the mixing parameter y can be expressed as:

$$y = 2 \sum_i \bar{\mathcal{B}}_i \langle \sqrt{r_i} \cos \delta_i \rangle. \quad (6.16)$$

This relation is derived in appendix A.3. Using those expressions eq. (6.14) can be written as:

$$\begin{aligned}
\mathcal{B}_{jX} &= \bar{\mathcal{B}}_j \left[\sum_i (\bar{\mathcal{B}}_i + \bar{\mathcal{B}}_i \langle r_i \rangle) + \langle r_j \rangle \sum_i (\bar{\mathcal{B}}_i + \bar{\mathcal{B}}_i \langle r_i \rangle) \right. \\
&\quad \left. - \langle 2\sqrt{r_j} \cos \delta_j \rangle \sum_i \bar{\mathcal{B}}_i \langle 2\sqrt{r_i} \cos \delta_i \rangle \right] \\
&= \bar{\mathcal{B}}_j \left[1 + \langle r_j \rangle - \langle 2\sqrt{r_j} \cos \delta_j \rangle \sum_i \bar{\mathcal{B}}_i \langle 2\sqrt{r_i} \cos \delta_i \rangle \right] \\
&= \bar{\mathcal{B}}_j [1 + \langle r_j \rangle - \langle 2\sqrt{r_j} \cos \delta_j \rangle y]. \tag{6.17}
\end{aligned}$$

The branching fraction in correlated decays \mathcal{B}_{jX} can be measured by:

$$\mathcal{B}_{jX} = \frac{N_j}{N_{D\bar{D}} \times \epsilon_j}, \tag{6.18}$$

with the number of $D^0\bar{D}^0$ decays $N_{D\bar{D}}$ and the signal yield N_j . From eq. (6.18) and eq. (6.17) we find that the branching fraction of an isolated D^0 decay can be obtained from a correlated decay via:

$$\bar{\mathcal{B}}_j = \frac{N_j}{N_{D\bar{D}} [1 + \langle r_j \rangle - y \langle 2\sqrt{r_j} \cos \delta_j \rangle] \times \epsilon_j}, \tag{6.19}$$

where the reconstruction and selection efficiency of a final state j is denoted by ϵ_j . We will use this formula for the measurement of the $D^0 \rightarrow K_s^0 K^+ K^-$ branching fraction which is discussed in chapter 13.

For completeness we explain in the following the double-tag measurement of branching fractions. The branching fraction of a pair of correlated $D^0\bar{D}^0$ mesons to a final state (i, \bar{j}) can be obtained from eq. (6.10) and can be measured using the signal yield $N_{i\bar{j}}$ and the number of $D^0\bar{D}^0$ decays:

$$\mathcal{B}_{i\bar{j}} = \int d\xi_i \int d\xi_{\bar{j}} |\mathcal{M}_{i\bar{j}}|^2 = \frac{N_{i\bar{j}}}{N_{D\bar{D}} \times \epsilon_{i\bar{j}}}. \tag{6.20}$$

The branching fraction of an isolated D^0 to a final state \bar{j} can be extracted by normalization to the single-tag inclusive branching fraction \mathcal{B}_{iX} , given in eq. (6.19):

$$\frac{\mathcal{B}_{i\bar{j}}}{\mathcal{B}_{iX}} = \frac{N_{i\bar{j}} \epsilon_i}{N_i \epsilon_{i\bar{j}}} = \frac{\bar{\mathcal{B}}_i \bar{\mathcal{B}}_j [1 + \langle r_i \rangle \langle r_j \rangle - \langle 2\sqrt{r_i r_j} \cos(\delta_i + \delta_j) \rangle]}{\bar{\mathcal{B}}_i [1 + \langle r_i \rangle - y \langle 2\sqrt{r_i} \cos \delta_i \rangle]}. \tag{6.21}$$

Finally we obtain:

$$\bar{\mathcal{B}}_j = \frac{N_{i\bar{j}} \epsilon_i}{N_i \epsilon_{i\bar{j}}} \times \underbrace{\frac{1 + \langle r_j \rangle - 2y \langle \sqrt{r_j} \cos \delta_j \rangle}{1 + \langle r_i \rangle \langle r_j \rangle - 2 \langle \sqrt{r_i r_j} \cos(\delta_i + \delta_j) \rangle}}_{f_{\text{corr}}}. \tag{6.22}$$

Depending on the final state (i, \bar{j}) the correction term f_{corr} can be neglected. For example in case of $(i, \bar{j}) = (K^-\pi^+, K^+\pi^-)$, we can use the experimental averages from table 7.1 to calculate f_{corr} . In this case the correction is $(0.338 \pm 0.004) \%$.

7

AMPLITUDE MODEL FOR $D^0 \rightarrow K_S^0 K^+ K^-$

We introduced the basic theoretical constructs for partial wave analysis in chapter 4 and the implications of the correlated decays of a pair of D^0 mesons in chapter 6. We now recap the important formulae and apply them to the decay $D^0 \rightarrow K_S^0 K^+ K^-$.

We analyze a data sample of $D^0 \bar{D}^0$ decays and we have to take into account the entanglement of both D^0 mesons. One D^0 decay, the so-called tag decay, is used to determine the flavour of the signal decay. From eq. (6.9) we get:

$$\begin{aligned}
 \left| \mathcal{M}_{(\text{tag})(K_S^0 K^+ K^-)} \right|^2 &= \left| \bar{\mathcal{A}}_{\text{tag}} \mathcal{A}_{K_S^0 K^+ K^-} - \mathcal{A}_{\text{tag}} \bar{\mathcal{A}}_{K_S^0 K^+ K^-} \right|^2 \\
 &= \left| \bar{\mathcal{A}}_{\text{tag}} \left(\mathcal{A}_{K_S^0 K^+ K^-} - \lambda_{\text{tag}} \bar{\mathcal{A}}_{K_S^0 K^+ K^-} \right) \right|^2 \\
 &= |\bar{\mathcal{A}}_{\text{tag}}|^2 \left[\left| \mathcal{A}_{K_S^0 K^+ K^-} \right|^2 + r_{\text{tag}} \left| \bar{\mathcal{A}}_{K_S^0 K^+ K^-} \right|^2 \right. \\
 &\quad \left. - 2\sqrt{r_D} \left| \mathcal{A}_{K_S^0 K^+ K^-} \right| \left| \bar{\mathcal{A}}_{K_S^0 K^+ K^-} \right| \cos(\delta_{\text{tag}} - \delta_{K_S^0 K^+ K^-}) \right] \\
 &= |\bar{\mathcal{A}}_{\text{tag}}|^2 \left| \mathcal{A}_{K_S^0 K^+ K^-} \right|^2 \left[1 + r_{\text{tag}} r_{K_S^0 K^+ K^-} \right. \\
 &\quad \left. - 2\sqrt{r_{\text{tag}}} \sqrt{r_{K_S^0 K^+ K^-}} \cos(\delta_{\text{tag}} - \delta_{K_S^0 K^+ K^-}) \right]. \quad (7.1)
 \end{aligned}$$

The final state $K_S^0 K^+ K^-$ is a self-conjugate final state and therefore D^0 and \bar{D}^0 amplitude are linked via [17]:

$$\mathcal{A}_{K_S^0 K^+ K^-} (m_{K^0 K^+}^2, m_{K^0 K^-}^2) = \bar{\mathcal{A}}_{K_S^0 K^+ K^-} (m_{K^0 K^-}^2, m_{K^0 K^+}^2). \quad (7.2)$$

Note that $\mathcal{A}_{K_S^0 K^+ K^-}$ and $\bar{\mathcal{A}}_{K_S^0 K^+ K^-}$ are the same function evaluated at different phase-space positions.

We use flavour specific tag channels as listed in table 10.1. For those channels λ_{tag} , see eq. (6.3), has the same magnitude R_D but the phase depends on the channel. Experimental averages are listed in table 7.1. As mentioned, the signal channel $K_S^0 K^+ K^-$ is a self-conjugate final state and, as we will see, its substructure is a mixture of negative and positive CP eigenstates as well as non- CP states. Therefore, it is hard to predict the ratio $\lambda_{K_S^0 K^+ K^-}$. In particular the interference term in eq. (7.1) can influence the result.

Table 7.1: Charm mixing averages from HFAG [38]. Values in [%].

Parameter	Value
x	0.53 ± 0.17
y	0.63 ± 0.09
R_D	0.350 ± 0.004
$\langle R_D^{K^- \pi^+ \pi^0} \rangle$	0.164 ± 0.027
$\delta_{K\pi} [^\circ]$	10 ± 11
$\delta_{K\pi\pi^0} [^\circ]$	17 ± 23

The decay amplitude $\mathcal{A}_{K_S^0 K^+ K^-}$ is modeled by the coherent sum of intermediate resonances. The D^0 as well as all final state particles are spin-less ($J = 0$) and have therefore helicity zero ($\lambda_i = 0$). In a three-body final state only one intermediate resonance is possible and since we have only spin-less particles the helicity of the intermediate resonance is fixed to zero. The formula for sequential two-body decays from eq. (4.53) therefore simplifies to:

$$\begin{aligned} A_R^{(K_1 K_2)_R K_3} &= \sqrt{\frac{2s_R + 1}{4\pi}} D_{00}^{s_R}(\phi_R, \theta_R, -\phi_R) A_{00}^R \\ &\quad \times \sqrt{\frac{1}{4\pi}} D_{00}^0(\phi_D, \theta_D, -\phi_D) A_{00}^D \\ &= \frac{\sqrt{2s_R + 1}}{4\pi} A^R P_{s_R}(\cos \theta_R) A^D. \end{aligned} \quad (7.3)$$

We have used that the Legendre polynomials $P_J(\cos \theta)$ are a special case of the Wigner D-matrix for $\lambda = \lambda' = 0$ (see appendix A.1). The helicity amplitudes A^D and A^R describe the dynamics of the production and decay of the intermediate resonance R. We add the individual amplitudes for all possible intermediate states coherently to obtain the total amplitude for an isolated D^0 decay:

$$\begin{aligned} A_{K_S^0 K^+ K^-} &= \sum_R \frac{\sqrt{2s_R + 1}}{4\pi} A^D P_{s_R}(\cos \theta_R) A^R \\ &= \sum_J \frac{\sqrt{2J + 1}}{4\pi} A^D P_J(\cos \theta_R) \sum_{R_J} A^{R_J}. \end{aligned} \quad (7.4)$$

In the last step we reordered the summation to resemble a partial wave decomposition. The helicity amplitudes A^{R_J} depend on the center-of-mass energy of the subsystem in which the resonance occurs. The center-of-mass energy in each subsystem is given by the invariant masses

$$\begin{aligned} m_{K_S^0 K^-}^2 &= (p_{K_S^0} + p_{K^-})^2 \\ m_{K_S^0 K^+}^2 &= (p_{K_S^0} + p_{K^+})^2 \\ m_{K^+ K^-}^2 &= (p_{K^+} + p_{K^-})^2. \end{aligned} \quad (7.5)$$

From these invariant masses the helicity angle associated with each invariant mass can be calculated according to eq. (4.7). In principle these variables are identical to the Mandelstam variables, yet in particle decay it is difficult to assign them to s, t and u channel. As mentioned before only two variables are necessary to describe the decay: two invariant masses or one invariant mass and its associated helicity angle. We denote the set of variables that are chosen to describe the position in the Dalitz plot by ξ .

The next step is to construct models for the helicity amplitudes. In section 5.2 we have developed an ansatz for isolated resonances far away from thresholds. Most of the resonances that significantly contribute to the intensity of the final

state $K_s^0 K^+ K^-$ fulfill this requirement. These resonances are described by a Breit-Wigner model:

$$A^J(s) = -\frac{g_{i \rightarrow R} g_{R \rightarrow f}}{m_R^2 - s + i\sqrt{s}\Gamma(s)}. \quad (5.7)$$

The $a_0(980)$ and the $f_0(980)$ are a bit more complicated. The $a_0(980)$ and $f_0(980)$ are considered to be isospin partners with $I = 1$ and $I = 0$ and have a position close to the opening of the $K\bar{K}$ channel to which both of them couple strongly. In this case the channel $K\bar{K}$ as well as the second channels need to be taken into account. In case of the $f_0(980)$ the second channel is $\pi\pi$ and the $a_0(980)$ couples to $\eta\pi$. The charged a_0^+ and a_0^- are described using the Flatté formula:

$$A_{2ch}^J(s) = -\frac{g_{a \rightarrow R} g_{R \rightarrow b}}{m_R^2 - s + i\sqrt{s}/m_R (g_1^2 \rho_1 + g_2^2 \rho_2)}. \quad (5.10)$$

For the neutral resonances we introduce a third channel, since there is the $K^+ K^-$ threshold and close by the $K^0 \bar{K}^0$ threshold. We assume that the coupling to $K^- K^+$ and $K^0 \bar{K}^0$ are equal. Since the pole mass is below the $K\bar{K}$ threshold we have to evaluate the phase-space factor ρ close at threshold. We use a modified formula for the phase-space factor which has better analytic properties compared to eq. (4.5). The parametrization suggested by the PDG [7, Section 47.2.3] is given by:

$$i\rho_{12} = \begin{cases} -\frac{\hat{\rho}_{12}}{\pi} \log \left| \frac{1+\hat{\rho}_{12}}{1-\hat{\rho}_{12}} \right|, & s < 0 \\ -\frac{2\hat{\rho}_{12}}{\pi} \arctan \frac{1}{\hat{\rho}_{12}}, & 0 < s < s_{th} \\ -\frac{\hat{\rho}_{12}}{\pi} \log \left| \frac{1+\hat{\rho}_{12}}{1-\hat{\rho}_{12}} \right| + i\hat{\rho}_{12}, & s_{th} < s \end{cases} \quad (7.6)$$

where $\hat{\rho}_{12}$ is defined as

$$\hat{\rho}_{12}(s) = \frac{1}{16\pi} \frac{2\sqrt{|q_{12}(s)|^2}}{\sqrt{s}}. \quad (4.5)$$

This definition is also used to obtain an analytic function for the break-up momentum.

Part III

THE BESIII EXPERIMENT

The BESIII experiment is located at the Beijing Electron-Positron Collider. The accelerator is a e^+e^- storage ring located at the Institute of High Energy Physics in Beijing. It provides symmetric collisions in the energy range between 2.0 GeV and 4.6 GeV. The maximum luminosity of BEPCII is achieved at $\sqrt{s} = 3.773$ GeV. In April a luminosity of $1 \times 10^{33} \text{ cm}^{-2} \text{ s}^{-1}$ was surpassed. The detector measures charged track momenta with a relative precision of 0.5 % (@1.0 GeV) using a multi-wire drift chamber in a 1 T magnetic field. Electromagnetic showers are measured in a caesium iodide calorimeter with a relative precision of 2.5 % (@1.0 GeV) and a good particle identification is achieved by combining information from energy loss in the drift chamber, from the time-of-flight system and from the calorimeter. Muons can be identified using 9 layers of resistive plate chambers integrated in the magnet return yoke.

8

THE BEPCII STORAGE RING

The Beijing Electron-Positron Collider II (BEPCII) is a symmetric e^+e^- collider located at the Institute of High Energy Physics in Beijing. It is a major upgrade of its predecessor BEPC [39], which was in operation between 1989 and 2004. During the upgrade the collider was essentially rebuilt.

BEPCII is a double ring multi-bunch e^+e^- collider. It is designed to operate in the τ -charm region between 2.0 GeV and 4.6 GeV with a maximum luminosity of $1 \times 10^{33} \text{ cm}^{-2} \text{ s}^{-1}$ at $\sqrt{s} = 3.773 \text{ GeV}$. So far the luminosity was below the design value but in April the goal of $1 \times 10^{33} \text{ cm}^{-2} \text{ s}^{-1}$ was surpassed.

Electrons and positrons are accelerated to the nominal beam energy by a linear accelerator with a length of 202.4 m and are injected into the storage ring. The storage ring is illustrated in fig. 8.1. It has two rings with a circumference of 237.5 m which cross each other in the northern and southern interaction point. The crossing angle in the southern point where BESIII is located, is 11 mrad. The ring is equipped with 60 quadrupole magnets for beam focusing and 40 bending magnets. Very close to the southern interaction point two focusing magnets are installed to ensure a high luminosity as shown in fig. 9.1 (blue components).

The expected luminosity of an e^+e^- collider can be expressed by the beam aspect ratio r , the vertical envelope function β_y (both at the interaction point), the vertical beam-beam parameter ξ_y , the bunch number k_b and the beam current I_b [41]:

$$\mathcal{L}(\text{cm}^{-2} \text{ s}^{-1}) = 2.17 \times 10^{34} (1+r) \xi_y \frac{E(\text{GeV}) k_b I_b (\text{A})}{\beta_y^*(\text{cm})}. \quad (8.1)$$

A luminosity of $1 \times 10^{33} \text{ cm}^{-2} \text{ s}^{-1}$ [42] was reached with a configuration of 119 bunches and a beam current of 849 mA and 852 mA for the positron and electron beam, respectively. The beam-beam parameter was 0.0384.

More details of the accelerator are provided by [41, 43].

BEPCII had its first collisions in July of 2008 and physics data taking started in March of 2009. Since then, BEPCII has been producing reliably collisions for particle physics analysis for around 6 Month per year. During this time and during dedicated periods BEPCII is also used for synchrotron radiation experiments.

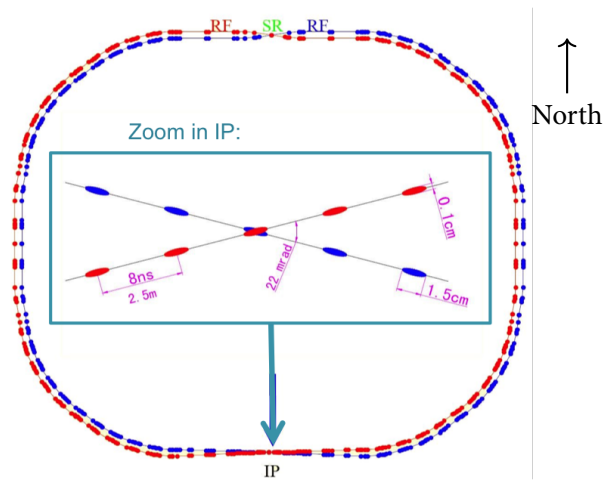


Figure 8.1: The BEPCII e^+e^- storage ring [40].

8.1 SYNCHROTRON RADIATION FACILITY

The Beijing Synchrotron Radiation Facility (BSRF) provides synchrotron radiation (SR) from ultraviolet and hard X-rays. 14 beam-lines provide experimental techniques like X-ray imaging and X-ray crystallography which are relevant for many other research areas like condensed matter physics, chemistry, material science, biology, geoscience and many more. During the dedicated SR operation, electrons are inserted into the outer ring with an energy of 2.5 GeV and only 250 mA. During that time the accelerator is tuned for a low emittance instead of a high current, which results in a higher brightness of the synchrotron source compared to the collision mode. A description of the BSRF can be found in [44].

THE BESIII DETECTOR

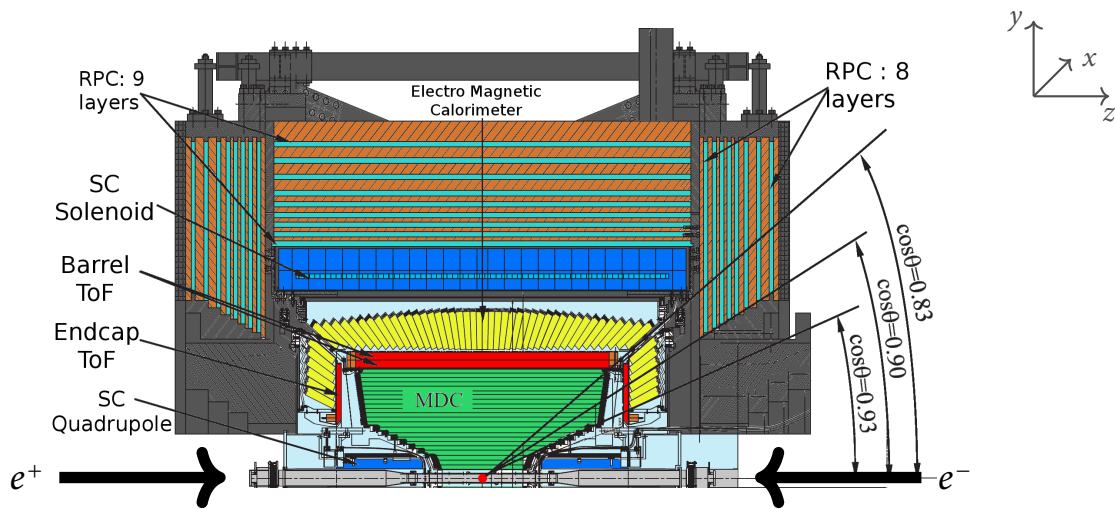


Figure 9.1: Vertical section of the BESIII detector along the beam-axis ($\cos \theta$ plane) [45].

The BESIII detector covers almost the full solid angle of 4π . The vertical section along the beam-line ($\cos \theta$ plane) is shown in fig. 9.1. In the ϕ plane the detector is symmetrical.

From inside to outside the experiment consists of a multi-wire drift chamber as central element, surrounded by a plastic-scintillator time-of-flight system and the electromagnetic calorimeter. Then follows the superconducting magnet with a field strength of 1 T and the outermost component is the muon system which is integrated into the magnet return yoke. In the following the individual detector components are described.

9.1 MULTI-WIRE DRIFT CHAMBER

The drift chamber is the central element of the detector. It measures charged tracks and their momenta in three dimensions. Using a measurement of the energy loss per length (dE/dx) it is possible to identify different particle species.

The chamber has cylindrical shape with an inner radius of 59 mm, an outer radius of 81 cm and a maximum length of 2.582 m. The inner part is designed to be removable in case of severe radiation damage and has a stepped shape to allow focusing quadrupole magnets be installed close to the interaction region.

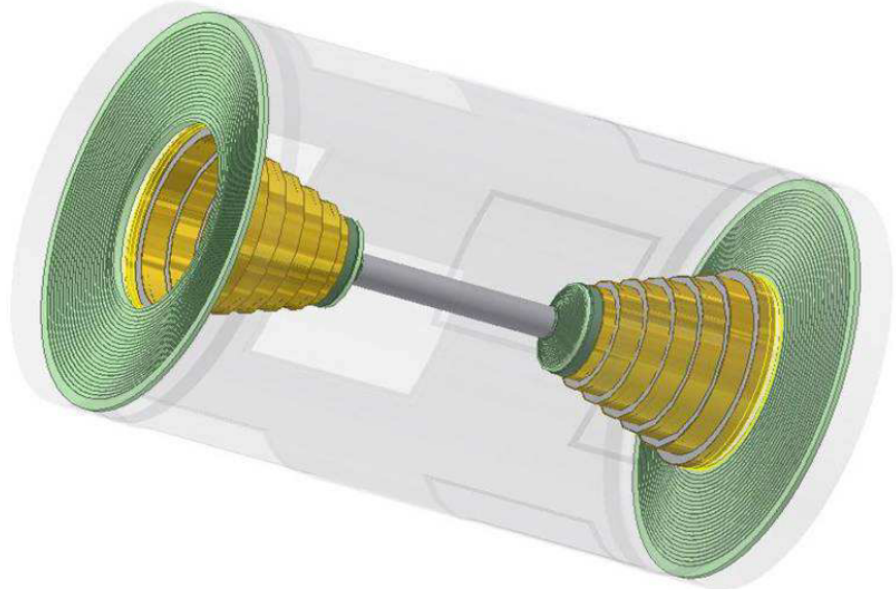


Figure 9.2: Schematic view of the multi-wire drift chamber [43].

This is done to produce the high luminosity. The whole chamber has 43 layers of sense wires with 6796 sense wires in total. These sense wire layers alternate with layers of field wires and are arranged in 11 super layers with 4 layers each (3 in the last super layer).

The precision of the momentum measurement depends on two parameters: the single wire resolution and the probability of multiple scattering. The wire resolution σ_x is $130 \mu\text{m}$ and the multiple scattering process is determined by the chamber design and the gas mixture. The gas mixture is on the one hand chosen to minimize the material budget and on the other hand to provide sufficient primary ionization for the dE/dx measurement. The optimal choice is a helium propane ($\text{He}/\text{C}_3\text{H}_8$) mixture in the ratio 60:40. The expected momentum resolution for equally spaced layers in an axial uniform magnetic field can be approximated by:

$$\frac{\sigma_{pt}}{p_t} = \sqrt{\left(\frac{\sigma_{pt}^{wire}}{p_t}\right)^2 + \left(\frac{\sigma_{pt}^{multiscat}}{p_t}\right)^2}. \quad (9.1)$$

The two terms can be expressed in terms of the single wire resolution σ_x and the radiation length X_0 of the total material in the chamber:

$$\frac{\sigma_{pt}^{wire}}{p_t} = \frac{3.3 \times 10^2 \times \sigma_x}{B \times L} \times p_t \times \sqrt{\frac{720}{n+5}} \quad (9.2)$$

$$\frac{\sigma_{pt}^{multiscat}}{p_t} = \frac{0.05}{B \times L} \times \sqrt{1.43 \frac{L}{X_0}} \left(1 + 0.038 \ln \frac{L}{X_0}\right). \quad (9.3)$$

where B is the magnetic field in Tesla, L the track length in meters, p_T the transversal momentum in GeV, and n the number of sense wire layers. For

a typical track of 1 GeV at 90° polar angle, σ_{pt}^{wire} and $\sigma_{pt}^{multiscat}$ are 0.32 % and 0.35 %. This leads to a momentum resolution of a typical track of 0.47 %.

The dE/dx resolution depends on fluctuations of the ionization process and recombination loss of electron-ion pairs. It is currently 5 % to 6 % [46]. Kaons and pions can be separated on a 3σ level up to momenta of ~ 770 MeV/c.

9.2 TIME-OF-FLIGHT SYSTEM

The next layer of the BESIII detector is the time-of-flight (TOF) system. It consists of a barrel part with two layers of plastic scintillator bars and an end cap part with one layer of plastic scintillator. The main task of the TOF system is particle identification. The event start time in first order is given by the radio-frequency clock of the storage ring (for details see section 10.2.1) and the TOF system measures the time difference between event start time and the passage of a charged track through the layers of plastic scintillator. From the track length, the velocity of the particle can be calculated, and together with a momentum measurement in the drift chamber the particle mass can be determined. The TOF system also provides fast trigger signals of charged particles.

The barrel system is mounted on the outer shell of the drift chamber with an inner radius of 0.81 m and 0.86 m for the first and second layer. Each layer consists of 88 scintillator bars, each with a length of 2.3 m and a width of 50 mm. A polar angle region of $|\cos \theta| < 0.82$ is covered. Each bar has two photomultiplier tubes (PMT) attached on both ends.

The end cap system has 48 scintillator bars with trapezoidal shape that are arranged fan shaped in one layer. The inside end of the components is cut in a 45° angle to reflect the light to the outer end. Here a single PMT detects the scintillation light. The minimum flight path of particles detected by the end cap TOF is about 1.4 m. The end cap layer covers a polar angle region of $0.95 < |\cos \theta| < 0.85$.

9.2.1 Time resolution

The time resolution is influenced by many sources of uncertainty. The largest contribution comes from the ‘intrinsic’ time resolution which is determined by the rise time of the scintillation light and fluctuations of the photon arrival time. Another uncertainty comes from the time walk effect¹. Both sources of uncertainty depend only on the particle type and its momentum and are therefore intrinsic to the technology in use. These uncertainties are reduced by a factor of $1/\sqrt{2}$ by two independent measurements in both layers of the barrel part.

Other uncertainties come from the determination of the collision time (RF clock), the hit position along the z -direction, the finite bunch length of 1.5 cm and from the uncertainty of the momentum measurement.

¹ The time walk effect denotes the dependence of the threshold crossing time on the signal height

Table 9.1: Time resolution of the time-of-flight system for a single layer [47]. The total resolution of both layers in the barrel part is given in brackets.

Uncertainty	Barrel [ps]	End cap [ps]
Intrinsic	80 ~ 90	80
Bunch length	35	35
Collision time	~ 20	~20
Z position	25	50
Readout electronic	25	25
Momentum uncertainty	30	30
Time walk	10	10
Total time resolution	100 - 110 (80 - 90)	110

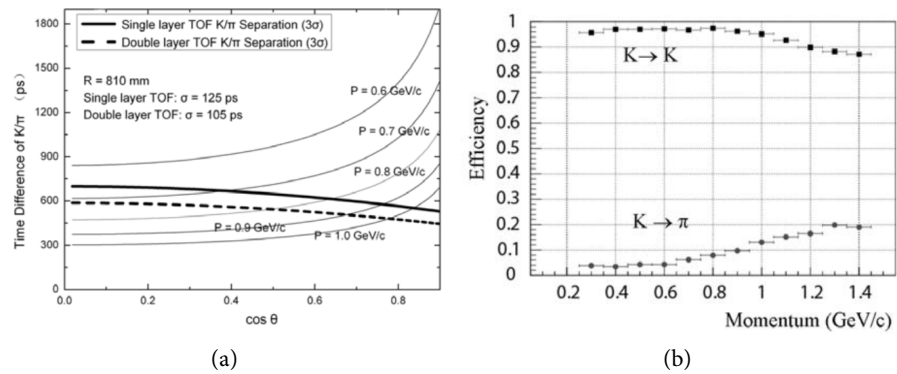


Figure 9.3: Time difference between kaon and pion as function of $\cos \theta$ (a) and the efficiency for kaon identification versus track momentum (b) [47].

An overview of different contributions to the time resolution is shown in table 9.1. The expected performance is shown in fig. 9.3 in terms of time difference between a kaon and pion track (a) and in terms of kaon identification efficiency (b).

Currently for the time resolution in the barrel part the expectations are outperformed by 89 ps and 67 ps [48] for one and two layers. In the end cap part the resolution is 131 ps which is below expectation. Therefore, a new system is under construction which replaces the plastic scintillator end caps by a system of multi-gap resistive plate chambers (MRPC) [48].

9.3 ELECTROMAGNETIC CALORIMETER

The electromagnetic calorimeter (EMC) surrounds the TOF detectors. It provides a accurate energy and position measurement of neutral showers in an energy range from 20 MeV up to the BEPCII maximum beam energy. Furthermore, a good electron-pion separation is provided. The calorimeter is built from

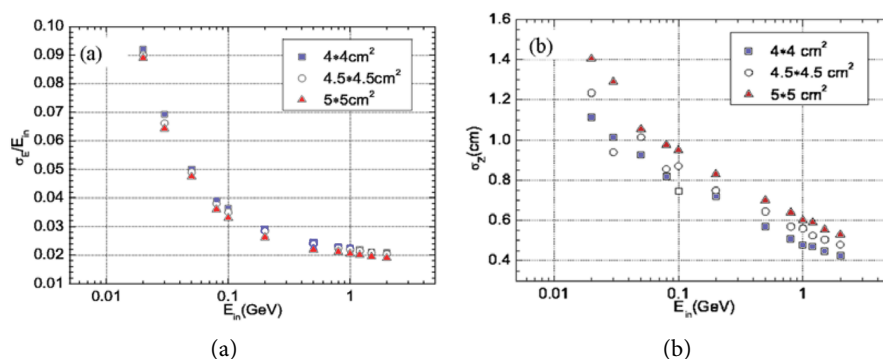


Figure 9.4: Monte-Carlo simulation for energy (a) and position resolution (b) for different crystal sizes as function for the photon energy [47].

thallium doped caesium iodide CsI(Tl) crystals which provide a high light yield and are therefore well suited for the detection of low energy photons. The whole detector consists of 6240 crystals that are arranged in 56 rings around the TOF system. Each crystal has a length of 28 cm which is equivalent to $15.1X_0$ and an area of 5.2×5.2 cm pointing to the interaction point. The crystals have a tilt of 1.5° and 1.5° - 3° in ϕ and $\cos \theta$ direction, respectively. This avoids that photons coming from the interaction point hit the transition region between crystals. The calorimeter covers an polar region of $\cos \theta < 0.83$ in the barrel and $0.84 < \cos \theta < 0.93$ in the end cap part. This corresponds to a coverage of 93 % of the full solid angle. The expected resolution of energy and position as function of the photon momentum is shown in fig. 9.4. An update on the current performance of the calorimeter can be found in [49].

9.4 MUON SYSTEM

The BESIII muon system (MUC) is integrated into the magnetic flux return. The technology of choice are resistive plate chambers (RPC) since the area that has to be covered is about 700 m^2 and RPC's provide an inexpensive and robust solution. The components of the gas mixture are argon (51 %), Tetrafluoroethane (41 %) and isobutane (8 %). Two layers of RPC's are combined into one super module of which 8 sections, with 9 layers of super modules each, surround the EMC in the barrel part in a octagonal shape. Due to space limitations only 8 layers are used in the end caps.

The main task of MUC is the identification of muons with a cut-off momentum as low as possible. The requirement on position resolution is modest because tracks in the muon system can later be matched to tracks measured in the drift chamber and to showers in the EMC. Using this matching condition low momentum muons can be identified down to 400 MeV. More details are provided in [47, 50].

DATA ANALYSIS AT BESIII

The BESIII off-line software environment is based on the GAUDI [51] framework. GAUDI was originally developed for the LHCb experiment and provides a generic framework for high energy physics experiments. In the BESIII software environment GAUDI provides basic features like data read-in/read-out and general interface classes for e. g. event generators.

10.1 SIMULATION

The event generation with the BESIII software framework is illustrated in fig. 10.1. Typically the e^+e^- collision is simulated by KKMC [53]. KKMC simulates the electro-weak production of fermion pairs in e^+e^- collision including initial-state radiation ($e^+e^- \rightarrow f\bar{f} + n\gamma$) which is calculated in QED up to the second order. The energy regime ranges from the τ lepton threshold up to 1 TeV, it has therefore a broad application also for the B factories. After the simulation of the production process the virtual photon can hadronized using the parton shower model implemented in PYTHIA, or the production of the resonance and its decay can be simulated. For the decay of a resonance usually BESEVTGEN [52] is used in a second step. BESEVTGEN is a fork of EVTGEN [54] which was originally developed for the BABAR and CLEO experiments. It provides precise decay models, which can easily be extended by the user. It is used for simulating a sequential decay chain starting from the production and decay of a (charmonium) resonance till the quasi-stable particles. The final state radiation (FSR) of the particles is then simulated using PHOTOS [55].

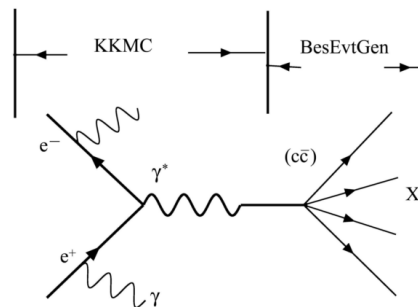


Figure 10.1: Event generation at BESIII [52].

The BESIII framework also provides the inclusive generators PYTHIA [56] and LUNDCHARM [57] and QED generators (e. g. BABAYAGA [58] or BHWIDE [59]). The latter ones are designed to simulate specific processes.

More information on the event generators used in BESIII can be found in [52].

10.2 RECONSTRUCTION

Particles transversing the detector trigger signals in different parts of the detector. After a calibration procedure charged tracks and electromagnetic showers can be reconstructed.

10.2.1 Event start time

The first step in the reconstruction procedure is the determination of the event start time. It is defined as the common time at the origin of all tracks in an event. Since the trigger rate is lower than the bunch crossing frequency the determination is not trivial, nevertheless the accurate determination is crucial for track reconstruction in the MDC. Using a fast reconstruction algorithm, tracks in the MDC are reconstructed and matched to hits in the TOF layers. Using a dE/dx measurement the particle type is estimated. The common event start time is then calculated from the time-of-flight measurement of all tracks in the event. The procedure is described in [60].

10.2.2 Charged tracks

Charged tracks are reconstructed from position measurements in the drift chamber. If we neglect the energy loss and multiple scattering of the particle when transversing the active volume of the drift chamber, its path in a magnetic field can be parameterized by a helix with 5 parameters:

d_0 signed distance in $x - y$ projection between pivot point and helix center

ϕ_0 azimuthal angle of \vec{d}_0

κ inverse of track momentum $\kappa \sim 1/p_t$

d_z signed distance in z projection between pivot point and helix center

λ slope of the track (tangent of the dip angle)

The helix is fixed in space by its pivot element \vec{x}_{pivot} . The physics parameters at the interaction point of a charged track are given by:

$$\vec{x} = \vec{x}_{\text{pivot}} + \begin{pmatrix} d_0 \cos \phi_0 \\ d_0 \sin \phi_0 \\ d_z \end{pmatrix} \quad \vec{p} = \begin{pmatrix} -\sin \phi_0 / \kappa \\ \cos \phi_0 / \kappa \\ \tan \phi_0 / \kappa \end{pmatrix}. \quad (10.1)$$

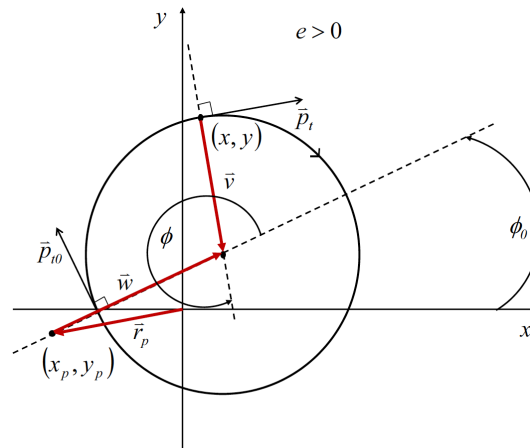


Figure 10.2: Illustration of helix parameterization for a negatively charged track with magnetic field along the negative z -direction [61].

A detailed description of the helix parameterization is given in [61]. BESIII has adopted the Belle helix parameterization.

The track finding algorithm starts by searching for straight track segments in the super layers. Using one of the segments as track seed, other segments are added successively. The best combination of segments is kept and fitted with the helix parametrization discussed above. Hits that were not part of a segment are added in a second step and the fit is repeated. When all tracks in a single event are reconstructed hits contributing to more than one track hypothesis are matched to one track. In that way artificial tracks are reduced efficiently.

10.2.3 Electromagnetic showers

The EMC measures the energy and position of photons and electrons. A photon transversing the calorimeter material converts to an electron-positron pair which in turn emits photons by bremsstrahlung. The shower can spread over several crystals of the detector. A cluster finding algorithm search for signals in neighboring crystals and afterwards the particle energy is calculated by the sum of energy deposited in each crystal. Usually a 3×3 or 9×9 matrix of crystals around the shower is used for the energy calculation to reduce the effects of detector noise. The particle position is determined by the weighted center of the cluster. A cluster can also be caused by two particles (e. g. $\pi^0 \rightarrow \gamma\gamma$). In that case the cluster has usually two crystals with peaking energy. Energy and position of both photons are then calculated by a reweighting procedure. More details are available in [62].

10.3 ANALYSIS

The analysis of events of course strongly depends on the channel under study, nevertheless in the following we want to discuss some general tools that are important for almost every analysis.

10.3.1 Kinematic fitting

The uncertainties on momentum and position measurements of tracks and showers can be reduced by applying additional constraints. A constraint can be a common vertex, four-momentum conservation or a requirement on the momentum direction. A Kalman Filter [63] is applied to optimize the track parameters given their measurement errors and a χ^2 value is calculated. Since the uncertainties on the track parameters are usually not perfectly estimated, the χ^2 is not a good quantity to calculate a probability for a certain hypothesis. Yet it can be used to rank different hypotheses. Within the BOSS framework these constraints are applied in separate steps.

10.3.2 Particle identification

An important task for most analysis is a good identification of the quasi-stable particles electron, muon, pion, kaon and proton. Depending on the particle type different signatures are observed in the different subdetectors. In the following we want to outline qualitatively how particles are identified.

Electrons have a small mass and they deposit typically all their energy in the calorimeter. The ratio energy over momentum is therefore close to one, while heavier particles are not completely stopped in the calorimeter. Muons deposit almost no energy in the calorimeter but are detected in several layers of the muon system. The track reconstructed from hits in the RPC's can be matched to the drift chamber track. This matching is worse for secondary muons (e.g. from $\pi \rightarrow \mu\nu_\mu$), which can be excluded in that way. Pions, kaons and protons can be identified using information from the energy loss in the drift chamber and from the time-of-flight system. The energy loss per length (dE/dx) depends on the particle momentum and its mass. The distribution of energy loss per path length versus momentum is shown in fig. 10.3(a). In the low momentum range particles can be well separated. With the measurement of the flight time, the momentum and the path length, the velocity can be calculated which differs for particles with the same momentum but different masses. An invariant mass spectrum for a typical momentum range calculated from momentum and velocity is shown in fig. 10.3(b).

Generally the total probability that a particle of certain type and momentum leaves a certain signature in the detector is a combination of information of all subdetectors and can be highly non-trivial in case that measurements are correlated and the probability distributions are unknown. But practically we have to combine only the TOF measurement with the energy loss in the drift chamber to separate pions, kaons and protons. We assume that correlations are small and calculate the probability for particle hypothesis H with momentum p and detector signature x as:

$$\mathcal{P}(x; p, H = \{\pi, K, p\}) = \text{Prob}(\chi_{dE/dx}^{2p,H}(x) + \chi_{TOF}^{2p,H}(x), 2). \quad (10.2)$$

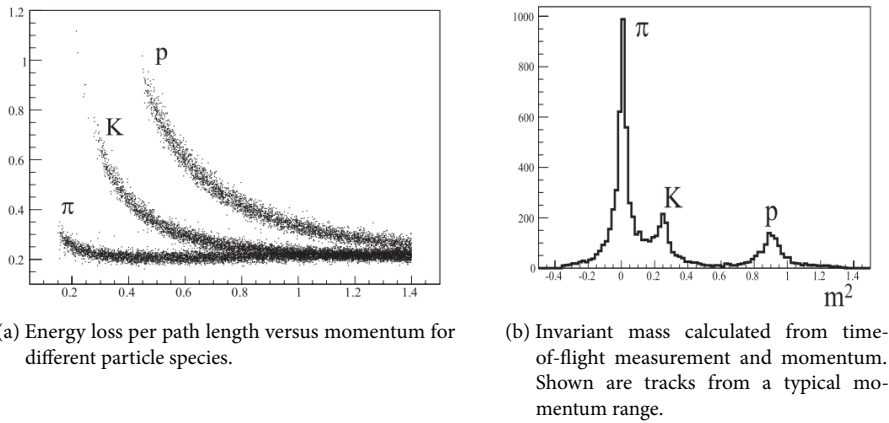


Figure 10.3: Particle identification based on TOF and MDC information [64].

χ_{TOF}^2 is the weighted sum of measurements in the first and second TOF layer and $\text{Prob}(\chi^2, \text{ndf})$ is the cumulative χ^2 distribution.

For a detailed description see [64].

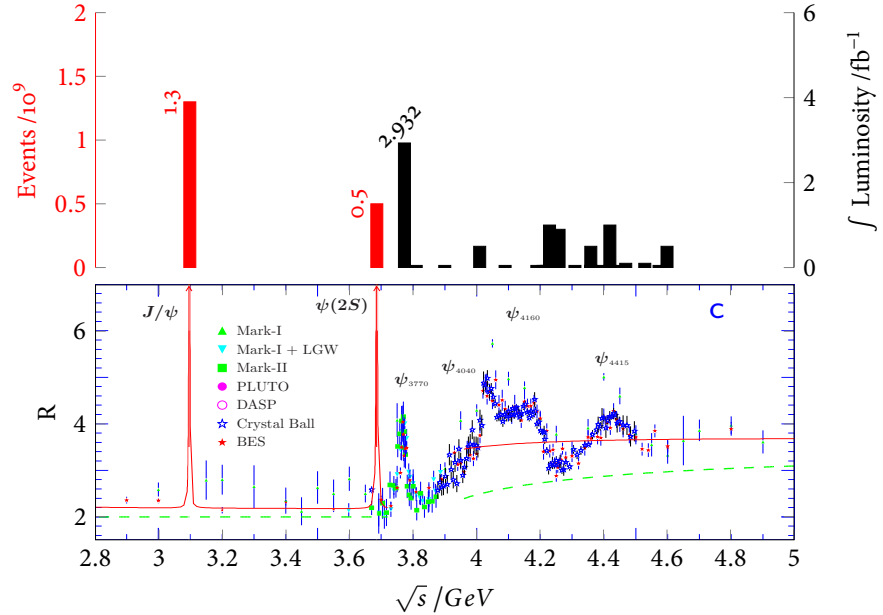
10.3.3 D tagging

D tagging refers to an analysis technique in special decay topologies which contain a pair of D mesons. These topologies arise at certain thresholds. The $\psi(3770)$ has a mass of $3.773 \text{ GeV}/c^2$ which is close to the $D^0 \bar{D}^0 / D^+ D^-$ threshold and the $\psi(3770)$ decays predominantly to those channels¹. The decay $\psi(3770) \rightarrow D\bar{D}$ is illustrated in fig. 3.2.

The $D\bar{D}$ pair is produced in a quantum entangled state and information on one of the mesons imposes constraints on the other meson. A so-called tagged analysis generically reconstructs one D meson D_{tag} in a clean channel with a high branching fraction and the second D is then reconstructed in the channel of interest. Depending on the tag mode the flavour of the signal decay or the CP quantum numbers are constrained and a flavour or CP eigenstate can be investigated. Since the available phase-space in the decay $\psi(3770) \rightarrow D\bar{D}$ is less than $44 \text{ GeV}/c^2$, the decay is fully reconstructed and the background is very low. The algorithm for the generic D reconstruction are called DTAGALG. The most important modes for the neutral D reconstruction are listed in table 10.1. The tag modes cover only a part of the D^0 branching fraction and therefore the tagging of a D^0 decay can reduce the statistics significantly. The tag information is diluted by doubly Cabbibo suppressed (DCS) decays of the D^0 and by D^0 mixing. DCS decays are typically suppressed by $\mathcal{O}(10^{-3})$ and D^0 mixing is slow. Nevertheless it can have an influence, as shown in chapter 6.

Table 10.1: D^0 flavour and CP tag modes with branching fractions [7].

Flavour tag		CP even	
$K^- \pi^+$	$(3.88 \pm 0.05) \%$	$K^+ K^-$ $(0.386 \pm 0.008) \%$	
$K^- \pi^+ \pi^0$	$(13.9 \pm 0.5) \%$	$\pi^+ \pi^-$ $(0.1402 \pm 0.0026) \%$	
$K^- \pi^+ \pi^0 \pi^0$	$(1.58 \pm 0.34) \%$	$K_S^0 \pi^0 \pi^0$ $(0.91 \pm 0.11) \%$	
$K^- \pi^+ \pi^+ \pi^-$	$(8.08 \pm 0.28) \%$	$\Sigma \mathcal{B}$ 1.4362 %	
$K^- \pi^+ \pi^+ \pi^- \pi^0$	$(4.2 \pm 0.4) \%$	CP odd	
$K^- \pi^+ \eta$	-	$K_S^0 \pi^0$ $(1.19 \pm 0.04) \%$	
$K^\mp e^\pm \nu_e$	$(3.55 \pm 0.05) \%$	$K_S^0 \omega$ $(1.11 \pm 0.06) \%$	
$K^\mp \mu^\pm \nu_\mu$	$(3.31 \pm 0.13) \%$	$K_S^0 \eta$ $(0.476 \pm 0.003) \%$	
$\Sigma \mathcal{B}$	38.50 %	$\Sigma \mathcal{B}$ 2.776 %	

Figure 10.4: BESIII data samples in the τ -charm region.Figure 10.5: R value in τ -charm region [7].

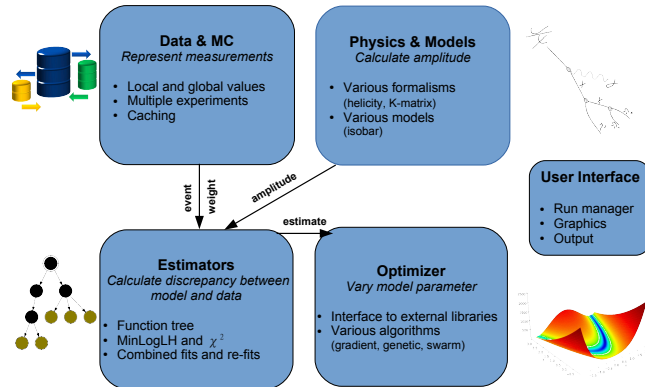


Figure 10.6: Overview over the modular structure of ComPWA [66].

10.4 DATA SAMPLES

The physics data taking started in 2009. Since that time data samples over the whole energy region were taken. The samples are illustrated in fig. 10.4. In fig. 10.5 the R value distribution in the charmonium region is shown to emphasize the close connection of the BESIII physics program to the charmonium region. Additionally to the data sample shown, scan data samples in the energy ranges from 2.05 GeV to 3.08 GeV and from 3.85 GeV to 4.56 GeV are available. An extensive overview over the BESIII physics program is given in [65].

10.5 PARTIAL WAVE ANALYSIS FRAMEWORK

The Dalitz plot analysis that is performed in the scope of this thesis uses the COMPWA framework² [66].

It was originally developed for the PANDA experiment and is not linked to BESIII. Yet is completely experiment independent and it offers a modularized design that allows the implementation of different types of physics models, estimators and optimizers. An overview of the COMPWA framework is shown in fig. 10.6. The amplitude model that is currently implemented is described in part ii and details on the likelihood and efficiency correction are given in part iv. The optimizer module currently supports minimization by MINUIT2 [67] and GENEVA³ [68]

Within the scope of this thesis major parts of the framework were extended. In particular, the resonance model and the likelihood estimation were modified and additional functionality was added. For the efficiency correction a

¹ Another threshold is around 4.2 GeV where the production of $D^0 D_0^{*+} (2400)^0$ starts.

² The COMPWA repository is hosted on <https://github.com/ComPWA>. The revision that is used is [commit 89baf58e](https://github.com/ComPWA/commit/89baf58e).

³ GENEVA provides an evolutionary algorithm to find the minimum in a high dimensional parameter space.

binned and an unbinned method were implemented. Further work was done in improving printing and plotting capabilities of the framework. Since this is one of the first analyses done with this framework a significant amount of time was spent on general validation tasks.

Part IV

ANALYSIS OF THE DECAY $D^0 \rightarrow K_s^0 K^+ K^-$

We present the analysis of the decay $D^0 \rightarrow K_s^0 K^+ K^-$ using 2931.8 pb⁻¹ of data taken at $\sqrt{s} = 3.773$ GeV with the BESIII detector. We perform an analysis of the $K_s^0 K^+ K^-$ Dalitz plot and measure the branching fraction.

The Dalitz plot analysis is performed using a sample of 1856 ± 45 flavour tagged signal events with a purity of 96.37 %. We find that the Dalitz plot is well described by a set of four resonances: $a_0(980)^0$, $a_0(980)^+$, $\phi(1020)$ and $a_2(1320)^-$. We determine their magnitudes, phases and fit fractions. Furthermore we measure the $a_0(980)$ coupling $g_{K\bar{K}} = (2.88 \pm 0.25 \text{ (stat.)} \pm 0.56 \text{ (sys.)}) \text{ GeV}$. The branching fraction is measured using 11 384 ± 115 untagged signal decays and we obtain a value of $(4.45 \pm 0.05 \text{ (stat.)} \pm 0.18 \text{ (sys.)}) \times 10^{-3}$. The measurement yields a relative precision of 4.21 % which improves the current best measurement significantly. Both measurements are limited by their systematic uncertainty.

EVENT RECONSTRUCTION AND SELECTION

In the following we describe the event reconstruction and selection of the decay $D^0 \rightarrow K_S^0 K^+ K^-$. We introduced the special decay topology of $\psi(3770)$ decays in chapter 3 and fig. 3.2. Since the $\psi(3770)$ decays predominantly to a pair of charged or neutral D mesons we have the choice to reconstruct both D mesons or to reconstruct only the signal decay. We refer to this as tagged and untagged analysis, respectively. In both cases the reconstruction procedure of the signal decay is identical. A flavour tagged analysis is necessary for the Dalitz plot analysis since the flavour of the D^0 cannot be determined from the $K_S^0 K^+ K^-$ final state. The disadvantage is a reduction of statistics by a factor of about 6.

In the $\psi(3770) \rightarrow D\bar{D}$ decay topology the energy of each D mesons is half the center-of-mass energy E_{cms} . This makes it convenient to introduce two kinematic variables. The beam-constrained mass m_{BC} is given by:

$$m_{BC}^2 c^4 = (E_{cms}/2)^2 - |\vec{p}_D|^2 c^2 \quad (11.1)$$

The reconstructed D^0 momentum \vec{p}_D is calculated from the momenta of its final state particles. The center-of-mass energy E_{cms} is calibrated on a per-run basis. The D^0 beam-constrained mass has a better resolution compared to the D^0 mass. The second variable is the energy difference between the measured D^0 energy and the beam energy:

$$\Delta E = E_{cms}/2 - E_D. \quad (11.2)$$

The energy is measured using the momenta of the final state particles and their particle hypothesis. ΔE is expected to be centered around zero.

11.1 MONTE-CARLO SIMULATION

In the following we describe the Monte-Carlo simulation. It is used to develop the selection requirements, to calculate the reconstruction efficiency for the branching fraction measurement (chapter 13) and to normalize the likelihood in the Dalitz plot analysis (chapter 12). Technical details about the simulation are given in section 10.1.

The BESIII collaboration provides a series of samples for different reactions. A list of all samples that are used throughout this work is shown in table 11.1. In the following we refer to the mixture of all those samples as Monte-Carlo sample. Each sample is scaled to the luminosity of the data sample. The full

data set of 2.932 fb^{-1} was collect during the 2010 and 2011 data taking period in which 0.927 fb^{-1} and 1.990 fb^{-1} were collected, respectively. For the branching fraction measurement we need to determine the signal reconstruction efficiency using Monte-Carlo simulation. The substructure of the decay can influence the total efficiency. We therefore use the amplitude description of the Dalitz plot from chapter 12 to generate an accurate signal Monte-Carlo sample. Technically we apply a hit-and-miss procedure ¹ to the large sample of events which are uniformly distributed over the phase-space. Signal events from the $D^0\bar{D}^0$ Monte-Carlo sample are then replaced by events from the new signal sample.

Table 11.1: Data and Monte-Carlo samples at $\sqrt{s} = 3.770 \text{ GeV}$. Luminosities of the Monte-Carlo samples are given in multiples of the luminosity of the data sample.

Reaction $e^+e^- \rightarrow X$	Luminosity (fb^{-1})	
	2010	2011
Data [69]	927.67 ± 9.28	1989.27 ± 19.89
$\psi(3770) \rightarrow D^0\bar{D}^0$	$21.8\times$	$21.8\times$
$\psi(3770) \rightarrow D^+D^-$	$10.9\times$	$10.8\times$
$\psi(3770) \not\rightarrow D\bar{D}$	$7.8\times$	$7.3\times$
$q\bar{q}$ (KKMC)	$7.8\times$	$7.3\times$
$\psi(2S)\gamma$	$10.8\times$	$10.1\times$
$J/\psi\gamma$	$10.8\times$	$10.1\times$
$\tau^+\tau^-$	$10.8\times$	$10.1\times$
$\mu^+\mu^-$	$5.0\times$	$5.0\times$
e^+e^-	$0.2\times$	$0.2\times$
$D^0\bar{D}^0 \rightarrow (\text{tag})(K_s^0K^+K^-)$ isotropic	5×10^7 events	
$D^0\bar{D}^0 \rightarrow (\text{tag})(K_s^0K^+K^-)$ resonant structure	3×10^7 events	

The simulated branching fraction for $D^0 \rightarrow K_s^0 K^+ K^-$ is 3.079×10^{-3} and therefore significantly lower than quoted by the PDG [7]. This originates from the problem that the branching fractions quoted by the PDG does not sum up to one. During generation one tries to reproduces the decay of channels with a high branching fraction as well as possible but channels with small branching fraction are often not reproduced very well. We correct the signal events for the inaccurate branching fraction by assigning corresponding weights to each event.

¹ A sample which is distributed according to a real-valued function can be generated via the so-called hit-and-miss procedure. For each data point in a uniformly distributed sample, a random number between zero and the function maximum is generated. If this number is smaller than the function value the event is accepted and rejected otherwise.

The distributions for some kinematic variables from the untagged sample are shown in fig. 11.1. No requirements are set on the beam-constrained D^0 mass and the K_s^0 mass. There are discrepancies between data and simulation, e. g. in the K_s^0 transversal momentum p_T . This most likely comes from a wrong normalization of the $q\bar{q}$ background sample. We discuss the background in section 11.5 and its systematic effect on the branching fraction measurement in chapter 13.

In the following we describe the selection of the final state particles, the tag candidates and the signal candidates. Note that the variables that are correlated with the Dalitz plot variables cannot be used for selection since it would lead to a non-uniform selection efficiency over the Dalitz plot. This is particularly true for all kinematic variables of the $K_s^0 K^+ K^-$ final state.

11.2 RECONSTRUCTION AND SELECTION OF THE FINAL STATE PARTICLES

The selection requirements of the final state particles and the tag candidate are consensus in the collaboration and we do not optimize these for the decay $D^0 \rightarrow K_s^0 K^+ K^-$. The detector is described in chapter 9 and especially fig. 9.1 is useful for understanding the selection criteria.

11.2.1 Charged kaons and pions

The momenta of charged tracks are calculated from the curvature of their tracks in the magnetic fields (see section 10.2.2 for details). From the signals in the drift chamber the helix parameters are determined using a Kalman filter and we require that the minimization succeeds. We select tracks originating from the interaction point by requiring that the point of closest approach of the helix and the interaction point are separated by less than 1 cm in radial direction and less than 10 cm in beam direction (z -direction). Furthermore we require that all tracks have a polar angle $\cos \theta$ smaller than 0.93, see fig. 11.1(g). This corresponds to the angular coverage of the drift chamber and the calorimeter. The interaction point can slightly vary from run to run and we use an average point per run.

The particle species is determined from the energy-loss dE/dx in the drift chamber and information from the time-of-flight system. For each subsystem and each particle species a $\chi^2(H)$ variable is calculated (see section 10.3.2) and then combined:

$$\chi^2(H) = \chi_{dE/dx}^2(H) + \chi_{TOF}^2(H). \quad (11.3)$$

Using the corresponding number degrees of freedom a probability P_H for each particle hypothesis H can be calculated and we require that all kaon and pion candidates satisfy $P_K \geq P_\pi$ and $P_\pi \geq P_K$, respectively.

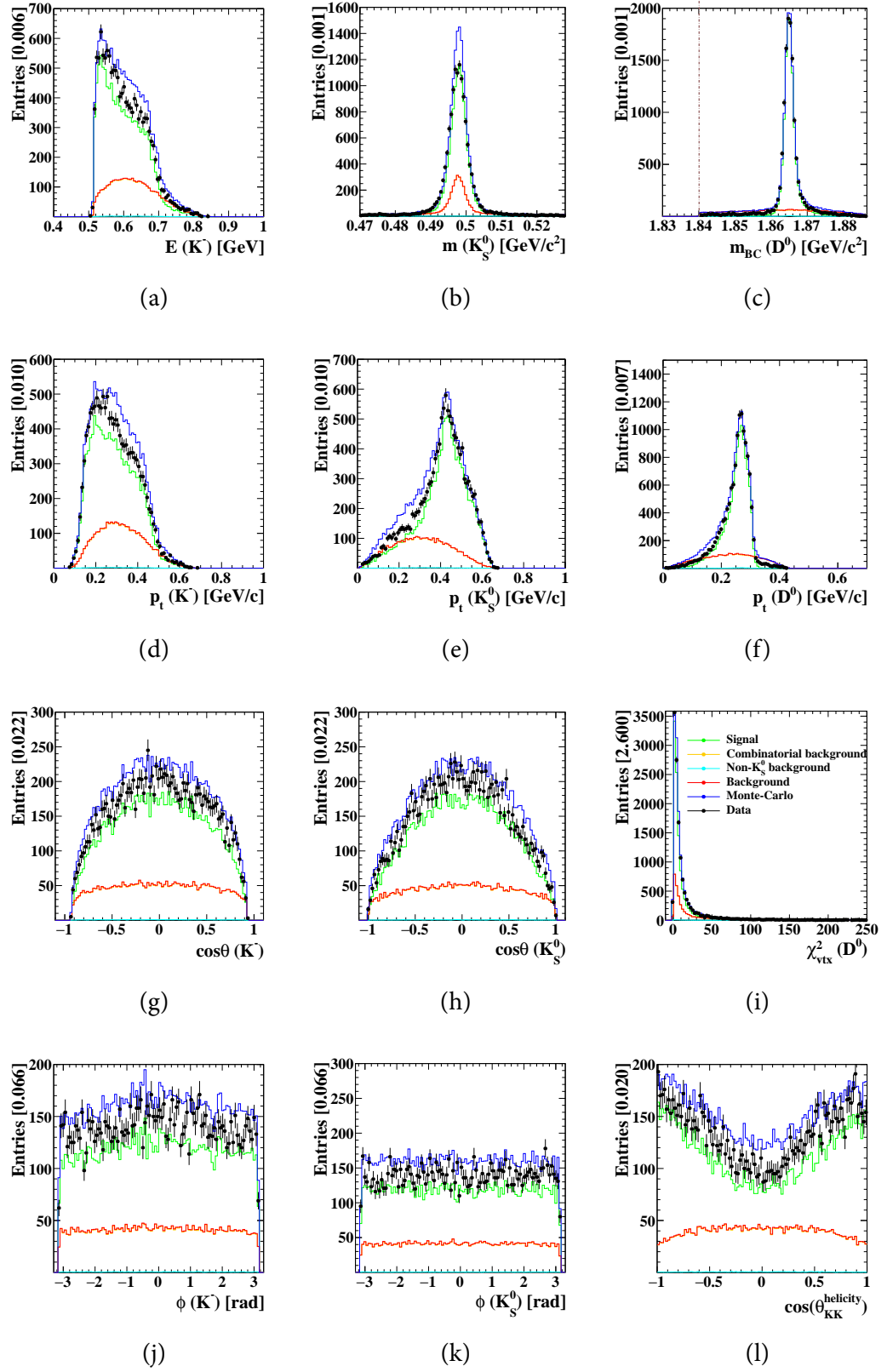


Figure 11.1: Untagged data (black) and Monte-Carlo (blue) samples. The Monte-Carlo sample is split into signal (green) and background (red). No requirements are imposed on m_{BC} and m_{KS} . Discrepancies between data and simulation are due to an improper scaling of the Monte-Carlo background sample.

11.2.2 Photons

The showers measured in the electromagnetic calorimeter are required to have a minimum shower energy of 25 MeV in the barrel part and 50 MeV in the end cap parts. Barrel and end cap are defined by a polar angle of $|\cos \theta| \geq 0.8$ and $0.84 \geq |\cos \theta| \geq 0.92$, respectively. The transition region between barrel and end cap is excluded. The minimum energy requirement is different since the barrel part has a better energy resolution. In case that more than one charged track was found in an event the time difference between arrival time in the calorimeter and the event start time needs to be between 0 ns and 700 ns.

11.2.3 π^0 and η candidates

Neutral pions and η are reconstructed from pairs of photons. Photons meet the requirements described before and we reject candidates with both photons detected in the end cap part due to poor resolution. π^0 candidates with invariant mass from $0.098 \text{ GeV}/c^2$ to $0.165 \text{ GeV}/c^2$ are selected. For η candidates the range is from $0.4 \text{ GeV}/c^2$ to $0.7 \text{ GeV}/c^2$. A kinematic fit with the nominal π^0 or η mass as constraint is performed and we require that the fit succeeds. The momenta obtained from the fit are used for further analysis.

11.2.4 K_s^0 candidates

The K_s^0 candidates are reconstructed from a pair of oppositely charged pions. A typical flight distance of K_s^0 candidates from D decays at $\sqrt{s} = 3.773 \text{ GeV}$ is about 2 mm. The pions therefore do not have the requirement to originate from the interaction point. Nevertheless the point of closest approach is required to be within 20 cm along the beam line. The pion pair is required to pass a kinematic fit with a common vertex as constraint and the χ^2 needs to be less than 100. The resulting momenta are used for the calculation of the K_s^0 invariant mass and for further analysis. The K_s^0 mass window is chosen to be from $0.487 \text{ GeV}/c^2$ to $0.511 \text{ GeV}/c^2$. The K_s^0 candidates for the signal decay have a relaxed mass window from $0.47 \text{ GeV}/c^2$ to $0.528 \text{ GeV}/c^2$. Since the K_s^0 mass spectrum is used to determine the signal yield, a larger sideband region is needed. Furthermore, on K_s^0 candidates of the signal decay another kinematic fit is applied with the requirement that the K_s^0 momentum points back to the interaction point. From this fit result, the K_s^0 flight distance and its uncertainty are obtained. We require a flight distance in units of its uncertainty of at least 0 and 2 for the tagged and untagged sample, respectively. The distribution is shown in fig. 11.2(a). Since the tagged sample has poor statistics we use a relaxed requirement.

11.3 TAG CANDIDATES

For a so-called tagged analysis both D mesons are reconstructed. See section 10.3.3 for technical details. The tag decay is generically reconstructed in

multiple channels. In case that the flavour of the signal decay is supposed to be tagged, the tag channel must provide this information. A list of flavour tag channels is given in table 10.1. In this analysis only hadronic decay channels are used. Additionally it is possible to use semi-leptonic decay channels but a higher background level is expected and we pass on this option. In each event we search for a tag decay and the signal decay $D^0 \rightarrow K_s^0 K^+ K^-$. If there are multiple candidates per event, the combination is chosen which has an average beam-constrained mass closest to the nominal D^0 mass.

$$\overline{m_{BC}} = \frac{m_{BC}^{\text{tag}} + m_{BC}^{\text{signal}}}{2} \quad (11.4)$$

We search for a tag-signal combination for each tag mode separately and so is possible that one event is counted multiple times. In this case, we select randomly one of the candidate pairs.

Bhabha events ($e^+ e^- \rightarrow e^+ e^-$) and cosmic radiation can mimic two-body D decays. For the tag channel $K^- \pi^+$ we veto these events. We reject events if one of the following requirements is fulfilled:

1. The event has only two charged tracks.
2. The flight time difference between the tracks is above a certain threshold.
3. Both tracks are identified as electrons.
4. Both tracks have a signal in the muon chambers.

For all D^0 tag candidates we require that the beam-constrained mass m_{BC} is between $1.86 \text{ GeV}/c^2$ and $1.87 \text{ GeV}/c^2$.

11.4 SIGNAL CANDIDATES

The selection of the final state particles $K_s^0 K^+ K^-$ was described previously. We combine them to a D^0 candidate and apply a kinematic fit to the $K_s^0 K^+ K^-$ combination with the nominal D^0 mass as constraint and require a χ^2 smaller than 20. The distribution is shown in fig. 11.2(b). The fitted four-momenta of the daughters are used to calculate the invariant masses for the Dalitz plot analysis. Other variables use the original four-momenta. In a separate step we perform a kinematic fit with a common vertex as constraint and require that the fit succeeds. The updated four-momenta are used for further analysis.

In case of a tagged analysis the best candidate combination is chosen, as mentioned before, by an average m_{BC} closest to the nominal D^0 mass. If only the signal decay is reconstructed (untagged analysis) we choose the candidate with minimum $\Delta E = E_D - E_{\text{beam}}$.

The total selection is summarized in table 11.3. Untagged events pass our selection with a signal efficiency of 64.39 % and a background rejection rate of 99.63 %. This leads to a purity of the untagged data sample of 93.5 %. Those numbers are obtained from a two-dimensional fit the m_{BC} and m_{KS} . Events are required to be within an 8σ signal region (see section 11.4.1). A detailed

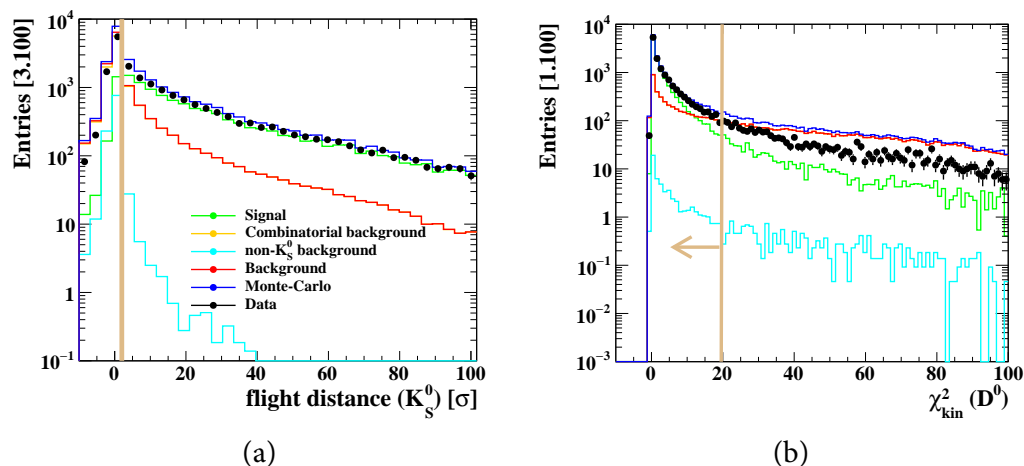


Figure 11.2: Non-standard selection variables. The distributions shown are the untagged sample with the full selection applied except the requirement on the variable that is shown. The selection value is indicated.

list of signal and background efficiencies for untagged data and Monte-Carlo samples are given in table 11.2. For flavour tagged events the purity raises to 96.37 %.

The distribution of m_{BC} of the tag candidate versus m_{BC} of the signal candidate after selection is shown in fig. 11.3(a).

11.4.1 Signal region

The tagged analysis requires a signal region. We define it by a box with the side length $n \times \sigma_{m_{BC}}$ along m_{BC} and $n \times \sigma_{m_{KS}}$ along m_{KS} . Where $\sigma_{m_{BC}}$ and $\sigma_{m_{KS}}$ are the resolutions of the central signal peak. The signal and background yields on data are obtained by a two-dimension fit as described in section 11.6. The fit is performed on the full data set without requirements on m_{BC} and m_{KS} . The yields for a certain signal region size are calculated by integrating the fit model in the region of interest. For different sizes of the signal region yields and purities are listed in table 12.2. The maximum significance for the tagged sample is obtained with a signal region size of $8 \times \sigma$. We choose this value for the further analysis. Background studies for the Dalitz plot analysis require sideband samples in which we include events outside a 10σ region.

11.4.2 Multivariate discrimination

We do a cross-check of our cut-based selection by comparing it to some multivariate discrimination methods provided by the TMVA package [67]. The discrimination variables used are:

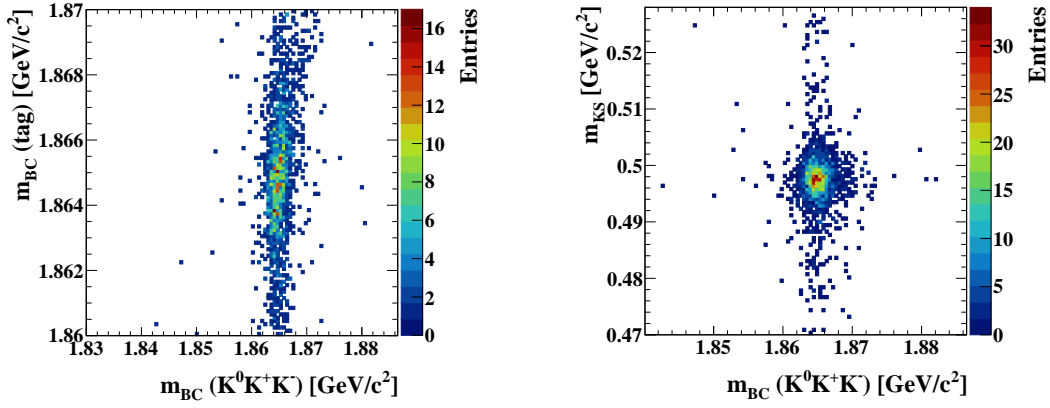
- D^0 : energy (ΔE), momentum (P , P_t) and χ^2 of kinematic fits χ^2_{vtx} , χ^2_{mass} , $\chi^2_{\text{mass (incl. } K_S^0)}$.

Table 11.2: Yields and rejection efficiencies for the untagged Monte-Carlo sample. The samples are scaled to the luminosity of data. The signal region is explained in section 11.4.1.

Signal	full region		8σ signal region	
	yield	rejection[%]	yield	rejection[%]
Data	13 295 \pm 115		12 162 \pm 110	
Simulation	15 244 \pm 35		12 664 \pm 31	
Signal	11 300 \pm 28	31.07	10 990 \pm 27	32.96
Background	3944 \pm 22	99.63	1675 \pm 14	99.84
Purity [%]	74.13		86.78	
non- K_S^0	54 \pm 2	98.37	28 \pm 1	99.15
Combinatorial	3890 \pm 22	99.63	1646 \pm 14	99.84
$\psi(3770) \rightarrow D^0\bar{D}^0$	232 \pm 3	99.90	97 \pm 2	99.96
$\psi(3770) \rightarrow D^+D^-$	352 \pm 6	99.77	150 \pm 4	99.90
$\psi(3770) \rightarrow \text{non-DD}$	95 \pm 3	99.50	43 \pm 3	99.77
$q\bar{q}$	2611 \pm 19	99.41	1105 \pm 12	99.75
$\psi(2S)\gamma$	584 \pm 8	99.67	251 \pm 5	99.86
$J/\psi \gamma$	71 \pm 3	99.73	29 \pm 2	99.89
$\tau\tau$	0		0	
$\mu\mu$	0		0	
e^+e^-	0		0	

Table 11.3: Overview of selection requirements.

$K_S^0 \rightarrow \pi^+\pi^-$		K^\pm	
$\pi^\pm V_z$	< 20 cm	V_z	< 10 cm
$\pi^\pm \cos(\Theta) $	< 0.93	V_r	< 1 cm
vertex χ^2	< 100	$ \cos(\Theta) $	< 0.93
flight distance [σ]	> 2 (untagged) > 0 (tagged)	identified by SIMPLEPIDSvc	
D^0_{signal}		D^0_{tag}	
kinematic fit	< 20	1.86 GeV/c ² < m_{BC} < 1.87 GeV/c ²	
χ^2_{mass}		Veto l^+l^- for $D^0 \rightarrow K^+\pi^-$	



(a) Beam-constrained mass of the D^0 tag candidate versus the signal candidate.

(b) K_S^0 mass versus beam-constrained mass of the signal candidate. Projections are shown fig. B.1.

Figure 11.3: Flavour tagged data sample after selection.

- K_S^0 : χ^2 of kinematic fits (χ_{vtx}^2 , $\chi_{\text{secondaryVtx}}^2$) and flight distance.
- K^\pm : probabilities from particle identification.

Many kinematic variables cannot be used for selection because they are correlated to the Dalitz plot variables. The performance in terms of background suppression versus signal efficiency is shown in fig. 11.4. Compared with the corresponding values of our ‘manual’ selection, we cannot see an advantage in using one of these methods.

11.5 BACKGROUND

The background that passes our selection can be categorized according to its distribution in the m_{BC} versus m_{KS} plane which is shown in fig. 11.3(b):

- **Non- K_S^0 background:** The final state of the signal decay is $K_S^0 K^+ K^- \rightarrow \pi^+ \pi^- K^+ K^-$. Events that do not contain the intermediate decay of a K_S^0 show up as a peak in m_{BC} and a flat distribution in m_{KS} . This results in a horizontal band.
- **Combinatorial background:** Events which do not contain the correct final state. These events come from $q\bar{q}$ production and from partly reconstructed D decays. The m_{BC} distribution has a phase-space component and a wide peak component. The $\pi^+ \pi^-$ pair can originate from a K_S^0 decay. In this case the events show up as a vertical band in m_{KS} otherwise they are equally distributed.

Since the signal is peaking in the center of the m_{BC} versus m_{KS} plane, the signal and both background components can be nicely distinguished on data by a fitting procedure. This is used for the determination of the untagged signal

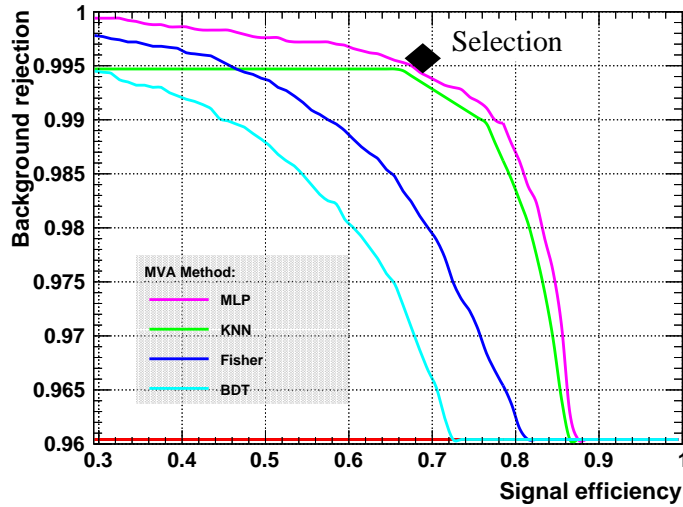


Figure 11.4: Background rejection rate versus selection efficiency. The performance of some multivariate discrimination methods is compared to our selection.

yield for the branching fraction measurement and the determination of the signal purity of the tagged sample for the Dalitz plot analysis. The projections of Monte-Carlo samples for signal, combinatorial and non- K_s^0 background are shown 11.5.

11.6 SIGNAL AND BACKGROUND MODELS

We have to discriminate our signal against two classes of background. Therefore, we describe signal, non- K_s^0 background and combinatorial background by probability-density functions (PDF) in m_{KS} and m_{BC} . The models for signal and background share the same description for the K_s^0 and D^0 mass peaks and therefore a simultaneous fit is appropriate to reduce the number of free parameters. The two-dimensional model is constructed as a product of the m_{BC} and m_{KS} components.

The **signal** peak in m_{KS} and m_{BC} is modeled using a modified Crystal-Ball function, as defined in eq. (B.2), with power-law tails on the left and on the right side.

The **combinatorial background** has a m_{BC} distribution which is well modeled by an ARGUS phase-space shape [70] and a wide Gaussian. The m_{KS} distribution has a peak with the same shape as the signal and a flat contribution which is described by a polynomial of first order.

The **non- K_s^0 background** shares the m_{BC} model with the signal and the m_{KS} mass is described by a polynomial of first order. We see from fig. 11.5 that the K_s^0 mass distribution of the non- K_s^0 background contains a peak despite the fact that there was no K_s^0 in the signal decay. Those candidates are reconstructed using a K_s^0 decay from the tag side. The peak vanishes for the tagged analysis. We add a K_s^0 peak and an ARGUS phase-space shape to the description of

m_{KS} and m_{BC} , respectively. Both components share their parameters with the combinatorial background shape.

A detailed description of the model can be found in appendix B.1. We fit the PDF simultaneously to three samples representing signal and background components. Projections of the samples and the fit functions are shown in fig. 11.5. All final shape parameter are listed in table B.7. We list only the result from the untagged sample.

The yields for signal and background are then determined by the combined model:

$$\begin{aligned}
 PDF(m_{BC}, m_{KS}) &= N_{\text{sig}} \times S(m_{BC}, m_{KS}) \\
 &+ N_{\text{comb}} B_{\text{comb}}(m_{BC}, m_{KS}) \\
 &+ N_{\text{non-}K_S^0} B_{\text{non-}K_S^0}(m_{BC}, m_{KS}). \quad (11.5)
 \end{aligned}$$

Using this model, an extended maximum-likelihood fit to data is performed.

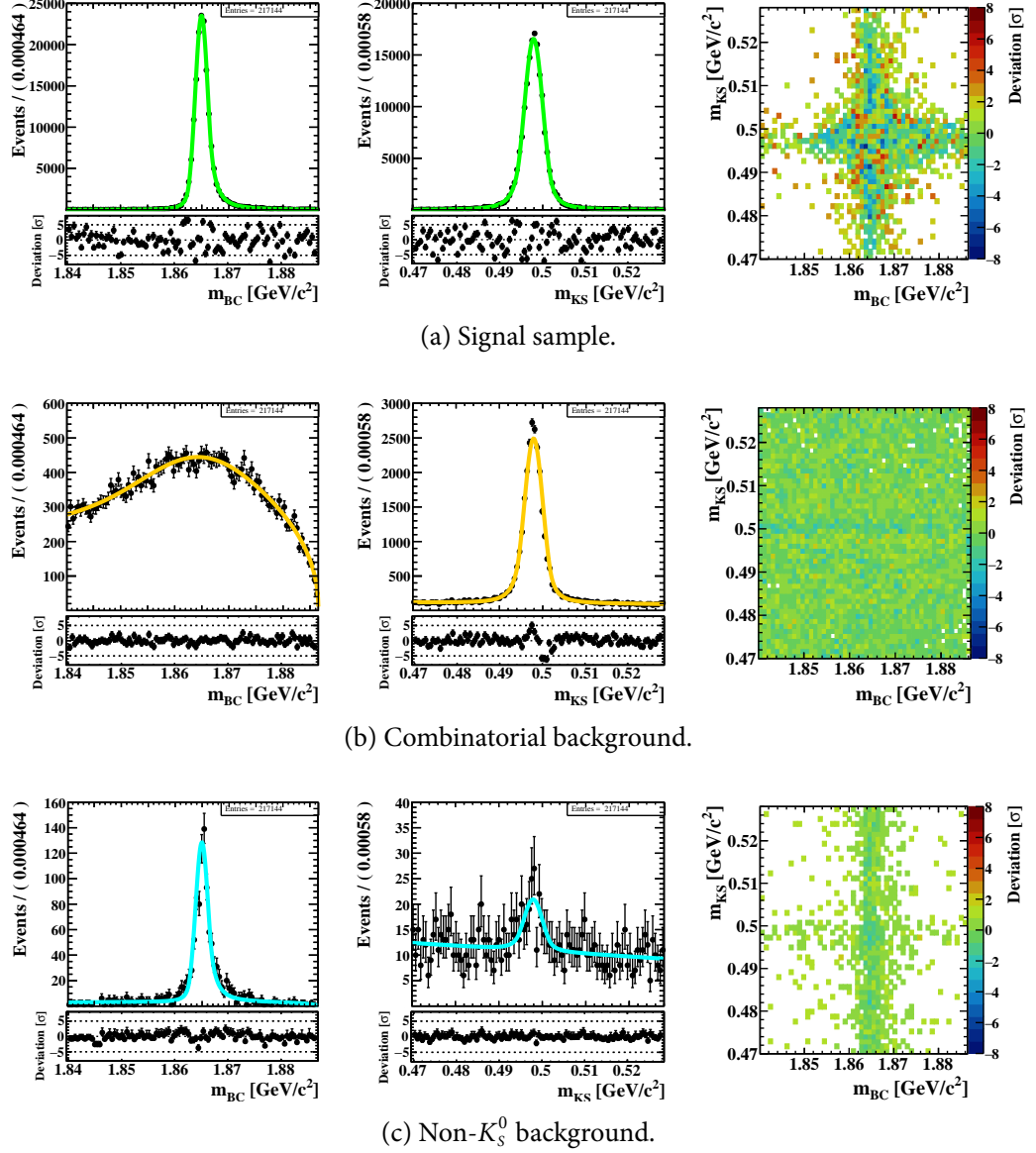


Figure 11.5: Dedicated samples for signal and background. The model is determined by a simultaneous fit to all three samples. The deviation between model and sample is shown in units of its uncertainty in the last column.

12

DALITZ PLOT ANALYSIS

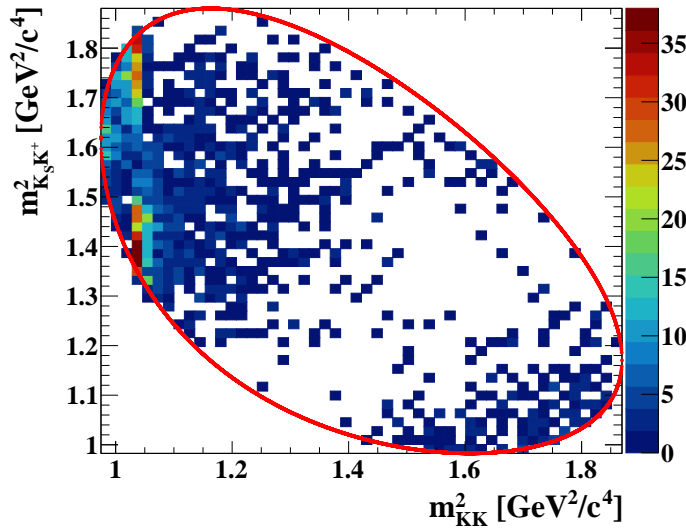


Figure 12.1: Binned Dalitz plot of the decay $D^0 \rightarrow K_s^0 K^+ K^-$ from 2931.8 pb^{-1} of $e^+ e^-$ collisions at $\sqrt{s} = 3.773 \text{ GeV}$. After reconstruction and selection a sample with 1872 ± 46 signal events is used for further analysis. The phase-space boundary is indicated in **red**.

The Dalitz plot for $D^0 \rightarrow K_s^0 K^+ K^-$ after reconstruction and selection is shown in fig. 12.1 and its projections in fig. 12.10. The distribution is dominated by the $\phi(1020)$ and the $a_0(980)^0$ resonances in the $K^+ K^-$ channel. Furthermore the $a_0(980)^+$ is visible in the $K_s^0 K^+$ channel. From the distribution along the $K_s^0 K^+$ invariant mass the vector particle nature of the $\phi(1020)$ can be observed.

The scope of this thesis is an analysis of the $K_s^0 K^+ K^-$ Dalitz plot and the determination of the partial branching fractions of the decay substructure. The Dalitz amplitude model is then used in the branching fraction measurement (chapter 13) as input to the simulation in order to determine the signal reconstruction efficiency.

The Dalitz amplitude parametrization is discussed in general in part ii and more specific in chapter 7. Details about the software environment are given in section 10.5 and the reconstruction and selection procedure was described in the previous chapter (chapter 11).

Table 12.2: Signal and background yields on data for different sizes of the rectangular signal region in m_{BC} and m_{KS} . The peak width in m_{BC} or m_{KS} is denoted by σ . We select signal region with 8σ side length.

Size of signal region $n \times \sigma$	Signal S	Background B	Purity S/(S+B)	Significance $S/\sqrt{S+B}$
1	701 ± 21	6.2 ± 1.9	0.991	26.68
2	1440 ± 36	17 ± 5	0.987	37.77
3	1672 ± 41	27 ± 9	0.983	40.57
4	1761 ± 43	36 ± 12	0.980	41.55
5	1805 ± 44	45 ± 14	0.976	41.97
6	1830 ± 45	54 ± 17	0.971	42.17
7	1845 ± 45	62 ± 19	0.967	42.26
8	1856 ± 45	70 ± 21	0.964	42.29
9	1863 ± 46	78 ± 23	0.960	42.29
10	1868 ± 46	85 ± 23	0.956	42.27

In the following we discuss the determination of the signal fraction in section 12.1 and the background amplitude model in section 12.2. The likelihood function is explained in section 12.3 and the efficiency correction in section 12.4. In section 12.5 we introduce the goodness-of-fit procedure. An overview of resonances that can appear as intermediate states is given in section 12.6 and the strategy that we use to select a proper set of resonances is explained in section 12.7. Systematic uncertainties are studied in section 12.8 and the results are finally presented and discussed in section 12.9.

In the following the free parameters of the Dalitz amplitude model are denoted with β and the Dalitz variables with ξ . These can be either two invariant masses, as used in fig. 12.1 or an invariant mass and the corresponding helicity angle (see fig. 4.12). In the first case we use m_{KK}^2 and $m_{K^0K^+}^2$ and in the latter case m_{KK}^2 and Θ_{KK} . The Dalitz amplitude model is denoted by $\mathcal{M}(\beta, \xi)$ and the amplitude of the resonances that occur as intermediate states by A_i .

12.1 SIGNAL PURITY

The reconstruction and selection procedure is described in detail in chapter 11. For the Dalitz plot analysis we define a signal region in the D^0 beam-constraint mass m_{BC} and in the K_s^0 mass m_{KS} (see section 11.4.1). The expected signal and background yields for different sizes of the signal region are listed in table 12.2. We a signal region with 8σ side length in m_{BC} and m_{KS} since it leads to the highest signal significance.

We determine the signal and background yields on data using models for signal and background as described in section 11.6. The fit is performed without a signal region and after the minimization we integrate the signal and back-

Table 12.1: Yields on data for different tag channels.

Flavour tag	Yield
$K^- \pi^+$	361 ± 19
$K^- \pi^+ \pi^0$	702 ± 26
$K^- \pi^+ \pi^0 \pi^0$	178 ± 13
$K^- \pi^+ \pi^+ \pi^-$	517 ± 23
$K^- \pi^+ \pi^+ \pi^- \pi^0$	114 ± 11
$K^- \pi^+ \eta$	63 ± 8
Total yield	1935 ± 44

Table 12.3: Signal and background yields for the data and Monte-Carlo samples within a 8σ signal region. The K_S^0 mass and width are left free in the fit. The comparison with the simulated true values shows that the correct result can be reproduced.

Parameter	Data	Simulation		
		Fit	True	Δ [σ]
Signal	1856 ± 45	1672 ± 43	1645.3	0.62
Combinatorial background	20 ± 20	49 ± 12	50.5	0.13
non- K_S^0 background	49.8 ± 6.8	32.2 ± 8.7	37.7	0.63
K_S^0 mass [MeV/ c^2]	497.58 ± 0.06	497.88 ± 0.06		
K_S^0 width [MeV]	2.39 ± 0.06	2.08 ± 0.05		

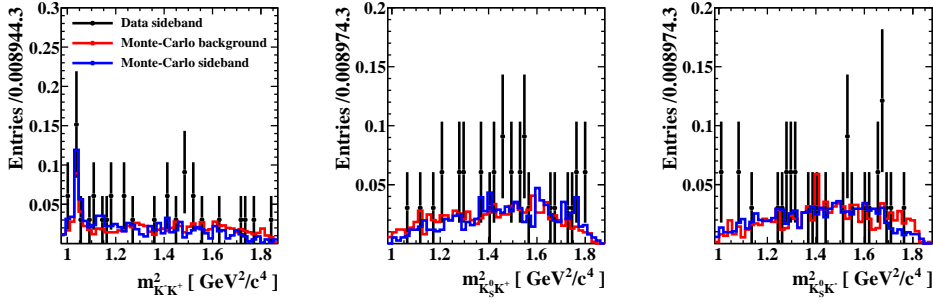


Figure 12.2: Comparison of data sideband sample (black) with Monte-Carlo background sample (red) and Monte-Carlo sideband sample (blue).

ground models within the signal region. The yields that we measure on the data and Monte-Carlo samples are listed in table 12.3. The fit to the Monte-Carlo sample shows that the true values can be reproduced and the fit to the data sample yields 1856 ± 45 signal and 70 ± 21 background events in total which gives a purity of 96.37 %. The total number of events in the data sample within the signal region is 1935 ± 44 . The contribution from each tag channels is listed in table 12.1. Number of signal and background events do not exactly add up to the total number of events since the extended maximum likelihood fit allows the total number of events to vary within its uncertainty. The fit to m_{BC} and m_{KS} is shown in fig. B.1. In the following we discuss the background amplitude model.

12.2 BACKGROUND

The background is studied using Monte-Carlo samples within the signal region, and using data and Monte-Carlo sideband samples. For the sideband region we accept all events outside a region of 10σ side length. Figure 12.2 compares the data sideband sample with Monte-Carlo sideband and Monte-Carlo background samples.

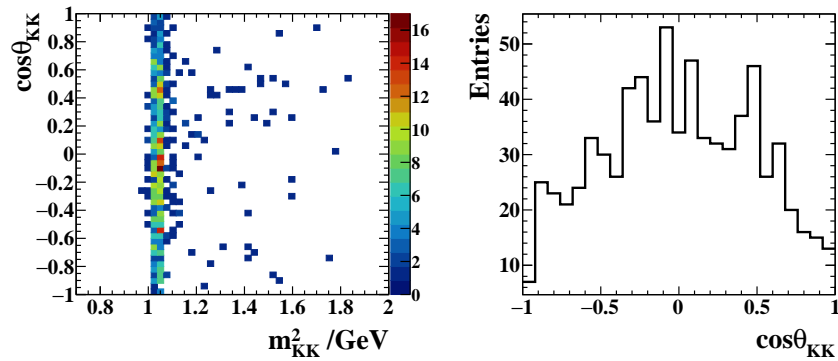


Figure 12.3: The decay the decay $D^0 \rightarrow (KK)_\phi(\pi\pi)_\rho$ is a peaking contribution to the background. We show the simulated distribution of K^+K^- invariant mass versus the corresponding helicity angle (right) and the projection of the helicity angle (left). We require that on generator level one of the D^0 decays to $\phi\rho$ and the other D^0 decays generically. Therefore, the sample contains a small number of misreconstructed candidates. Events are not corrected for reconstruction and selection efficiency.

In all samples a peaking background component shows up which originates from the decay $D^0 \rightarrow (KK)_\phi(\pi\pi)_\rho$. It is therefore part of the non- K_s^0 background component (see section 11.5) and is hard to suppress. The K^+K^- invariant mass distribution versus the helicity angle of this decay from simulation is shown in fig. 12.3. The decay of a pseudo-scalar (P) to two vector mesons (V) has a different structure compared to our signal decay ($P \rightarrow PPP$) and therefore, we do not see the vector particle nature of the $\phi(1020)$. The relative angular momentum between ϕ and ρ is zero in first order and its angular distribution is therefore expected to be flat. Considering that the events shown in fig. 12.3 are not efficiency corrected, the expectation is satisfied. The relative height of the peak to the phase-space component depends in the size of the signal and sideband regions.

The agreement of the background shape between data and simulation is reasonable and since background is low we do not expect a significant influence on our result. The nominal background model is determined from the Monte-Carlo background sample within the signal region. The sideband samples are used to estimate the systematic uncertainty.

We describe the background by a phenomenological model. This means we focus on a decent description without any demand on physical meaning. We build the model from a phase-space component and a peaking structure around $1 \text{ GeV}/c^2$ which is described by a Breit-Wigner amplitude model with the $\phi(1020)$ mass and width but with a spin zero angular distribution and in addition by a Breit-Wigner model with free mass and width. An accurate description would require a full analysis of the four particle final state which is beyond the scope of this work.

The fit to the Monte-Carlo background sample is shown in fig. 12.4 and the fit parameters are listed in table 12.4. Background model and the signal fraction

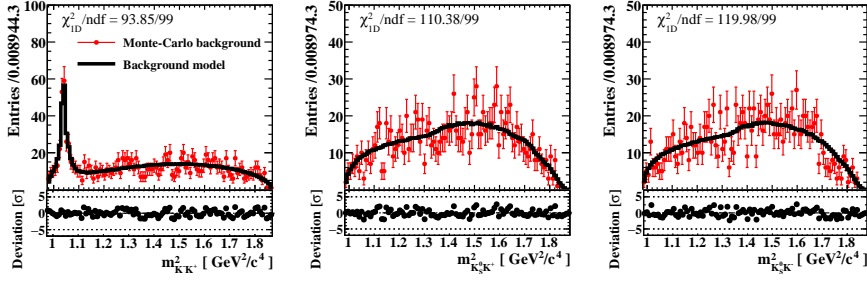


Figure 12.4: Projections of the Monte-Carlo background sample and the background model. The parameters of the background model are listed in table 12.4.

Table 12.4: Fit result for the background model. The Monte-Carlo background sample was used to determine the model parameters. The mass and width of the second Breit-Wigner amplitude are determined to be (1.025 ± 0.004) GeV/c² and (19.1 ± 7.1) MeV, respectively.

Component	Magnitude	Phase[rad]	Fit fraction[%]
$\phi(1020)$	$0.62^{+0.16}_{-0.07}$	$1.42^{+0.32}_{-0.33}$	83.8 ± 5.0
Breit-Wigner model	$0.39^{+0.21}_{-0.10}$	$-1.37^{+0.35}_{-0.33}$	32.4 ± 7.1
constant	1	0	12.4 ± 7.0
Total			129 ± 11

are inserted into the likelihood which is given in eq. (12.1).

12.3 LIKELIHOOD FUNCTION

The likelihood function is constructed as follows:

$$L(\xi, \beta) = f \cdot \frac{|\mathcal{M}(\xi, \beta)|^2}{\int |\mathcal{M}(\xi', \beta)|^2 \epsilon(\xi') d\xi'} + (1-f) \cdot \frac{|B(\xi)|^2}{\int |B(\xi')|^2 \epsilon(\xi') d\xi'}, \quad (12.1)$$

where $\mathcal{M}(\xi, \beta)$ and $B(\xi)$ are the signal and background Dalitz amplitude models. The efficiency function is denoted by $\epsilon(\xi)$ and the signal fraction (see section 12.1) by f . The normalization integrals are calculated using Monte-Carlo integration. The likelihood function is evaluated for each event and the logarithm of its products can be written as:

$$-\log \mathcal{L}(\beta) = -\sum_{\text{ev}}^N \log L(\xi_{\text{ev}}, \beta), \quad (12.2)$$

where N is the size of the data sample. The interesting physics parameters are the fit fractions which are defined as:

$$f_i = \frac{|c_i|^2 \int d\xi' |A_i(\xi')|^2}{\int d\xi' |\mathcal{M}(\xi')|^2}, \quad (12.3)$$

where c_i is the magnitude of resonance A_i . The integral $\int d\xi' |A_i(\xi')|^2$ is equal to one, due to our choice for the resonance normalization. Note that the normalization integral in the denominator does not include the efficiency function. A precise calculation of the statistical uncertainty of the fit fractions requires the propagation of the full covariance matrix through the integration. We use a Monte-Carlo approach to estimate the statistical uncertainty. Details are given in appendix B.3.

12.4 EFFICIENCY CORRECTION

We need to correct the events from data for the reconstruction and selection efficiency. We determine the reconstruction and selection efficiency at a certain point in phase-space using the signal Monte-Carlo sample. The sample consists of 30×10^6 events with resonant substructure and 50×10^6 events which are uniformly distributed in phase-space (see table 11.1). In this way we ensure that the efficiency is precisely calculated in the peak region and as well in the phase-space region with a small amplitude value. In contrast to the total efficiency required for the branching fraction measurement, the local efficiency here is not sensitive to the substructure of the signal Monte-Carlo sample.

We define the efficiency in bin i centered at ξ_i as:

$$\epsilon(\xi_i) = \frac{N^i}{N_{\text{gen}}^i}. \quad (12.4)$$

The position of an event in the Dalitz plot can be calculated from its generated or from its reconstructed values. We study the effect and find its influence negligible on the final result. We use the reconstructed phase-space position. The efficiency is visualised using the variables m_{KK}^2 and the helicity angle of the K^+K^- system $\cos \theta_{KK}$ in fig. 12.5. This representation is called Dalitz ‘box diagram’. Compared to the representation using two invariant masses it has the advantage that the phase-space boundary is a rectangle and does not intersect bins. The efficiency drops to zero in regions with low momentum K^+ and K^- tracks.

The efficiency correction using a histogram has disadvantages in regions with a large variation of the amplitude (e. g. close to the $\phi(1020)$). Therefore, we use the binned efficiency correction for visualization only and choose an unbinned efficiency correction approach for the minimization procedure, as described in the following.

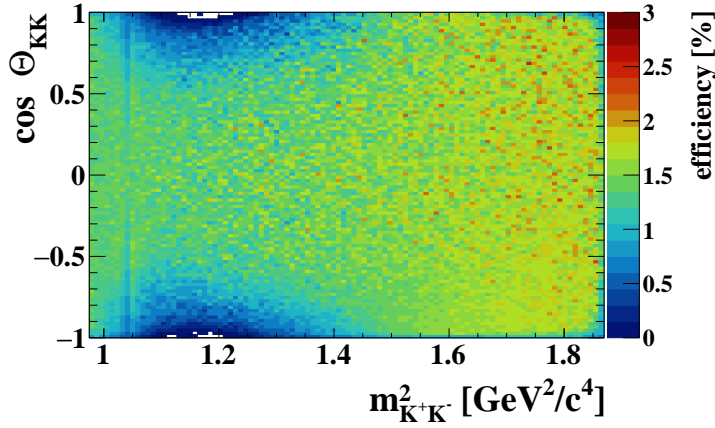


Figure 12.5: Simulated selection and reconstruction efficiency for tagged signal decays. The reconstructed phase-space position of the events is used.

The likelihood function from eq. (12.1) including the efficiency function is given by (we neglect the background term for simplicity):

$$L = \frac{|\mathcal{M}(\boldsymbol{\beta}, \boldsymbol{\xi})|^2 \epsilon(\boldsymbol{\xi})}{\int d\xi |\mathcal{M}(\boldsymbol{\beta}, \boldsymbol{\xi})|^2 \epsilon(\boldsymbol{\xi})}. \quad (12.5)$$

The coherent amplitude sum is denoted by $\mathcal{M}(\boldsymbol{\beta}, \boldsymbol{\xi})$, $\boldsymbol{\beta}$ are the free parameters in the fit and $\boldsymbol{\xi}$ are the Dalitz plot variables. The logarithm of the likelihood is then given by:

$$-\log \mathcal{L} = -\sum_{ev} \log \left(\frac{|\mathcal{M}(\boldsymbol{\beta}, \boldsymbol{\xi})|^2}{\int d\xi |\mathcal{M}(\boldsymbol{\beta}, \boldsymbol{\xi})|^2 \epsilon(\boldsymbol{\xi})} \right) - \sum_{ev} \ln \epsilon(\boldsymbol{\xi}). \quad (12.6)$$

In the minimization procedure the first derivative with respect the fit parameters $\boldsymbol{\beta}$ is calculated and therefore all terms not depending on $\boldsymbol{\beta}$ drop out. Therefore, the efficiency function is only relevant for the normalization term in the denominator. The normalization integral is calculated by Monte-Carlo integration and can be expressed as:

$$\begin{aligned} \mathcal{I} &= \int d\xi |\mathcal{M}(\boldsymbol{\beta}, \boldsymbol{\xi})|^2 \epsilon(\boldsymbol{\xi}) \\ &\approx \sum_{i=0}^{N_{gen}} |\mathcal{M}(\boldsymbol{\beta}, \boldsymbol{\xi}_i)|^2 \Delta x_i \epsilon(\boldsymbol{\xi}_i) \quad N_{gen} = \text{MC sample size.} \\ &= \frac{1}{N_{gen}} \sum_{i=0}^{N_{gen}} |\mathcal{M}(\boldsymbol{\beta}, \boldsymbol{\xi}_i)|^2 N_{gen} \Delta \xi_i \epsilon(\boldsymbol{\xi}_i) \\ &= \frac{1}{N_{gen}} \sum_{i=0}^{N_{gen}} |\mathcal{M}(\boldsymbol{\beta}, \boldsymbol{\xi}_i)|^2 N_{\xi_i}, \end{aligned} \quad (12.7)$$

where N_{ξ_i} is the number of accepted events. We write the integral as sum over all accepted events:

$$\begin{aligned} \mathcal{I} &= \frac{1}{N_{gen}} \sum_{i=0}^{N_{gen}} \sum_{j=1}^{N_{\xi_i}} |\mathcal{M}(\boldsymbol{\beta}, \boldsymbol{\xi}_i)|^2 \\ &= \frac{V_{phsp}}{N_{gen}} \sum_{k=1}^{N_{acc}} |\mathcal{M}(\boldsymbol{\beta}, \boldsymbol{\xi}_k)|^2 \quad \text{Sum over sample of accepted events.} \end{aligned} \quad (12.8)$$

We artificially add the phase-space volume of our decay V_{phsp} to obtain the correct units of the integral and for consistency with a binned efficiency correction. For the minimization process this factor is irrelevant since it drops in the first derivative.

This method allows to incorporate the efficiency correction directly into the likelihood normalization by using a isotropic Monte-Carlo sample with applied efficiency. That means we generate a large phase-space sample and after simulation, reconstruction and selection it can be used to correct the likelihood for efficiency in a non-parametric way. The knowledge of the efficiency function $\epsilon(\boldsymbol{\xi})$ is not necessary. Binned and unbinned approaches calculate the likelihood normalization consistently on a level better than 1 % and the effect on the fit result is negligible.

Both approaches depend on an accurate simulation of the track reconstruction. The differences between simulation and data were studied by the collaboration in bins of the particle momentum. The relative differences are listed in table B.2. To each Monte-Carlo event in the isotropic sample we assign a correction factor depending on the momenta of K_s^0 , K^+ and K^- to consider those differences.

12.5 GOODNESS-OF-FIT

We need a goodness-of-fit procedure to quantify the agreement between our model hypothesis and the data sample. Furthermore we need to rank the agreement of different sets of amplitudes in order to find an optimal set of resonances.

A common approach is the χ^2 test. The data sample is divided into bins and from the number of entries N_i and the function value at the bin center $f(\vec{x}_i)$ we calculate:

$$\chi^2 = \frac{N_i - f(\vec{x}_i)}{\sigma_i}. \quad (12.9)$$

In case that the uncertainties on the values in each bin are Poisson distributed the χ^2 distribution follows a regularized Gamma function. Our data sample has a rather limited size and the strong contributions from $\phi(1020)$ and $a_0(980)^0$ at low K^+K^- invariant masses leads to regions in phase-space with essentially

no events as shown in fig. 12.1.¹ Fortunately there are many more powerful tests on the market. An overview is given in [71].

We use an unbinned point-to-point dissimilarity goodness-of-fit method which is often refer to as ‘statistical energy’ test. This approach compares directly the unbinned probability densities of two samples. The application to problems in particle physics was first discussed in [72]. Further (technical) hints can be found in [71]. The method performs much better compared to a χ^2 test in omnipresent as well as localized discrepancies.

As a complement to the point-to-point dissimilarity method we use the well-known likelihood-ratio test to calculate the relative significance of amplitude models (see section 12.5.2).

12.5.1 Point-to-Point dissimilarity test

The basic idea is to use an analogy to the electrostatic energy as test variable for the comparison of two unbinned samples. Lets assume a continuous charge distribution $\rho(\mathbf{x})$ which can be splitted into distributions for the negative and positive charges:

$$\rho(\mathbf{x}) = \rho_+(\mathbf{x}) - \rho_-(\mathbf{x}). \quad (12.10)$$

The electrostatic potential writes as:

$$\Phi = \frac{1}{2} \int d\mathbf{x} \int d\mathbf{y} \frac{[\rho_+(\mathbf{x}) - \rho_-(\mathbf{x})][\rho_+(\mathbf{y}) - \rho_-(\mathbf{y})]}{|\mathbf{x} - \mathbf{y}|}. \quad (12.11)$$

In case both distributions are equally distributed the electrostatic energy is minimal. We considering ρ_{\pm} to be probability density functions (PDF) and we substitute $\frac{1}{|\mathbf{x}-\mathbf{y}|}$ by a general distance function $R(|\mathbf{x} - \mathbf{y}|)$. Our test variable becomes:

$$\begin{aligned} 2\Phi &= \int d\mathbf{x} \int d\mathbf{y} \rho_+(\mathbf{x})\rho_+(\mathbf{y})R(|\mathbf{x} - \mathbf{y}|) \\ &+ \int d\mathbf{x} \int d\mathbf{y} 2\rho_+(\mathbf{x})\rho_-(\mathbf{y})R(|\mathbf{x} - \mathbf{y}|) \\ &+ \int d\mathbf{x} \int d\mathbf{y} \rho_-(\mathbf{x})\rho_-(\mathbf{y})R(|\mathbf{x} - \mathbf{y}|). \end{aligned} \quad (12.12)$$

In the following we identify $\rho_+ = \rho_{data}$ as the true and unknown PDF of our data sample and $\rho_- = \rho_{mc}$ as the amplitude model obtained from the Dalitz plot analysis. In the next step we approximate the integrals over ρ_{data} and ρ_{mc} by Monte-Carlo integration. We use our data sample of size N for the integrals over ρ_{data} and for ρ_{mc} we generate a large Monte-Carlo sample of size M using

¹ Despite that, we give the χ^2 values for the invariant mass projections in fig. 12.10.

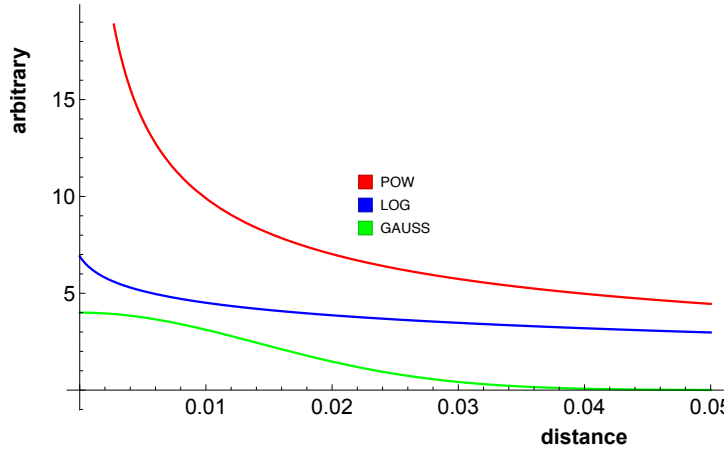


Figure 12.6: Illustration of different distance functions.

our amplitude model. The Monte-Carlo sample has passed detector simulation, reconstruction and selection. Φ is then calculated using two unbinned samples:

$$\begin{aligned} \Phi &= \frac{1}{N(N+1)} \sum_{j>i} R(|\mathbf{n}_i - \mathbf{n}_j|) \\ &\quad - \frac{1}{NM} \sum_{j,i} R(|\mathbf{n}_i - \mathbf{m}_i|) \\ &\quad + \frac{1}{M(M+1)} \sum_{j>i} R(|\mathbf{m}_i - \mathbf{m}_j|). \end{aligned} \quad (12.13)$$

Here \mathbf{m}_i and \mathbf{n}_i are elements from the Monte-Carlo and data sample, respectively. This variable can be used to rank different sets of amplitudes or different amplitude descriptions. In contrast to [71, 72], we do not drop the last term since we think that without this term it is not ensured that models with better fit quality always have smaller values in Φ . We did not treat prefactors carefully, in particular the unit of Φ is not correct. However this is irrelevant for the usage of Φ as goodness-of-fit test variable. Furthermore it is in general necessary to rescale the phase-space variables to a common range or common width. Since we are using two invariant masses with almost the same range to calculate the Dalitz plot position this is not necessary in our case. In the next section we discuss our choice for the distance function $R(|\mathbf{x} - \mathbf{y}|)$.

12.5.1.1 Distance function

In the literature [71, 72] three different distance functions are discussed:

1. Power-law $R(|\mathbf{x} - \mathbf{y}|) = (|\mathbf{x} - \mathbf{y}|^\kappa + \epsilon)^{-1}$
2. Logarithmic $R(|\mathbf{x} - \mathbf{y}|) = -\log(|\mathbf{x} - \mathbf{y}| + \epsilon)$
3. Gaussian $R(|\mathbf{x} - \mathbf{y}|) = \exp\left(\frac{-|\mathbf{x} - \mathbf{y}|}{2\sigma^2}\right)$

The power-law and logarithmic distance functions have a numerical cut-off ϵ . The exponent of the power-law function κ and the width of the Gaussian

σ are nuisance parameters. The different distance functions are illustrated in fig. 12.6. The power-law and logarithmic distance functions have infinite range. That means pairs of events can contribute to the value of Φ even if they are far away from each other and therefore only weakly correlated. We consider this as unphysical and use the Gaussian distance function. The width can be considered as a correlation range. We choose a width which is allowed to vary over the Dalitz plot, as proposed in [71]. The local ‘correlation range’ at the Dalitz position ξ is calculated from an average correlation range $\bar{\sigma}$ scaled by the amplitude value at that point:

$$\sigma(\xi) = \frac{\bar{\sigma}}{\mathcal{M}(\xi) \int d\xi}. \quad (12.14)$$

The idea is that in regions with low amplitude values and therefore with few events the width is larger compared to regions with high amplitude values and many events. The phase-space factor $\int d\xi$ is added because the expectation value of $\mathcal{M}(\xi) \int d\xi$ is one. The variable width improves the power of the test significantly as studied in [71]. The nuisance parameter $\bar{\sigma}$ is set to an ‘average width’ of all resonances in the Dalitz plot. We choose 30 MeV. The influence of this parameter is considered to be small.

12.5.1.2 Probability distribution

The test variable Φ can be used to measure the agreement relative to another solution. We want to calculate the probability that our amplitude model is the underlying amplitude of the data sample. The probability \mathcal{P}_{fit} can be calculated from the distribution $\mathcal{D}_{\text{fit}}(\Phi)$ of the test variable Φ :

$$\mathcal{P}_{\text{fit}} = \int_{-\infty}^{\Phi_{\text{fit}}} \mathcal{D}_{\text{fit}}(\Phi) d\Phi. \quad (12.15)$$

In case of a χ^2 test the χ^2 distribution is analytically known. For the ‘statistical energy’ test we have to obtain the distribution from simulation. We use the amplitude \mathcal{M}_{fit} to generate two samples. One sample with the same size as the data sample N and a second sample with the same size M as the Monte-Carlo sample that was used to calculate Φ . These pairs are generated multiple times, and for each we calculate Φ_i . The distribution $\mathcal{D}_{\text{fit}}(\Phi)$ follows a Gaussian shape and is shown in fig. 12.7. The probability can then be obtained by eq. (12.15). For technical reasons the Monte-Carlo sample that is used here is limited to about 16×10^3 events. Therefore, the value of Φ has a statistical uncertainty which is 3.7×10^{-6} for the final amplitude model.

12.5.2 Likelihood ratio test

The Dalitz amplitude model consists of the coherent sum of a set of resonances. The agreement between data sample and model is given by the value of the likelihood function at its minimum. A model with more parameters usually yields a better fit quality. We need to test if a model with additional resonances

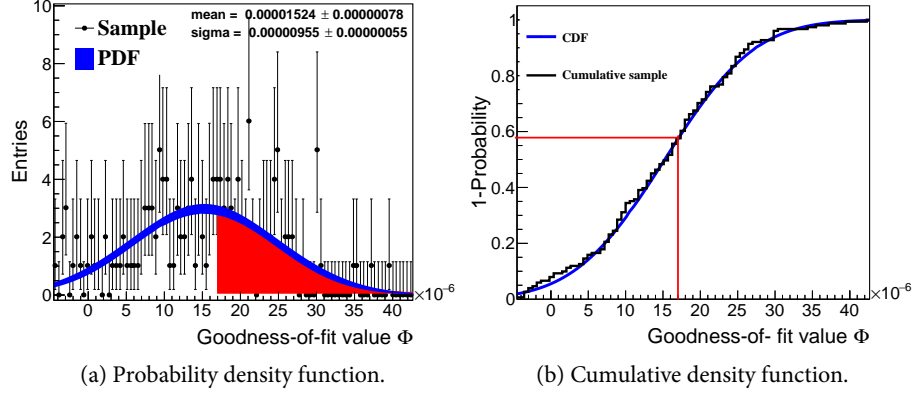


Figure 12.7: The fit probability of the final model for the Point-to-Point dissimilarity method is estimated from a set of Monte-Carlo samples. The goodness-of-fit value Φ is 17×10^{-6} which gives a fit probability of $(42.6 \pm 3.0) \%$.

results is a significantly improved description. In ‘statistics language’ this means we have to test the significance of composite statistical hypotheses. Composite statistical hypotheses means that the null hypothesis (with less parameters) is within the parameter space of the alternative hypothesis (with more parameters). In our case both models are approximately the coherent sum of different sets of resonances and if one set is a subset of the other we can apply the likelihood ratio test.

We calculate the ratio of both likelihoods at the minimum:

$$Q_{\mathcal{L}} = -2 \log \frac{\mathcal{L}(\text{null hypothesis})}{\mathcal{L}(\text{alternative hypothesis})}. \quad (12.16)$$

Wilks theorem [73] states that for the case of hypothesis testing described above, $Q_{\mathcal{L}}$ is distributed according a χ^2 distribution with n degrees of freedom:

$$\chi^2(Q_i; n) = \frac{Q_i^{n/2-1} e^{-Q_i/2}}{2^{n/2} \Gamma(\frac{n}{2})}. \quad (12.17)$$

In which n is the difference of degrees of freedom between the null and the alternative hypothesis. For a sample size approaching infinity, Wilks theorem is exact.

We obtain the probability from the χ^2 cumulative distribution function:

$$\mathcal{P}(Q_{\mathcal{L}}) = \int_{-\infty}^{Q_{\mathcal{L}}} \chi^2(x, n) dx. \quad (12.18)$$

And the significance in units of the standard deviation of the normal distribution is given by:

$$s(\mathcal{P}) = \sqrt{2} \operatorname{erf}^{-1}(\mathcal{P}). \quad (12.19)$$

Table 12.5: Comparison of different results for the $f_0(980)$ parameters. Other measurements are listed in [75, Table 2]. The BESII result is corrected for a different phase-space factor (second row).

Measurement	Mass [MeV/c ²]	$g_{K\bar{K}}$ [GeV]	$g_{\pi\pi}$ [GeV]	$2g_{K\bar{K}}^2/g_{\pi\pi}^2$
Ambrosino <i>et al.</i> [74] $e^+e^- \rightarrow \pi^0\pi^0\gamma(\text{KL})$	976.8 ± 10.1	3.76 ± 1.17	-1.43 ± 0.60	13.8 ± 7.8
García-Martín <i>et al.</i> [75] $\pi\pi$ scattering, K_{4l}	-	-	2.3 ± 0.2	-
Ablikim <i>et al.</i> [76] $J/\psi \rightarrow \phi\pi^+\pi^-, \phi K^+K^-$	965 ± 10	0.49 ± 0.07 3.5 ± 0.5	0.165 ± 0.018 1.17 ± 0.13	17.7 ± 2.7
Weighted average	971 ± 7	3.54 ± 0.46	1.5 ± 0.1	17.3 ± 2.6

This is the quantile function of the normal distribution with zero mean and a width of one. The inverse error function $\text{erf}^{-1}(x)$ is used.

12.6 RESONANCES

In this section we collect information on the resonances that can appear as intermediate states in the decay $D^0 \rightarrow K_s^0 K^+ K^-$. The phase-space range is in all Dalitz variables approximately from 1 to 1.364 GeV/c². We are looking for resonances in this mass window which decay to $K\bar{K}$. The kaons have quantum numbers $J^P = 0^-$ and therefore the allowed quantum numbers from the constituent quark model for intermediate resonances are $J^{PC} = 0^{++}, 1^{--}, 2^{++}$ and so on.

All resonances listed by the PDG [7] that fulfill those requirements are discussed in the following. An overview is given in table 12.7.

- The $f_0(980)$ is expected to be the isospin 0 component of a nonet, built from the $a_0(980)$, the $K^*(800)$ and the $f_0(600)$ (see fig. 1.3). It lies close to the $K\bar{K}$ threshold and couples strongly to the charged and neutral final states of $K\bar{K}$ and $\pi^+\pi^-$. The f_0 couplings to KK and $\pi\pi$ were measured by e. g. KLOE [74]. An overview of different measurements is given in table 12.5. Since it has the same quantum numbers and mass as the $a_0(980)^0$, and only slightly different coupling, both will be hard to distinguish. Since we see a contribution from $a_0(980)^+$ in the $K_s^0 K^+$ channel we also expect a $a_0(980)^0$ contribution in the $K\bar{K}$ channel.
- The $a_0(980)$ is located close below the $K\bar{K}$ threshold. It couples strongly to the $\eta\pi$ as well as to the $K^+K^-/K^0\bar{K}^0$ channel. The charged $a_0(980)$ has only the channels $K_s^0 K^\pm$ and $\eta\pi^\pm$ while the neutral partner also decays via $K^0\bar{K}^0$. This is taken into account by using two and three channel formulas (see section 5.3). The coupling to the $K\bar{K}$ channel can be determined on data. The $a_0(980)$ mass and the coupling to $\eta\pi$ are external

Table 12.6: Comparison of different results for the $a_0(980)$ parameters. One can clearly see that measurements from χ_{cJ} decays systematically differs from the other measurements. Some measurements use a different phase-space factor than we do. The corrected values are given in the second line.

Measurement	Mass [MeV/c ²]	$g_{K\bar{K}}[\text{GeV}]$	$g_{\eta\pi}[\text{GeV}]$	$2g_{K\bar{K}}^2/g_{\eta\pi}^2$
Teige <i>et al.</i> [83] $\pi^- p \rightarrow \{\eta\pi^+\pi^-, \eta\pi^0 n\}$	1001.0 ± 1.9	0.15 ± 0.02 1.1 ± 0.2	0.240 ± 0.015 1.7 ± 0.1	0.8 ± 0.2
Abele <i>et al.</i> [82] $p\bar{p} \rightarrow K_L K^\pm \pi^\pm$	999 ± 2	0.23 ± 0.02 1.6 ± 0.1	0.324 ± 0.015 2.3 ± 0.1	1.03 ± 0.14
Bugg [78] $p\bar{p} \rightarrow$ $\{\eta\pi^0\pi^0, K_L\pi^\pm K^\pm, \omega\pi^+\pi^-\pi^0\}$	987.4 ± 3.2	0.29 ± 0.02 2.1 ± 0.1	0.405 ± 0.015 2.9 ± 0.1	1.05 ± 0.09
Ambrosino <i>et al.</i> [77] $\phi(1020) \rightarrow \eta\pi^0\gamma(\text{KL})$	982.5 ± 2.0	2.15 ± 0.08	2.82 ± 0.05	1.16 ± 0.08
Athar <i>et al.</i> [79] $\chi_{cJ} \rightarrow h^+ h^- h^0$	1002 ± 18	0.4 ± 0.1 2.6 ± 0.8	0.64 ± 0.05 4.5 ± 0.4	0.66 ± 0.39
Adams <i>et al.</i> [80] $\chi_{c1} \rightarrow \{\eta\pi^+\pi^-, \eta^+\pi^+\pi^-\}$	998 ± 16	0.40 ± 0.08 2.8 ± 0.6	0.60 ± 0.04 4.3 ± 0.3	0.87 ± 0.35
Weighted average	994 ± 1	1.89 ± 0.06	2.66 ± 0.04	1.05 ± 0.04

input parameters. Recent measurements comes from KLOE [77], from a reanalysis of Crystal Barrel data [78] and from CLEO-c [79, 80]. At BESIII there is an ongoing measurement of these parameters in the decay $\chi_{c1} \rightarrow \eta\pi^+\pi^-$. The analysis is currently in review stage [81]. An overview over all measurements is listed in table 12.6. In the KLOE analysis the ratio of the couplings is defined as $g_{K^+K^-}^2/g_{\eta\pi}^2$ in all other analysis the ratio is defined as $(g_{K^+K^-}^2 + g_{K^0\bar{K}^0}^2)/g_{\eta\pi}^2 \approx 2g_{K^+K^-}^2/g_{\eta\pi}^2$. The coupling constants from different analysis need to be corrected for different parametrizations, namely for the two-body phase-space factor a different formula are used. It is not completely clear which formula were used for the χ_{cJ} analyses. In case that our assumption for the phase-space factor is correct, there is a systematic discrepancy between values obtained in χ_{cJ} decays and the other analyses. In the previous analysis by *BABAR* the result from [82] was used. We use the weighted average for the $a_0(980)$ mass and coupling to $\eta\pi$.

- The most precise measurement of the $\phi(1020)$ mass and width was performed by the *BABAR* experiment using initial state radiation in the final state $e^+e^- \rightarrow K\bar{K}(\gamma)$ [84]. A mass of (1019.51 ± 0.05) GeV/c² and a width of (4.29 ± 0.08) MeV were measured. For our analysis we use the PDG average values, shown in table 12.7. The $\phi(1020)$ is described by a Breit-Wigner model with mass-depended width.

Table 12.7: Overview of resonances that can contribute to the decay $D^0 \rightarrow K_s^0 K^+ K^-$. Mass and width are the Breit-Wigner parameters. In case that these are channel depended we quote the parameters of the $K\bar{K}$ final state. Values without reference are the averaged values from the particle data group [7].

Resonance	$I^G (J^{PC})$	$\mathcal{B}_{K\bar{K}}[\%]$	Mass[MeV/c ²]	Width[MeV]
$f_0(980)$	$0^+(0^{++})$	seen	971 ± 7	$g_{K\bar{K}} = 3.54 \pm 0.05$ $g_{\pi\pi} = 1.5 \pm 0.1$
$a_0(980)$	$1^-(0^{++})$	seen	994^{+6}_{-4}	$g_{\eta\pi} = 2.66 \pm 0.04$
$\phi(1020)$	$0^-(1^{--})$	48.9 ± 0.5	1019.461 ± 0.019	4.266 ± 0.031
$f_2(1270)$	$0^+(2^{++})$	4.6 ± 0.4	1275.1 ± 1.2	$184.2^{+4.0}_{-2.4}$
$a_2(1320)$	$1^-(2^{++})$	4.9 ± 0.8	1318.1 ± 0.7	109.8 ± 2.4
$f_0(1370)$ [87]	$0^+(0^{++})$	seen	1440 ± 6	121 ± 15
$\rho(1450)$ [89]	$1^+(1^{--})$	not seen	1422.8 ± 6.5	146.5 ± 10.5

- The parameters for the $f_2(1270)$ are determined in the final state $\pi\pi$. For example at BESII in the reactions $e^+e^- \rightarrow J/\psi \rightarrow \gamma\pi^+\pi^-$ [85] and $J/\psi \rightarrow \phi\pi^+\pi^-$ [76]. We use the PDG average value.
- The mass and width of the $a_2(1320)$ in the $K\bar{K}$ channel were determined in the 1980s for example in the reaction $\pi^\pm p \rightarrow K_s^0 K^\pm p$ [86]. All measurements are in good agreement and we use the PDG average values.
- The properties of the $f_0(1370)$ are rarely known and there is also a discrepancy between different measurements. The particle data group assumes a complex pole position in the range of $(1200 - 1500) - i(150 - 250)\text{MeV}$. We use the mass and width published in [87]. This measurement is the most recent one and is in agreement with measurements from the 1980s.
- Input to the particle data group averages for mass and width of the $a_0(1450)$ comes from the Crystal Barrel collaboration. The results from the final states $p\bar{p} \rightarrow K_L^0 K^\pm \pi^\pm$ [82] and $p\bar{p} \rightarrow \{\pi^0\pi^0\pi^0, \pi^0\eta\eta, \pi^0\pi^0\eta\}$ [88] are consistent. We use the PDG average.
- The $\rho(1450)$ parameters are not precisely known. The Crystal Barrel experiment measured them in the reaction $p\bar{p} \rightarrow K^+ K^- \pi^0$. A mass of $(1422.8 \pm 6.5)\text{GeV}/c^2$ and a width of $(146.5 \pm 10.5)\text{GeV}$ were observed [89]. The isospin was not determined and there is the possibility to confuse it with the $\omega(1420)$. The $\rho(1450)$ has not been observed in the channel $K\bar{K}$ and we do not include it in our model. Yet we list it for completeness here.

12.7 MODEL SELECTION

In the following we discuss how we choose the set of resonances that we included into the Dalitz amplitude model. The particle data group [7] lists 12 resonances that could potentially contribute to the decay $D^0 \rightarrow K_s^0 K^+ K^-$. The fit result for an amplitude model including all resonances is given in table 12.8. The sum of fit fractions is 196.64 % which is due to large interferences. Those can be of physical origin but it is also possible that the minimization procedure adds intensity to two or more resonances which is then compensated by a larger destructive interference. In the end more intensity can be added without an improved fit quality. Furthermore many resonances have small fit fractions and we want to remove those which do not significantly contribute.

Those problems are common in amplitude analyses and an often used strategy is to subsequently remove insignificant resonances from the model with the maximum set of resonances. Usually one introduces a cut-off in the fit fraction or on the significance of a resonance. This cut-off is somehow arbitrary and more importantly this procedure does not balance between a more complex model and an improved fit quality.

In contrast to this approach, we use a strategy that automatically balances between improved fit quality and model complexity and furthermore, does not involve any arbitrary parameters. This strategy is described in the following.

12.7.1 Penalty term

Balancing a model between fit quality and model complexity is a very common problem in the area of machine learning and in statistics in general. One approach to solve such a problem is the so-called Least Absolute Shrinkage and Selection Operator (LASSO) method [90]. The basic idea is to penalize undesired behaviour of the objective function. In the original approach the objective function is a least square model and the penalty function is the sum of the absolute values of the free parameters.

In the context of particle physics this approach is described in [91]. In our case the objective function is $-\log \mathcal{L}$ and the undesired behavior is a large sum over all fit fractions. Therefore, we use the square-root of the sum of fit fractions as penalty function. We modify eq. (12.2) as follows:

$$-\log \mathcal{L}_P = -\log \mathcal{L} + \lambda_P \sum_i \sqrt{\frac{\int A_i A_i^* d\xi}{\int \sum_{i,j} A_i A_j^* d\xi}}. \quad (12.20)$$

The square-root is used here since it favors the suppression of small contributions, in contrast to e. g. the sum of the fit fractions which would favor solutions with equal values. The parameter λ_P regularizes the model complexity. A large value suppresses the sum of fit fractions and small values allow for larger interference terms. It is a nuisance parameter and we have to determine its optimal value. Again, this is a common problem in statistics and the class of solutions are so-called information criteria. Information criteria are mathematical formu-

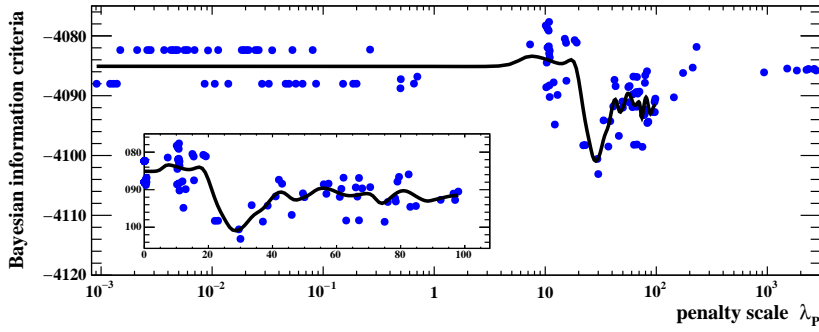


Figure 12.8: Scan of penalty scale λ_p . The BIC information criterion is shown with a minimum at $\lambda_p^{min} = 30.0$. A spline function (black) to the data points is shown to guide the eye.

lations of the ‘principle of parsimony’ [92]. This means in hypothesis testing we prefer the model with less parameters over a more complicated model, given the same goodness-of-fit.

The criteria suggested by [91] are the Akaike (AIC) [93] and Bayesian (BIC) [92] information criteria:

$$AIC_{\lambda_p} = -2 \log \mathcal{L}_{\lambda_p} + 2r_{\lambda_p} \quad BIC_{\lambda_p} = -2 \log \mathcal{L}_{\lambda_p} + r_{\lambda_p} \log N_{data}. \quad (12.21)$$

The number of events in data is denoted by N_{data} and the coefficient r is related to the complexity of the model. We follow the suggestion of [91] and use the number of resonances with a fit fraction larger 10^{-3} as parameter r . This somehow also introduces a cut off however, not directly in the resonance selection but in the scale for the complexity of the model. By construction, the BIC prefers less complex models compared to the AIC.

We perform a scan for different values of λ_p over a wide range and map out the minima of AIC and BIC. The scan is shown in fig. 12.8. Since the for many values of λ_p the minimization procedure is numerically instable we have to use different starting values for the model parameters to find valid minima over the whole range of λ_p . Nevertheless in some intervals minimization does not succeed. We find a minimum for BIC at $\lambda_p = 30.0$ but no minimum for AIC. The fit result at the minimum is listed in table 12.8. The sum of fit fractions decreases from 196.64 % for $\lambda_p = 0.0$ to 159.67 % for λ_p at the BIC minimum. We test the influence on the final set of different values of λ_p close to the minimum and find that the result depends only weakly on the exact value of λ_p . Some values tend to add $a_2(1320)^-$ to the model and some do not. We keep the $a_2(1320)^-$ and test its significance. A disadvantage of this method is that the error estimate of the fitting procedure is inaccurate due to the additional term in $-\log \mathcal{L}$. Therefore, we remove the penalty term and all resonances with a fit fraction $< 10^{-3}$ and rerun the fit.

The final model includes the resonances $a_0(980)^0$, $\phi(1020)$, $a_0(980)^+$ and $a_2(1320)^-$.

Table 12.8: Fit fractions in % of different sets of resonances. The significance is calculated from a likelihood ratio test with respect to the final model. A negative significance indicates that the likelihood is worse than the reference model.

Resonance	Complete	BIC min $\lambda_P^{min} = 30.0$	Final model	Significance $a_2(1320)^-$	
g_{KK} [GeV]	2.78 ± 0.56		$2.87^{+0.23}_{-0.28}$	3.21 ± 0.18	
$f_0(980)$	17.55	2×10^{-4}			
$a_0(980)^0$	41.89	74.95		72.8 ± 4.7	77.9 ± 4.1
$a_0(980)^+$	37.28	35.34		31.9 ± 4.7	38.0 ± 2.8
$a_0(980)^-$	6.04	7.4×10^{-2}			
$\phi(1020)$	49.81	48.61		47.5 ± 1.6	47.2 ± 1.4
$f_2(1270)$	3.43	2×10^{-4}			
$a_2(1320)^0$	1.51	3×10^{-2}			
$a_2(1320)^+$	2.55	5×10^{-2}			
$a_2(1320)^-$	0.205	0.55		0.78 ± 0.40	
$f_0(1370)$	8.73	2×10^{-5}			
$a_0(1450)^0$	1×10^{-11}	7×10^{-9}			
$a_0(1450)^+$	9.14	1×10^{-7}			
$a_0(1450)^-$	18.52	9×10^{-9}			
Total	196.64	159.67		153.0 ± 7.6	163.1 ± 5.1
Degrees of freedom	25			7	5
$-\log \mathcal{L}$	-4149.98		-4125.78	-4116.69	
Significance	3.82		-	-3.88	
Goodness-of-fit	0		1.701×10^{-5}	1.680×10^{-5}	
Fit probability [%]	0		42.6 ± 3.0	24.6 ± 2.0	

12.8 SYSTEMATICS

In the following we describe how we estimate the systematic uncertainties on the fit parameters and the fit fractions. These include an uncertainty from the fitting procedure, the background description, the amplitude model and inaccuracies of the Monte-Carlo simulation. For each source of uncertainty we rerun the fit with a different configuration and add the deviations from the nominal model in quadrature. An overview of the systematic uncertainties for the nominal model is given in table 12.11 (and an extensive overview in table B.3).

12.8.1 Background

The result is influenced by the background description in various ways. The background amplitude model can influence the fit result. This in turn is influenced by the background sample that is used to determine the parameters and by the amplitude model parametrization. The fit quality for the Monte-Carlo background sample is fairly good, as shown in fig. 12.4. We therefore neglect the uncertainty due to an insufficient description of the background model. Instead we test different background samples. The nominal model is determined from a Monte-Carlo background sample in the signal region. We substitute it by the data sideband sample and the Monte-Carlo background sideband sample. The difference of the fit result in comparison to the nominal model is taken as systematic uncertainty. Note that the contribution to the $\phi(1020)$ peak is different for the signal and sideband region. The systematic uncertainty is therefore a conservative assumption.

Another source of uncertainty is the signal purity. It is obtained on data as explained in section 12.1. Since the yields are not efficiency corrected we assume that the systematic uncertainty on this is negligible. The systematic effect on the Dalitz plot analysis is estimated by varying the signal fraction by one standard deviation of its statistical uncertainty to larger and smaller values.

12.8.2 Amplitude model

A source of uncertainty of the amplitude model is the resonance radius that is used in the damping factors (see section 5.4). We vary it in steps of 1 GeV^{-1} from 0 GeV^{-1} to 5 GeV^{-1} . Our nominal value is 1.5 GeV^{-1} .

The quantum entanglement of $D^0\bar{D}^0$ is included in the Dalitz amplitude model. We use external parameters for the magnitude and phase of

$$\lambda_j = \frac{\mathcal{A}_j}{\bar{\mathcal{A}}_j} = -\sqrt{R_D} e^{-i\delta_D}, \quad (6.3)$$

which we denote by R_D and δ_D . Both depend on the final state but are not measured for each final state that we use for tag reconstruction. As nominal values we use the experimental averages for $K^- \pi^+$ which are listed in table 7.1.

Table 12.9: Charm mixing averages from HFAG [38].

Parameter	Value
x[%]	0.53 ± 0.17
y[%]	0.63 ± 0.09
R_D [%]	0.350 ± 0.004
$\langle R_D^{K^- \pi^+ \pi^0} \rangle$	0.164 ± 0.027
$\delta_{K\pi}$ [°]	10 ± 11
$\delta_{K\pi\pi^0}$ [°]	17 ± 23

We use the value of R_D for the final state $K^- \pi^+ \pi^0$ and two times the nominal value to study the influence of the magnitude on the final result. For the phase δ we use the values 0 and two times its nominal value. The fit result for a Dalitz amplitude model without quantum entanglement ($r_D = 0$) is listed in table B.6.

12.8.3 Monte-Carlo simulation

The efficiency correction of the data sample is obtained from Monte-Carlo simulation. Differences between data and Monte-Carlo simulation in track reconstruction and particle-identification can influence the result. Especially the regions with low momentum K^\pm tracks are prone to inaccuracies. We correct for these differences using momentum depended correction factors provided by the collaboration. The corrections are listed in appendix B.4. We test the influence of the tracking correction by rerunning the fit without correction (table B.3). The influence is found to be small and we do not assign a systematic uncertainty.

Another effect are different momentum resolutions in data and Monte-Carlo simulation. The $\phi(1020)$ has a width which is of the same order as the mass resolution. We study the influence of the mass resolution by rerunning the minimization with a free width parameter. The parameter changes from 4.266 MeV to (5.08 ± 0.28) MeV. We add the deviation from the nominal model to the systematic uncertainty. The likelihood difference of both configurations has a statistical significance of 2.82σ . We decide to keep the parameter fixed in the nominal model.

12.8.4 External parameters

A list of external parameters used in this analysis is shown in table 12.10. We shift each parameter by its uncertainty to smaller and larger values and rerun the minimization. The deviation from the nominal model is taken as systematic uncertainty. The influence of the $a_0(980)$ coupling to $\eta\pi$ is estimated by rerunning the minimization with both couplings left free. We obtain $g_{\eta\pi} = (2.62 \pm 0.11)$ GeV.

12.8.5 Fitting procedure

The fitting procedure can introduce a bias on the fit result. Furthermore we need to assure that the estimation of the statistical uncertainty calculated by MINUIT is correct. This study accounts for the following contributions to the systematic uncertainty:

1. Correlations between parameters.
2. Efficiency correction.
3. Reconstruction effects (e. g. a shift in phase-space position).

Table 12.10: List of external parameters with uncertainties.

Name	Value
$a_0(980)$ mass	$(0.994^{+6}_{-4}) \text{ GeV}/c^2$
$a_0(980) g_{\eta\pi}$	2.66 GeV
$\phi(1020)$ mass	$(1.019\,461 \pm 0.000\,019) \text{ GeV}/c^2$
$\phi(1020)$ width	$(4.266 \pm 0.031) \text{ MeV}$
$a_2(1320)$ mass	$(1.3181 \pm 0.0007) \text{ GeV}/c^2$
$a_2(1320)$ width	$(109.8 \pm 2.4) \text{ MeV}$
$a_0(1450)$ mass	$(1.474 \pm 0.019) \text{ GeV}/c^2$
$a_0(1450)$ width	$(265 \pm 13) \text{ MeV}$

We use our nominal fit result to generate a signal Monte-Carlo sample by using a hit-and-miss method. This sample has passed detector simulation and reconstruction as well as the event selection procedure. Then, we add the expected amount of background from Monte-Carlo simulation and rerun the minimization procedure. We calculate the difference between the parameters of the nominal model and the fit result in units of the statistical uncertainty of the parameter. This quantity is denoted by:

$$\mathcal{P}_\beta = \frac{\boldsymbol{\beta}_{\text{true}} - \boldsymbol{\beta}}{\sigma_\beta}. \quad (12.22)$$

We repeat this procedure for 150 statistically independent samples. The distribution of \mathcal{P}_β is expected to be Gaussian with a mean of zero with a width of one. A shifted mean indicates the average bias on the parameter of interest. A width larger or smaller than one is a hint on an under- or overestimation of the statistical uncertainty.

The distribution for \mathcal{P}_β is shown in fig. B.3. We find significant biases for some parameters. Especially the parameters of the $a_2(1320)^-$ are significantly shifted. Note that these shifts are given in units of the statistical uncertainty and are therefore small in absolute values. We correct each fit parameter for its bias and add half of the correction to the systematic uncertainty.

The widths of the distributions are compatible with one. Despite this we perform an additional χ^2 test on the error estimate to assure that the confidence intervals are well covered. We use the likelihood ratio test described in section 12.5.2. We have a set of true parameters $\boldsymbol{\beta}_{\text{true}}$. From these parameters independent samples are generated, as described above. The fit to each sample i gives us a set of parameters $\boldsymbol{\beta}_{\text{min}}^i$ at the minimum as well as the value of the likelihood at this point $-\log \mathcal{L}_{\text{min}}^i = -\log \mathcal{L}^i(\boldsymbol{\beta}_{\text{min}}^i)$. Furthermore we evaluate the

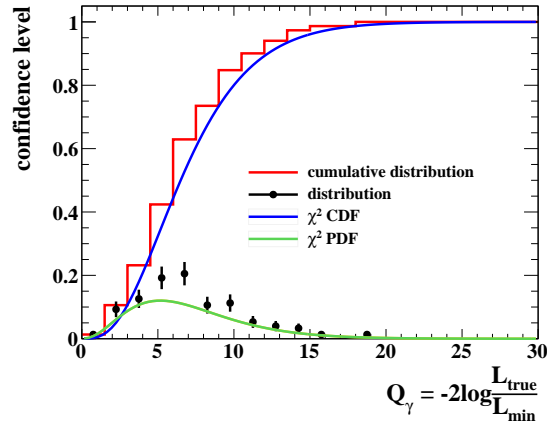


Figure 12.9: The quantity Q_i is distributed according to a χ^2 distribution. The fit yields 7.15 ± 0.28 degrees of freedom. This shows that the confidence levels are well covered.

likelihood at the position of the true parameters: $-\log \mathcal{L}_{true}^i = -\log \mathcal{L}^i(\beta_{true})$. For each sample we calculate

$$Q_i = -2 \log \frac{\mathcal{L}^i(\text{true})}{\mathcal{L}^i(\text{min})}. \quad (12.16)$$

Q_i is expected to be distributed according to eq. (12.17) and a fit to the Q_i distribution with the degrees-of-freedom as free parameter is supposed to yield the number of fit parameters. The distribution for the nominal model is shown in fig. 12.9 and the test shows that the confidence intervals are well covered.

Furthermore we check that no better minima exists in the parameter space. We do so by rerunning the minimization with random start values from the whole parameter space. From 150 fits, no fit with a valid minimum exhibits a smaller likelihood value than the nominal set of start parameters.

12.9 RESULT

We find that the Dalitz plot is well described by a model with 5 resonances. We include the $a_0(980)^0$, $\phi(1020)$, $a_0(980)^+$ and the $a_2(1320)^-$. The Dalitz plot projections and the fit model are shown in fig. 12.10 and the fit parameters are listed in table 12.12. A logarithmic representation can be found in fig. B.4.

The $a_2(1320)^-$ has a small fit fraction but a significance of 3.88σ as shown in table 12.8 and we therefore include it into our model. The significance of the final set of resonances versus the full set is 3.82σ but since the final model has a significantly smaller sum fit fraction it is preferred from the point of view of physical interpretability. The sum fit fraction is 166.8 % which comes from a strong destructive interference between the $a_0(980)^0$ and the $a_0(980)^+$ of about -71.09% .

The $a_0(980)^0$ and the $f_0(980)$ have the same mass and similar couplings. Our resonance selection procedure favors the $a_0(980)^0$ over the $f_0(980)$. The

Table 12.11: Overview of uncertainties for the nominal model. We list the fit parameters and its statistical and systematic uncertainties. The fit parameters and fit fractions are corrected for its fitting bias and are denoted by corrected value. Systematic uncertainties are given in units of the statistical uncertainty of the parameter. In case that errors are asymmetric we use the average value. A detailed overview is given in table B.3.

Parameter	g_{KK}	$a_0(980)^0$	$a_0(980)^+$			$\phi(1020)$			$a_2(1320)^-$		
	[GeV]	FF[%]	c	ϕ [rad]	FF[%]	c	ϕ [rad]	FF[%]	c	ϕ [rad]	FF[%]
Fit values	2.87	0.73	0.66	-2.93	0.32	0.81	1.76	0.48	0.10	0.24	0.008
Corrected values	2.88	0.73	0.66	-2.92	0.32	0.81	1.74	0.48	0.09	0.13	0.007
Background [$\bar{\sigma}$]	0.45	0.59	0.90	0.77	0.75	0.37	0.42	0.60	0.23	0.38	0.18
Model [$\bar{\sigma}$]	0.29	0.63	1.12	1.44	1.04	0.69	0.64	1.95	0.30	0.66	0.43
External [$\bar{\sigma}$]	1.93	0.77	1.45	1.15	1.62	0.57	2.60	0.21	0.95	0.28	0.99
Fitting [$\bar{\sigma}$]	0.03	0.04	0.01	0.00	0.05	0.01	0.19	0.04	0.20	0.21	0.16
Sys. uncertainty [$\bar{\sigma}$]	2.00	1.30	2.19	2.21	2.17	1.03	2.72	2.07	1.07	0.89	1.17
Sys. uncertainty	0.51	0.07	0.13	0.34	0.10	0.04	0.17	0.03	0.03	0.21	0.005
Mean stat. uncertainty $\bar{\sigma}$	0.25	0.06	0.06	0.15	0.05	0.04	0.06	0.02	0.03	0.24	0.004
Total uncertainty	0.56	0.09	0.14	0.37	0.11	0.05	0.18	0.04	0.04	0.32	0.006

present of the $a_0(980)^0$ is expected since its charged partner is seen in the $K_S^0 K^+$ channel. Nevertheless it is possible that some of the intensity added to the $a_0(980)^0$ originates from the $f_0(980)$. The study of another decay channel of $a_0(980)^0$ or $f_0(980)$ would be necessary to clearly distinguish both.

The coupling of the $a_0(980)$ to $K\bar{K}$ is a free parameter and we determine a value of $(2.88 \pm 0.25 \text{ (stat.)} \pm 0.56 \text{ (sys.)})$ GeV. At the *BABAR* experiment the coupling was measured in the same decay channel and a value of (3.29 ± 0.21) GeV [18] was obtained. A reanalysis using the full data set gives (3.90 ± 0.07) GeV [19]. An overview of other measurements is compiled in table 12.6. Those measurements yields an average value of (1.89 ± 0.06) GeV. Our measurement is in between those measurement and is compatible with all of them within its uncertainty. The uncertainty mainly originates from $a_0(980)$ mass.

The projections of the model and the data sample show that both models have a decent fit quality. For a quantitative measure of the goodness-of-fit we apply the ‘statistical energy’ test as described in section 12.5. The probability that the data sample is distributed according to our amplitude model is (42.6 ± 0.3) %.

The effect of the quantum entanglement between the tag D^0 decay and the signal decay as described in chapter 6 has only a minor influence. In fig. 12.10 the total intensity is shown in blue and the intensity due to the Cabibbo-favoured decay is shown in orange. The difference between both is due to the quantum entangled decay.

In general our results are systematically limited. The major source is the uncertainty on the $a_0(980)$ mass and its coupling to $\eta\pi$. The coupling to $\eta\pi$ to currently fixed to 2.66 GeV. As shown in table 12.6 the measurements for the coupling to $\eta\pi$ spread over a wide range.

Table 12.12: Result from the Dalitz plot analysis. The first uncertainty is statistical followed by systematic uncertainty. The coupling constant $a_0(980) \rightarrow K\bar{K}$ is determined to be $g_{K\bar{K}} = (2.88 \pm 0.25 \text{ (stat.)} \pm 0.56 \text{ (sys.)}) \text{ GeV}$. The model has a fit probability of $(42.6 \pm 0.3) \%$ and the statistical significance of the $a_2(1320)^-$ is 3.88σ .

Final state	Magnitude	Phase [rad]	Fit fraction [%]
$a_0(980)^0 K_s^0$	1	0	$73 \pm 6 \pm 7$
$a_0(980)^+ K^-$	$0.66 \pm 0.06 \pm 0.13$	$-2.92 \pm 0.15 \pm 0.34$	$32 \pm 5 \pm 10$
$\phi(1020) K_s^0$	$0.81 \pm 0.04 \pm 0.04$	$1.74 \pm 0.06 \pm 0.17$	$48 \pm 2 \pm 3$
$a_2(1320)^- K^+$	$0.09 \pm 0.03 \pm 0.03$	$0.13 \pm 0.24 \pm 0.21$	$0.7 \pm 0.4 \pm 0.5$
Total			154 ± 13

The amplitude model is used below in the branching fraction measurement to calculate the signal efficiency.

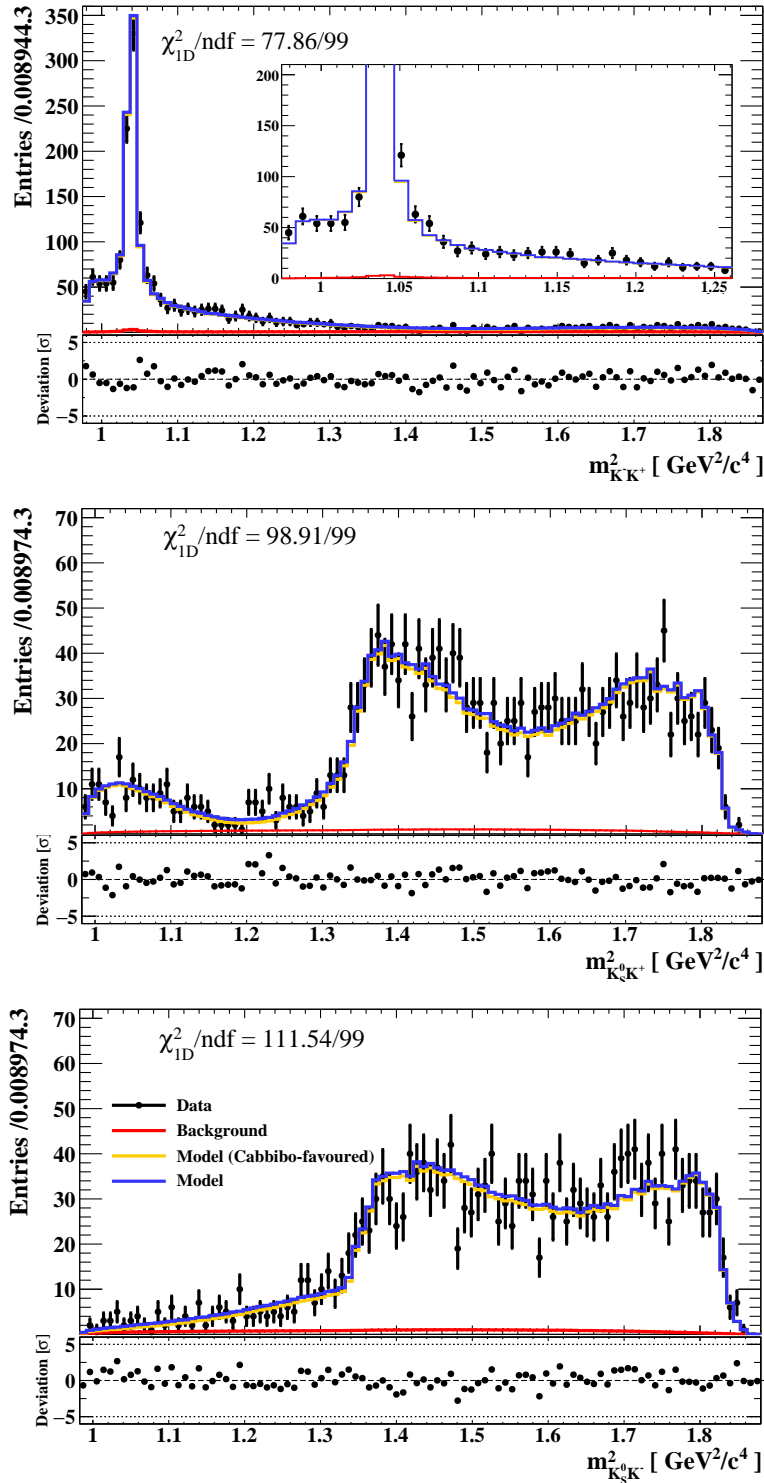


Figure 12.10: Dalitz plot projections of data sample and amplitude model. The Cabbibo-favoured component (orange), the background component (red) and the full amplitude (blue) are shown.

13

BRANCHING-FRACTION MEASUREMENT

The measurement of the branching fraction $D^0 \rightarrow K_s^0 K^+ K^-$ in quantum entangled $D^0 \bar{D}^0$ decays can be done in two ways, as explained in section 6.2. In a so-called **double-tag** measurement both D^0 mesons are reconstructed and the branching fraction is normalized to the number of inclusively reconstructed tag decays. This ratio has to be corrected for the effect of the entangled D^0 decays, as shown in eq. (6.22). Since the requirement that both D^0 mesons are reconstructed reduced statistics by about a factor of 6, we decide to perform a **single-tag** measurement. In that case the number of reconstructed signal decays N_{sig} is normalized to the total number of $D^0 \bar{D}^0$ decays $N_{D\bar{D}}$. The branching fraction for an isolated D^0 decay is then given by:

$$\mathcal{B}_j = \frac{N_j}{N_{D\bar{D}} \underbrace{[1 + \langle r_j \rangle - y \langle 2\sqrt{r_j} \cos \delta_j \rangle]}_{f_{QC}} \times \epsilon_{BF}}. \quad (6.19)$$

The single-tag measurement is also influenced by the entanglement of D^0 and \bar{D}^0 . The corresponding correction factor is denoted by f_{QC} . The simulated signal reconstruction efficiency is denoted by ϵ_{BF} and $N_{D\bar{D}}$ is calculated from the luminosity of the data sample \mathcal{L}_{data} and the cross section $\sigma_{D^0 \bar{D}^0}$ for the production of $D^0 \bar{D}^0$ at $\sqrt{s} = 3.773$ GeV in $e^+ e^-$ collisions. The K_s^0 is reconstructed in $\pi^+ \pi^-$ decays and we need to correct our result for its decay to other final states. The branching fraction for the decay $D^0 \rightarrow K_s^0 K^+ K^-$ then given by:

$$\mathcal{B}(D^0 \rightarrow K_s^0 K^+ K^-) = \frac{N^{\text{sig}}}{f_{QC} \cdot \epsilon_{BF} \cdot \mathcal{B}(K_s^0 \rightarrow \pi^+ \pi^-) \cdot (2 \times \mathcal{L}_{data} \cdot \sigma_{D^0 \bar{D}^0})}. \quad (13.1)$$

An overview of the parameters is given in table 13.1.

The correction factor for the quantum entangled $D^0 \bar{D}^0$ decays is calculated in section 13.1 from the Dalitz amplitude model. The signal yield on data is determined on data by a two-dimensional fitting procedure as described in section 11.6 and section 13.2. The reconstruction and selection efficiency for $D^0 \rightarrow K_s^0 K^+ K^-$ is shown in section 13.3 and we validate the branching fraction measurement in in section 13.4. Finally we study systematic uncertainties in section 13.5.

Table 13.1: Parameters for the branching fraction measurement. The number of D^0 decays on data is calculated from the cross section $e^+e^- \rightarrow D^0\bar{D}^0$ and the luminosity of the data sample. The signal Monte-Carlo sample is scaled to resemble the correct branching fraction.

Parameter	Simulation	Data	Reference
Luminosity		$(2931.8 \pm 13.8) \text{ pb}^{-1}$	[69, 94]
$\sigma(e^+e^- \rightarrow D^0\bar{D}^0)$		$(3.66 \pm 0.07) \text{ nb}$	[95]
Number of D^0 decays	21.46×10^6	$(21.46 \pm 0.41) \times 10^6$	
$\mathcal{B}(K_s^0 \rightarrow \pi^+ \pi^-)$	0.686	0.6920 ± 0.0005	[7]
$\mathcal{B}(D^0 \rightarrow K_s^0 K^+ K^-)$	3.079×10^{-3} 4.47×10^{-3} <i>scaling</i>		
Quantum entanglement correction f_{QC}	2	2.07 ± 0.03	section 13.1
Signal yield	$11\,384 \pm 115$	$11\,660 \pm 118$	section 13.2
Efficiency		(0.1704 ± 0.0004)	section 13.3

13.1 CORRECTION FOR QUANTUM ENTANGLED $D^0\bar{D}^0$ DECAYS

We want to obtain the branching fraction of an isolated D^0 decay. We have to correct the branching fraction from entangled $D^0\bar{D}^0$ decays by the factor

$$f_{QC} = 1 + \langle r_j \rangle - y \langle 2\sqrt{r_j} \cos \delta_j \rangle. \quad (13.2)$$

This factor can be calculated from the Dalitz amplitude model shown in fig. 12.10. The quantities r_j and δ_j depend on the phase-space position. For the calculation of f_{QC} we use average values which are calculated according to eq. (6.13). We use a signal Monte-Carlo sample with 2×10^6 events to evaluate the integrals and obtain:

$$f_{QC} = 2.07 \pm 0.03. \quad (13.3)$$

The statistical uncertainty of the Dalitz amplitude model is propagated to f_{QC} . We use the covariance matrix of the Dalitz amplitude model and generate several sets of model parameters. For each set we calculate f_{QC} . The distribution is shown in fig. 13.1 and we use its root-mean-square as uncertainty on f_{QC} . The limited statistics in the double-tagged Dalitz plot analysis causes a large uncertainty on f_{QC} of 1.4%. The Monte-Carlo sample does not include the quantum entanglement of $D^0\bar{D}^0$, in that case f_{QC} is exactly 2.

13.2 SIGNAL YIELD

The signal yield is determined using models for signal, combinatorial and non- K_s^0 background. Details are given in section 11.6. Since we see small differences

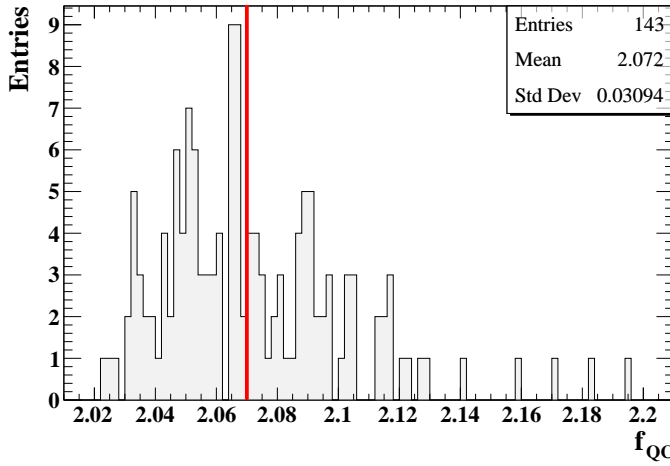


Figure 13.1: The distribution of the correction factor f_{QC} . Various sets of model parameters which were generated using the covariance matrix of the Dalitz amplitude model are used to estimate the uncertainty on f_{QC} .

Table 13.2: Signal and background yields for data and Monte-Carlo sample. The K_s^0 mass and width parameters are left free in the fit.

Parameter	Data	Simulation		
		Fit	True	Dev[σ]
Signal	$11\,660 \pm 118$	$11\,384 \pm 115$	11 298	0.75
Comb. background	1544 ± 66	3840 ± 75	3890	0.67
non- K_s^0 background	3 ± 131	0 ± 8	54	6.75
K_s^0 mass [MeV/ c^2]	497.73 ± 0.03	497.87 ± 0.02		
K_s^0 width [MeV]	2.29 ± 0.03	2.03 ± 0.02		

between data and simulation in the K_s^0 mass and width we leave these parameters free in the fit. This improves the fit quality notably. The fit results are listed in table 13.2 and the projections of sample and model to m_{BC} and m_{KS} are shown in fig. 13.3 for simulation and in fig. 13.6 for data. The fit to data yields a reduced χ^2 of 1.51 and 0.92 for the m_{BC} and m_{KS} distribution, respectively. Table 13.2 shows that the yield of the non- K_s^0 background component cannot be reproduced accurately. But since the yield is low the influence of the final result is small as we show in section 13.4.

13.3 EFFICIENCY CORRECTION

The efficiency for the branching fraction measurement is determined in simulation. The efficiency depends on the simulation of the decay substructure and therefore we use the Dalitz amplitude model to generate an accurate sig-

nal sample and use this sample for the efficiency calculation. We define the efficiency as:

$$\epsilon_{BF} = \frac{N^{\text{rec}}}{N_{\text{generated}}}. \quad (13.4)$$

$N_{\text{generated}}$ is the number of events with the final state $\pi^+\pi^-K^+K^-$ and an intermediate K_S^0 on generator level and N^{rec} is the number of correct reconstructed decays. Since even in a signal event the signal can be wrongly reconstructed we have to deal with background. By analogy to the determination of the signal yields in section 13.2 we determine the number of correct reconstructed signal events by a fitting procedure in m_{BC} and m_{KS} . Furthermore this has the advantage that a potential bias would influence the signal yield and the efficiency. In the ratio, given in eq. (13.1), such an effect would cancel.

The fit result can be biased by the level of background. Therefore, we use the full Monte-Carlo sample, including background. The projections of the sample and the fit model are shown in fig. 13.2. On generator level the Monte-Carlo

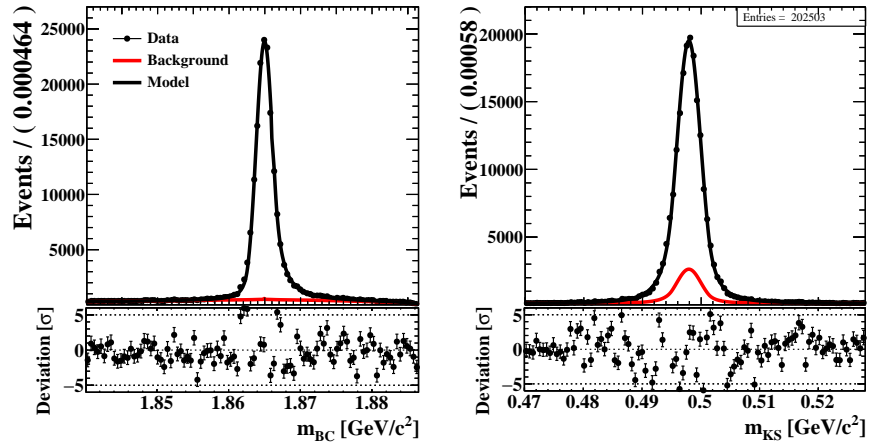


Figure 13.2: Efficiency determination using the full Monte-Carlo sample. The signal events in the sample were substituted with events that were generated according to the Dalitz amplitude model.

sample contains 979 229 signal decays. We determine $166\,880 \pm 438$ reconstructed signal events and the efficiency is:

$$\epsilon_{BF} = (17.04 \pm 0.04) \% \quad (13.5)$$

The uncertainty is statistical only.

13.4 VALIDATION

We validate our measurement procedure by applying the same fitting procedure that is used on data to the Monte-Carlo sample. From the full Monte-Carlo sample we select a subsample with the same luminosity as the data sample. This sample is corrected for the inaccurate branching fraction in the Monte-Carlo

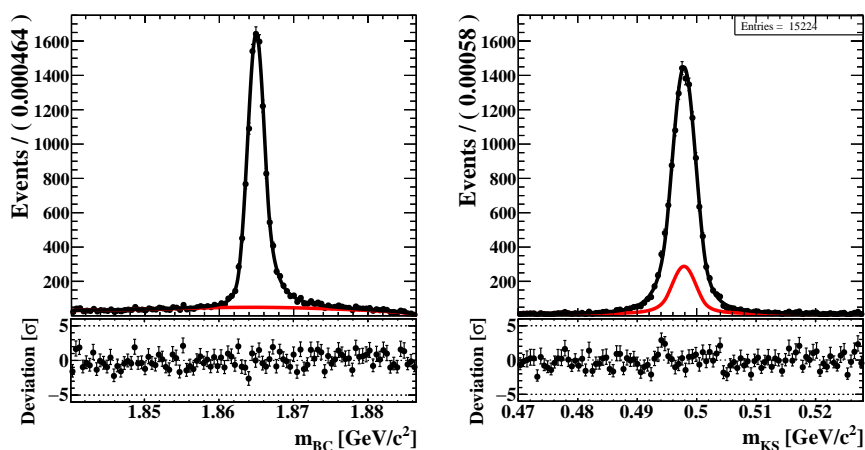


Figure 13.3: Signal yield on a (reduced) Monte-Carlo sample.

simulation. The expected outcome is the current PDG value of 4.47×10^{-3} . The projection of the sample and the fit model are shown in fig. 13.3 and the parameters are listed in table 13.2. The reduced χ^2 is 1.21 and 1.23 for the m_{BC} and m_{KS} distribution, respectively.

We obtain a signal yield of 11461 ± 115 and according to eq. (13.1) the branching fraction is:

$$\mathcal{B}_{MC}(D^0 \rightarrow K_s^0 K^+ K^-) = (4.540 \pm 0.045 \text{ (stat.)} \pm 0.014 \text{ (sys.)}) \times 10^{-3}. \quad (13.6)$$

The relative accuracy is 1.1%. The systematic uncertainty quoted here is the statistical error of the efficiency determination. All other sources of systematic uncertainties are due to differences between data and Monte-Carlo simulation and are therefore not present in this case. The deviation to the true value is 1.40σ .

13.5 STUDY OF SYSTEMATIC UNCERTAINTIES

13.5.1 Mass resolution

We see differences in the K_s^0 mass distribution between data and simulation. The K_s^0 mass and width are free parameters in the fit. We obtain a difference of (140 ± 32) keV and (259 ± 35) keV for the K_s^0 mass and width, respectively. We do not assign any further uncertainty. The width for the m_{BC} distribution is 1.16 MeV for the Monte-Carlo sample and we cannot see a difference to data.

13.5.2 Substructure of $K_s^0 K^+ K^-$

The total reconstruction and selection efficiency is determined using Monte-Carlo simulation and it depends on a correct simulation of the substructure of the decay. We determine the efficiency on a sample which contains signal events that decay according to the Dalitz amplitude model that was determined

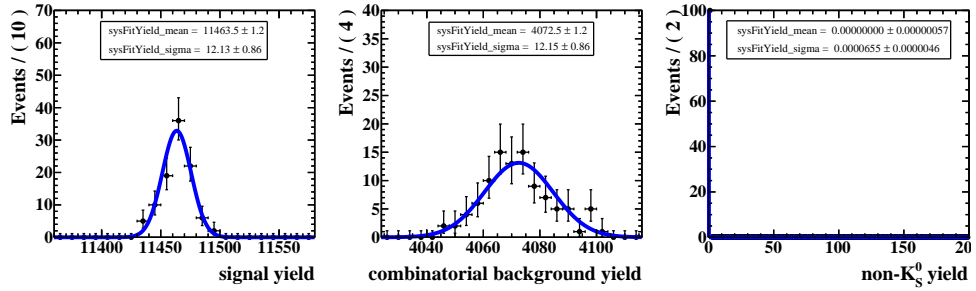


Figure 13.4: Uncertainties for the signal and background yield due to variations in the PDF description. The width of the distribution is taken as systematic uncertainty.

in chapter 12. Since the Dalitz plot is well described, as shown in fig. 12.10, we consider this source of uncertainty to be negligible.

13.5.3 Signal and background models

The shape of signal and background models is determined using Monte-Carlo simulation. Discrepancies between data and simulation can therefore lead to a bias in the yield determination. In the fit to data the K_s^0 width is left free to take into account different resolutions. To estimate how the yield depends on the exact shape of the model we vary all shape parameters according to their uncertainties and recalculate the yields using statistically independent Monte-Carlo samples. We use the covariance matrix of the fit and a multi-dimensional Gaussian to generate sets of shape parameters and recalculate signal and background yields using these sets of parameters. The width of the signal yield distribution is taken as systematic error. The distribution with a Gaussian fit is shown in fig. 13.4. We assume that the systematic uncertainty due to discrepancies between PDF model and data is less than 0.2 %.

13.5.4 Selection variables

Deviations between data and simulation can lead to different resolutions in specific variables. Therefore, selection requirements can have different efficiencies in data and simulation. This in turn leads to differences in the signal yields for data and simulation which influences the branching fraction. We therefore vary the selection variables and determine the simulated yields for each variation. We choose a value below and above of the nominal value. The range that we use here is a conservative assumption on what the difference between data and simulation could be. Since we are using mostly standard selection criteria most uncertainties on the selection variables are already included in the systematic uncertainties of track reconstruction and particle identification for K_s^0 and K^\pm . The χ^2 of the D^0 kinematic fit is the only variable that remains. We recalculate the simulated yield for values ± 2 of the nominal value and use the maximum

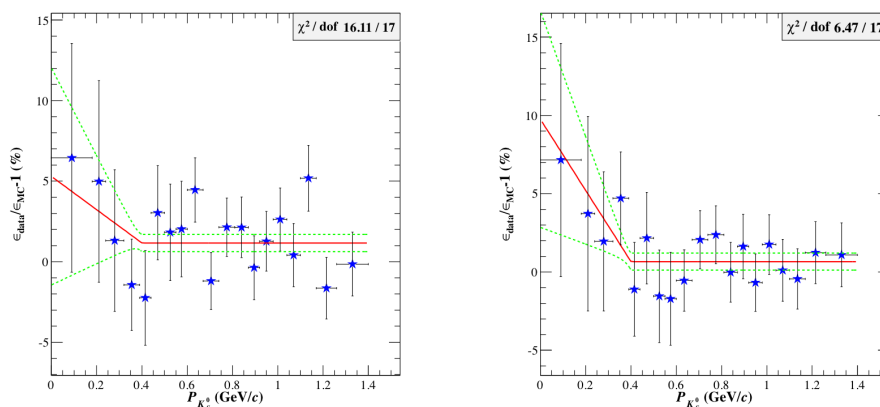


Figure 13.5: Efficiency difference of $K^0 \rightarrow K_S^0$ (left) and $\bar{K}^0 \rightarrow K_S^0$ (right) between data and simulation [96].

relative deviation as systematic uncertainty of our selection. The change in the yield is less than 0.8 %.

13.5.5 K_S^0 reconstruction efficiency

The systematic uncertainty of the K_S^0 reconstruction efficiency was studied in detail using $J/\psi \rightarrow K^{*\pm}K^\pm$ and $J/\psi \rightarrow \phi K_S^0 K^\mp \pi^\pm$ control samples and is provided by the collaboration [96]. The agreement between data and simulation is $(1.01 \pm 0.53) \%$, when we average over \bar{K}^0 and K^0 . The discrepancy in efficiency between data and simulation has a momentum dependence, as shown in fig. 13.5. We can take this into account by calculating the momentum weighted average and we obtain $(1.05 \pm 0.05) \%$ (see table 13.3). We take a conservative value of 1.5 % as systematic uncertainty.

13.5.6 Track reconstruction and particle identification

Charged tracks are selected using criteria which are consensus in the collaboration. Many studies had been performed and show that the difference of tracking efficiencies for data and simulation is less than 1 %. We use this as the systematic uncertainty of the track reconstruction efficiency for each charged kaon track.

Furthermore the simulation of the particle identification corresponds to data generally on a level of 1 %. The comparison with the momentum weighted difference between data and simulation in table 13.3 shows that this is a conservative assumption. We add 1 % systematic uncertainty for each charged kaon track due to particle identification (the K_S^0 daughter tracks have no requirements on the particle ID).

Table 13.3: Momentum weighted efficiency difference between data and simulation. The dependence of the efficiency difference on the particle momentum is listed in table B.3a. We use a conservative assumption as systematic uncertainty since studies were performed using a previous software version than is used for this analysis (6.6.4.p02). All studies are provided by the collaboration.

$\left(\frac{\epsilon_{data}}{\epsilon_{mc}} - 1\right)$ [%]	Software version	Weighted average	Arithmetic average	We use
K_s^0 reconstruction [96]	6.6.4.p02	0.97 ± 0.03	1.13	1.5
K^+K^- reconstruction [97]	6.6.2	0.207 ± 0.002	0.86	2
K^+K^- PID [97]	6.6.2	-0.2073 ± 0.0003	-0.54	2
K^+K^- PID	6.6.4.p02	0.616	0.62	2

13.5.7 Overview of systematic uncertainties

An overview over all contributions to the systematic uncertainty of the measurement is given in table 13.4. The systematic uncertainty, and also the total uncertainty, of the measurement is dominated by the contributions due to track reconstruction and particle identification. Furthermore the cross section measurement is a significant contribution.

13.6 RESULT

The signal yield on data is determined by a two-dimensional fitting procedure. The projections to m_{BC} and m_{KS} of the data sample and the fit model are shown in fig. 13.6 and we obtain a signal yield of:

$$N^{\text{sig}} = 11\,660 \pm 118. \quad (13.7)$$

Details on the fit result as well as the correlation matrix can be found in appendix B.7 and table B.8.

Our final result for the branching fraction of $D^0 \rightarrow K_s^0 K^+ K^-$ is according to eq. (13.1):

$$\mathcal{B}(D^0 \rightarrow K_s^0 K^+ K^-) = (4.45 \pm 0.05 \text{ (stat.)} \pm 0.18 \text{ (sys.)}) \times 10^{-3}. \quad (13.8)$$

The relative statistical and systematical uncertainties are 1.1 % and 4.08 %, respectively, which give a total uncertainty of 4.21 %. Our result is in good agreement with the current best measurement of $(4.47 \pm 0.34) \times 10^{-3}$ [7]. The deviation is 0.1σ . We are able to improve the precision of the branching fraction $D^0 \rightarrow K_s^0 K^+ K^-$ significantly.

Table 13.4: Overview of systematic uncertainties.

Systematic uncertainties [%]	
Signal/background model	0.20
Selection	0.80
Quantum entanglement	1.45
Efficiency	
Statistics	0.22
K^\pm particle identification	2.00
K^\pm tracking	2.00
K_S^0 reconstruction	1.50
External	
Luminosity measurement	0.47
cross section $e^+e^- \rightarrow D^0\bar{D}^0$	1.83
$\mathcal{B}(K_S^0 \rightarrow \pi^+ \pi^-)$	0.07
Total	4.08

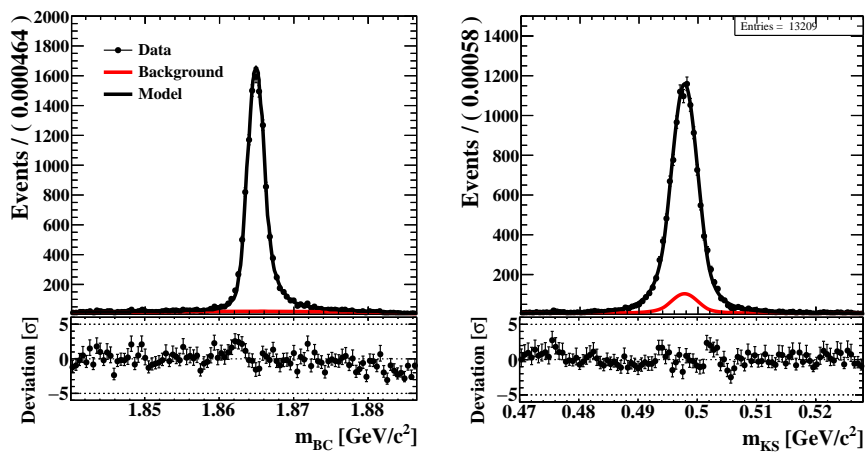


Figure 13.6: Projections of the data sample and the fit model.

Part V

SUMMARY AND OUTLOOK

SUMMARY AND OUTLOOK

The BESIII experiment analyzes e^+e^- collisions in an energy range between 2.0 GeV and 4.6 GeV. At a center-of-mass energy of $\sqrt{s}=3.773$ GeV the production threshold for $D^0\bar{D}^0$ and D^+D^- is located. At this energy BESIII has reached a luminosity record of $1 \times 10^{33} \text{ cm}^{-2} \text{ s}^{-1}$ and has collected a large sample of 2931.8 pb^{-1} . This corresponds to about 10.7×10^6 $D^0\bar{D}^0$ decays and 8.5×10^6 D^+D^- decays. The at-threshold decay topology provides a good laboratory to study D decays in a clean environment. As both, an advantage and a complication, the $D^0\bar{D}^0$ meson pair is produced in a quantum entangled state that allows to conclude properties of one D^0 meson from the decay of the other meson. Depending on the decay channel of the second meson, this can be the particle flavour or the CP quantum number.

The topic of this thesis is the analysis of the decay $D^0 \rightarrow K_S^0 K^+ K^-$. In a first step the Dalitz plot is analyzed using an isobar amplitude model. We select the optimal set of resonances using a ‘penalty term’ method. We find that the Dalitz plot is well described using an amplitude with four resonant contributions, namely the $a_0(980)^0$, the $a_0(980)^+$, the $\phi(1020)$ and the $a_2(1320)^-$. The largest contribution to the total intensity comes from the $a_0(980)^0$ which described together with its charged partner the $K\bar{K}$ threshold. Both resonances show a strong interference which leads to a sum of fit fractions of the Dalitz amplitude model of $(154 \pm 13) \%$. The $f_0(980)$ influences this interference but our strategy for resonance selection does not favour a model that includes the $f_0(980)$. The $a_0(980)$ couples strongly to the channel $K\bar{K}$ as well as to the channel $\pi\eta$. We measure its coupling to $K\bar{K}$ to be $g_{K\bar{K}} = (2.88 \pm 0.25 \text{ (stat.)} \pm 0.56 \text{ (sys.)}) \text{ GeV}$. Within the uncertainty we are in agreement with previous measurements. The contribution from $a_2(1320)^-$ yields only $(0.09 \pm 0.03) \%$ yet its significance is 3.88σ . For the Dalitz plot analysis both D^0 mesons in each event are reconstructed. Therefore the sample size of limited and statistical and systematic uncertainties are of the same order. The result is influenced by the quantum entanglement of both D^0 meson with respect the measurements of isolated D^0 decays. We include this effect in our amplitude model. The measurement of the fit fractions is unfortunately not in agreement with the result from previous analysis performed at the *BABAR* experiment [18]. The reason for the deviation could not be established.

We use the Dalitz amplitude model to accurately describe the signal decay in Monte-Carlo simulation. This is necessary to determine the total reconstruction and selection efficiency of the decay. We measure a branching fraction of $(4.45 \pm 0.05 \text{ (stat.)} \pm 0.18 \text{ (sys.)}) \times 10^{-3}$. The measurement is in good agreement with previous measurements and we are able to reduce the uncertainty significantly. The measurement is systematically limited. An improved measurement of the cross section of $e^+e^- \rightarrow D^0\bar{D}^0$ from BESIII will be available soon and will reduce the systematic uncertainty. The correction factor of the quantum

entanglement of the $D^0\bar{D}^0$ is extracted from the Dalitz amplitude model and its statistical limitations are propagated to the systematic uncertainty of the branching fraction measurement.

The result from the Dalitz plot analysis and the branching fraction measurement are currently under review by the collaboration.

In a side project the reconstruction of displaced vertices was studied using $J/\psi \rightarrow \Lambda\bar{\Lambda}$ decays. No significant deviations between data and Monte-Carlo simulation is found. The results are provided to the BESIII collaboration [98]. As part of this study the branching fraction $J/\psi \rightarrow \Lambda\bar{\Lambda}$ is measured to be $(2.07 \pm 0.03 \text{ (stat.)} \pm 0.08 \text{ (sys.)}) \times 10^{-3}$. The result is in good agreement with previous measurements [99, 100] and we are able to reduce the uncertainty significantly.

The decay $D^0 \rightarrow K_s^0 K^+ K^-$ is of interest for the measurement of the CKM angle γ/ϕ_3 . The angle γ/ϕ_3 can be measured in the decay $B^- \rightarrow D^0 K^-$ using the so-called GGSZ method [19]. The D^0 needs to decay to a self-conjugate final state among which, the channels $K_s^0 \pi^+ \pi^-$ and $K_s^0 K^+ K^-$ are of special interest. The strong phase difference between D^0 and the \bar{D}^0 decay and its variation over the phase-space is an external input. We can extract it from our Dalitz amplitude model as shown in fig. 13.7. The phase difference depends strongly on the model and therefore the model uncertainty would be the limiting factor for the measurement of γ/ϕ_3 . The solution is a model independent measurement of the phase as it is currently performed for the channel $K_s^0 \pi^+ \pi^-$ at BESIII. For the channel $K_s^0 K^+ K^-$ a previous measurement of CLEO-c [17] exists but with its larger statistics, BESIII could reduce the uncertainty. Unfortunately this measurement is beyond this thesis.

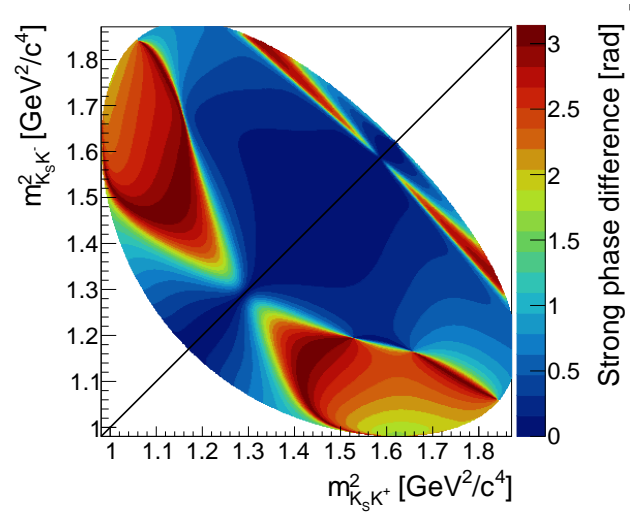


Figure 13.7: Absolute strong phase difference of D^0 and \bar{D}^0 amplitude.

Part VI

APPENDIX

A

THEORY

A.1 PROPERTIES OF THE WIGNER D-MATRIX

In the following we list some properties of the WignerD function. Derivations for the relations can be found in [27]. The Wigner-D matrix is connected to the (small) Wigner-D matrix via:

$$D_{m'm}^J(\alpha\beta\gamma) = e^{-im'\gamma} d_{m'm}^J(\beta) e^{-im\alpha}. \quad (\text{A.1})$$

The (small) Wigner-D matrix element is given by:

$$d_{m'm}^J(\beta) = \sum_n \frac{(-1)^n \sqrt{(J+m)!(J-m)!(J+m')!(J-m')!}}{(J-m'-n)!(J+m-n)!(n+m'-m)!n!} \\ \times (\cos \beta/2)^{2J+m-m'-2n} \times (-\sin \beta/2)^{m'-m+2n}. \quad (\text{A.2})$$

The sum goes over all n for which the factorials are positive. The Wigner-D matrix obeys the following relations:

1. $d_{m'm}^J(-\beta) = (-1)^{m'-m} d_{m'm}^J(\beta) = d_{mm'}^J(\beta)$
2. $D_{mm'}^J(0, \beta, 0) = D_{m'm}^J(0, -\beta, 0)$
3. $D_{mm'}^J(\alpha, \beta, \gamma) = D_{mm'}^J(\gamma, -\beta, \alpha)$
4. $d_{m'm}^J(\pi) = (-1)^{J-m} \delta_{m', -m}$
5. $D_{mm'}^J(0, 0, 0) = \delta_{mm'}$

The Wigner-D matrix elements are orthogonal

$$\int_0^{2\pi} d\alpha \int_0^{2\pi} d\gamma \int_0^\pi d\beta \sin \beta D_{mn}^{J*}(\alpha\beta\gamma) D_{m'n'}^J(\alpha\beta\gamma) \\ = \frac{8\pi^2}{2J+1} \delta_{mm'} \delta_{nn'} \delta_{JJ'}, \quad (\text{A.3})$$

and they are related to spherical harmonics via:

$$D_{m0}^J(\alpha\beta, 0) = \sqrt{\frac{4\pi}{2J+1}} Y_J^{m*}(\beta, \alpha) \\ = \sqrt{\frac{(J-m)!}{(J+m)!}} P_J^m(\cos \beta) e^{-im\alpha}. \quad (\text{A.4})$$

A.2 THE OPTICAL THEOREM

The optical theorem links the imaginary part of the forward scattering amplitude with the total cross section. We follow [21, Chapter 4.5]. Assuming a scattering process of two-particles in the initial state $|i\rangle$ and in the final state $|i\rangle$, we choose the z -axis as collision axis of the initial state ($\theta_i = \phi_i = 0$) and evaluate the final state in forward direction ($\theta_f = \phi_f = 0$). We remind about the unitarity relation for the transition operator:

$$T - T^\dagger = iT^\dagger T. \quad (4.17)$$

$$\begin{aligned} \langle f | T_{\mathcal{P}} | i \rangle - \langle f | T_{\mathcal{P}}^\dagger | i \rangle &= i \langle f | T^\dagger T | i \rangle \\ &= i \sum_n \langle f | T^\dagger | n \rangle \langle n | T | i \rangle. \end{aligned} \quad (A.5)$$

We have inserted a complete set of states in the right hand side of the matrix notation and we have separated the conserved four-momenta from the transition amplitude T . In the next step we replace them by two-particle plane wave states:

$$\begin{aligned} \langle 00, \lambda | T_{\mathcal{P}} | 00, \lambda \rangle - \langle 00, \lambda | T_{\mathcal{P}}^\dagger | 00, \lambda \rangle &= \\ &= i \sum_{\lambda'} \int d\theta' d\phi' \langle 00, \lambda | T^\dagger | \theta' \phi', \lambda' \rangle \langle \theta' \phi', \lambda' | T | 00, \lambda \rangle \\ \langle 00, \lambda | T_{\mathcal{P}} | 00, \lambda \rangle - \langle 00, \lambda | T_{\mathcal{P}} | 00, \lambda \rangle^* &= \\ &= i \sum_{\lambda'} \int d\theta' d\phi' |\langle \theta' \phi', \lambda' | T | 00, \lambda \rangle|^2 \\ 2i \operatorname{Im} \langle 00, \lambda | T_{\mathcal{P}} | 00, \lambda \rangle &= i \left(\frac{q}{2\pi} \right)^2 \sum_{\lambda'} \int d\theta' d\phi' \frac{d\sigma_{\lambda'}}{d\theta' d\phi'}. \end{aligned} \quad (A.6)$$

We have used that the cross section is linked to the amplitude intensity via [21, Equation 4.61]:

$$\frac{d\sigma}{d\theta d\phi} = \left(\frac{2\pi}{q} \right)^2 |\langle \theta \phi, \lambda_f | T_{\mathcal{P}} | 00, \lambda_i \rangle|^2. \quad (A.7)$$

The optical theorem can then be written as:

$$\operatorname{Im} T(s, t = 0) = \frac{q\sqrt{s}}{8\pi^2} \sigma_{tot}. \quad (4.18)$$

A.3 THE MIXING PARAMETER y

The D^0 mixing parameter y is defined as:

$$y = \frac{\Gamma_2 - \Gamma_1}{2\Gamma}. \quad (A.8)$$

The width of the CP eigenstates

$$|D_{1,2}\rangle = \frac{1}{\sqrt{2}} (|D^0\rangle \pm |\bar{D}^0\rangle) \quad (2.1)$$

are denoted by $\Gamma_{1,2}$ and the total D^0 width by Γ . We use eq. (2.1) and get:

$$\begin{aligned} 2y &= \underbrace{\sum_j |\langle j|D_2\rangle|^2}_{\Gamma_2/\Gamma} - \underbrace{\sum_j |\langle j|D_1\rangle|^2}_{\Gamma_1/\Gamma} \\ 2y &= \sum_j (|\langle j|D^0\rangle - \langle j|\bar{D}^0\rangle|^2 - |\langle j|D^0\rangle + \langle j|\bar{D}^0\rangle|^2) \\ 2y &= \sum_j (|\mathcal{A}_j - \bar{\mathcal{A}}_j|^2 - |\mathcal{A}_j + \bar{\mathcal{A}}_j|^2) \\ 2y &= 2 \sum_j (-\mathcal{A}_j^* \bar{\mathcal{A}}_j - \mathcal{A}_j \bar{\mathcal{A}}_j^*) \\ y &= \sum_j (\bar{\mathcal{A}}_j^* \sqrt{r_j} e^{i\delta_j} \bar{\mathcal{A}}_j + \bar{\mathcal{A}}_j \sqrt{r_j} e^{-i\delta_j} \bar{\mathcal{A}}_j^*). \end{aligned} \quad (A.9)$$

Finally we find the relation:

$$y = \sum_j |\bar{\mathcal{A}}_j|^2 \sqrt{r_j} 2 \cos \delta_j. \quad (A.10)$$

B

ANALYSIS OF $D^0 \rightarrow K_S^0 K^+ K^-$

B.1 SIGNAL AND BACKGROUND MODELS

The models for signal and background distributions of m_{BC} and m_{KS} are given in table B.1. The two-dimensional model is built from the one-dimensional model by multiplication:

$$F(m_{BC}, m_{KS}) = f(m_{BC}) \times g(m_{KS}). \quad (\text{B.1})$$

The Crystal-Ball function[101] is a Gaussian function with a power-law tail on one side. We add a second tail to the original description and denote it by CB2:

$$CB2(x) \sim \begin{cases} \left(\frac{n_L}{|\alpha_L|}\right)^{n_L} \exp\left(-\frac{|\alpha_L|^2}{2}\right) \left(\frac{n_L}{|\alpha_L|} - |\alpha_L| - x\right)^{-n_L}, & \text{if } x < \alpha_L \\ \exp\left(-\frac{x^2}{2}\right), & \text{if } \alpha_L < x < \alpha_R \\ \left(\frac{n_R}{|\alpha_R|}\right)^{n_R} \exp\left(-\frac{|\alpha_R|^2}{2}\right) \left(\frac{n_R}{|\alpha_R|} - |\alpha_R| + x\right)^{-n_R}, & \text{if } x > \alpha_R \end{cases} \quad (\text{B.2})$$

The mass dependence is expressed as the deviation from the mean value in units of the width: $x = (m - \mu)/\sigma$. $CB2(x)$ is a differentiable function with a Gaussian central part and power-law tails starting from $\alpha_{R/L}$ (in units of σ) on both sides. $n_{R/L}$ is the exponent of the power-law tails.

B.2 TAGGED SIGNAL FRACTION FOR THE DALITZ PLOT ANALYSIS

The signal and background yields are determined by a two-dimensional fit in m_{KS} and m_{BC} . The signal and background models are described in section 11.6 and appendix B.1. The fit to the tagged sample is shown in fig. B.1. For the Dalitz plot analysis we apply a signal region of 8σ . The signal fraction in the signal region is now calculated by integration of signal and background models in the corresponding region. The statistical uncertainty is propagated through the integral. Yields and signal fraction for data and simulation are compared in table 12.3.

Table B.1: PDF description for signal and background. The modified Crystal-ball function $CB2$ is defined in eq. (B.2), $P^{(1)}$ denotes a polynomial of first order with slope parameter s_X and $G(\mu, \sigma)$ is a Gaussian function. All functions are probability density functions and are therefore implicitly normalized. We omit the mass dependence of the functions.

$f(m_{BC})$	
signal	$CB2(\alpha_L, n_L, \mu, \sigma, \alpha_R, n_R)$
comb	$f_{comb}^{BC} \text{argus}(E_{\text{beam}}, p_{\text{argus}}) + (1 - f_{comb}^{BC})G(\mu_{comb}, \sigma_{comb})$
non- K_S^0	$f_{nonK_S^0}^{BC} CB2(\alpha_L, n_L, \mu, \sigma, \alpha_R, n_R) + (1 - f_{nonK_S^0}^{BC})\text{argus}(E_{\text{beam}}, p_{\text{argus}})$
$g(m_{KS})$	
signal	$CB2(\alpha_L, n_L, \mu, \sigma, \alpha_R, n_R)$
comb	$f_{comb}^{ks} P^{(1)}(s_{comb}) + (1 - f_{comb}^{KS})CB2(\alpha_L, \dots)$
non- K_S^0	$f_{nonK_S^0}^{ks} P^{(1)}(s_{nonK_S^0}) + (1 - f_{nonK_S^0}^{KS})CB2(\alpha_L, \dots)$

B.3 STATISTICAL UNCERTAINTY OF FIT FRACTIONS

The fit fractions for each intermediate resonance are calculated according to eq. (12.3). The normalization depends on all fit parameters and we have to propagate the covariance matrix through the integral. We choose a Monte-Carlo approach. The central values of the fit parameters are denoted by $\bar{\beta}$ and the covariance matrix by $\Sigma_{\bar{\beta}}$. Sets of fit parameters are generated using a multi-variate Gaussian

$$G(\mathbf{x}, \bar{\beta}, \Sigma_{\bar{\beta}}) \propto \exp\left(-\frac{1}{2}(\mathbf{x} - \bar{\beta})^T \Sigma_{\bar{\beta}}^{-1}(\mathbf{x} - \bar{\beta})\right), \quad (\text{B.3})$$

and we calculate the fit fractions for each set of parameters. The statistical uncertainty for each fit fractions is then given by the root-mean-square of the distribution. The distribution for the $a_0(980)^0$ fit fraction is shown in fig. B.2.

B.4 EFFICIENCY DIFFERENCES BETWEEN DATA AND SIMULATION

Differences between data and simulation in track reconstruction and particle-identification can influence the result of the Dalitz plot analysis. Especially the regions with low K^\pm tracks are prone to inaccuracies. We use the results provided by the collaboration [96, 97]. The momentum dependence of the efficiency difference for the reconstruction of charged kaons is listed in table B.3a and for particle identification in table B.3b. Both were determined using BOSS 6.6.2 [97]. Since we use a different version we have to study carefully how the result is influence. The reconstruction of the K_S^0 is studied in [96] and the results is shown in table B.3c and fig. 13.5. The study was performed with the same BOSS version but the requirement on the flight distance significance was

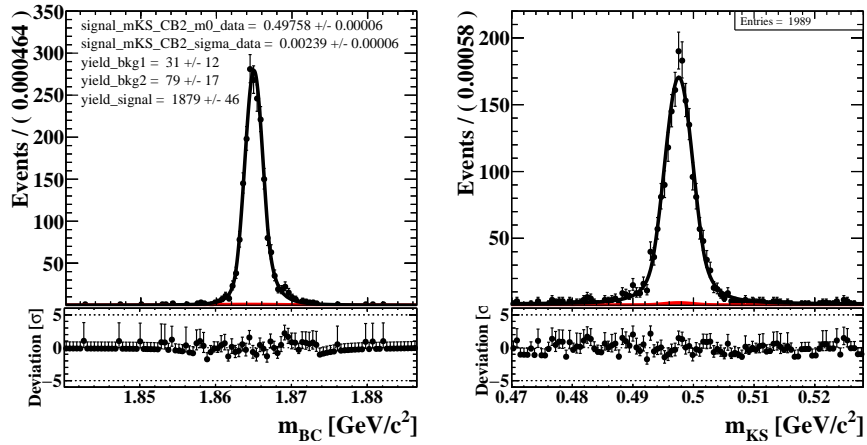


Figure B.1: Projections of data sample and fit model. From the fitted yields we calculate a signal purity of 96.37 %.

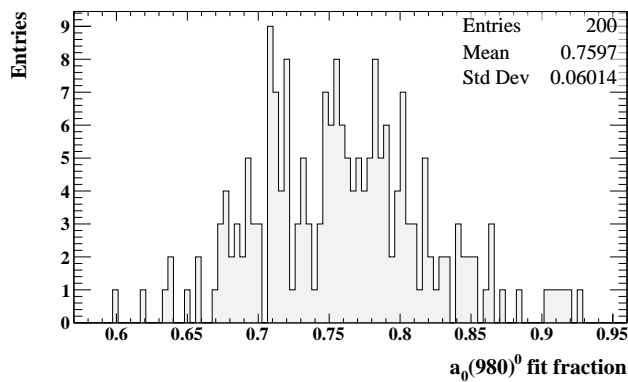


Figure B.2: Statistical variation of the $a_0(980)^0$ fit fraction. The statistical uncertainty of the fit fractions is estimated via Monte-Carlo simulation.

Table B.2: Relative efficiency difference between data and simulation in momentum bins. Note that the efficiency studies for charged kaons were performed using BOSS 6.6.2.

P[GeV/c] K^\pm		P[GeV/c] K^\pm		P[GeV/c]	K_S^0	$\overline{K_S^0}$
0.0 - 0.1	0.36	-	-	0 - 0.18	0.0645	0.0715
0.1 - 0.2	-0.007	0.1 - 0.2	-0.0263	0.18 - 0.24	0.0498	0.0372
0.2 - 0.3	0.0056	0.2 - 0.3	-0.0038	0.24 - 0.32	0.0131	0.0195
0.3 - 0.4	0.01	0.3 - 0.4	-0.0021	0.32 - 0.39	-0.0143	0.047
0.4 - 0.5	0.0177	0.4 - 0.5	-0.0017	0.39 - 0.44	-0.0224	-0.0111
0.5 - 0.6	0.0121	0.5 - 0.6	-0.002	0.44 - 0.5	0.0303	0.0216
0.6 - 0.7	0.0089	0.6 - 0.7	0.0008	0.5 - 0.55	0.0182	-0.0155
0.7 - 0.8	0.005	0.7 - 0.8	0.0046	0.55 - 0.6	0.0203	-0.0172
0.8 - 0.9	0.0053	0.8 - 0.9	0.0082	0.6 - 0.67	0.0445	-0.0055
0.9 - 1	0.0009	0.9 - 1	0.0028	0.67 - 0.74	-0.0119	0.0205
1 - 1.1	-0.0079	1 - 1.1	0.0071	0.74 - 0.81	0.0214	0.0237
				0.81 - 0.87	0.0213	-0.0002
				0.87 - 0.92	-0.0037	0.0163
				0.92 - 0.98	0.0127	-0.0068
				0.98 - 1.04	0.0262	0.0175
				1.04 - 1.1	0.0041	0.001
				1.1 - 1.17	0.0518	-0.0045
				1.17 - 1.26	-0.0164	0.0123
				1.26 - 1.4	-0.0015	0.0109

(a) Charged kaon tracking efficiency[97]

(b) Charged kaon PID efficiency[97]

(c) K_S^0 reconstruction efficiency[96]. Visualized in fig. 13.5.

chosen to be larger 2. In our analysis we select events with a flight distance significance larger 0.

The likelihood normalization is calculated using a phase-space sample that includes detector simulation, reconstruction and selection. The simulated efficiency is therefore intrinsically applied. We correct this sample for the efficiency difference between data and simulation by assigning per-event weights depending on the particle momenta of K^\pm and K_S^0 :

$$w(p_{K^-}, p_{K^+}, p_{K^0}) = \left(\frac{\epsilon_{data}(p_{K^-})}{\epsilon_{mc}(p_{K^-})} \right)_{K^-} \times \left(\frac{\epsilon_{data}(p_{K^+})}{\epsilon_{mc}(p_{K^+})} \right)_{K^+} \times \left(\frac{\epsilon_{data}(p_{K^0})}{\epsilon_{mc}(p_{K^0})} \right)_{K^0}. \quad (\text{B.4})$$

The influence of the efficiency correction on the result of the Dalitz plot analysis is found to be negligible. We do not assign a systematic uncertainty.

B.5 SYSTEMATIC UNCERTAINTIES OF THE DALITZ PLOT ANALYSIS

Input/Output check

We validate the analysis procedure by fitting the Dalitz amplitude model to a set of statistically independent Monte-Carlo samples. For each sample we calculate from the fit result:

$$\mathcal{P}_\beta = \frac{\beta_{\text{true}} - \beta}{\sigma_\beta}. \quad (12.22)$$

Further details are given in section 12.8.5. The distribution of \mathcal{P}_β for each free parameter in the fit is shown in fig. B.3

Overview

A detailed overview of the systematic uncertainties of the Dalitz amplitude model can be found in table B.3.

B.6 DALITZ PLOT FIT RESULT

The interference term between two resonances of the Dalitz amplitude model are calculated, similar to eq. (12.3), by:

$$f_{ij} = \frac{|c_i|^2 \int d\boldsymbol{\beta} A_j A_i^*{}^2}{\int d\xi |\mathcal{M}(\xi)|}. \quad (B.5)$$

We list the interference terms in table B.4 without uncertainty since the covariance matrix of the Dalitz amplitude model was not propagated through the integral. We consider only interference terms of the Cabibbo-favoured amplitude component.

The projections of the Dalitz amplitude model and the data sample are shown in logarithmic scale in fig. B.4.

As a cross-check we fit an Dalitz amplitude model to the data sample which does not consider the quantum entanglement of $D^0\bar{D}^0$. The fit result is listed in table B.6. The difference to the model that includes the quantum entanglement in table 12.12 is notable.

B.7 UNTAGGED SIGNAL YIELD FOR BRANCHING FRACTION MEASUREMENT

The fit result for the shape parameters is shown in table B.7.

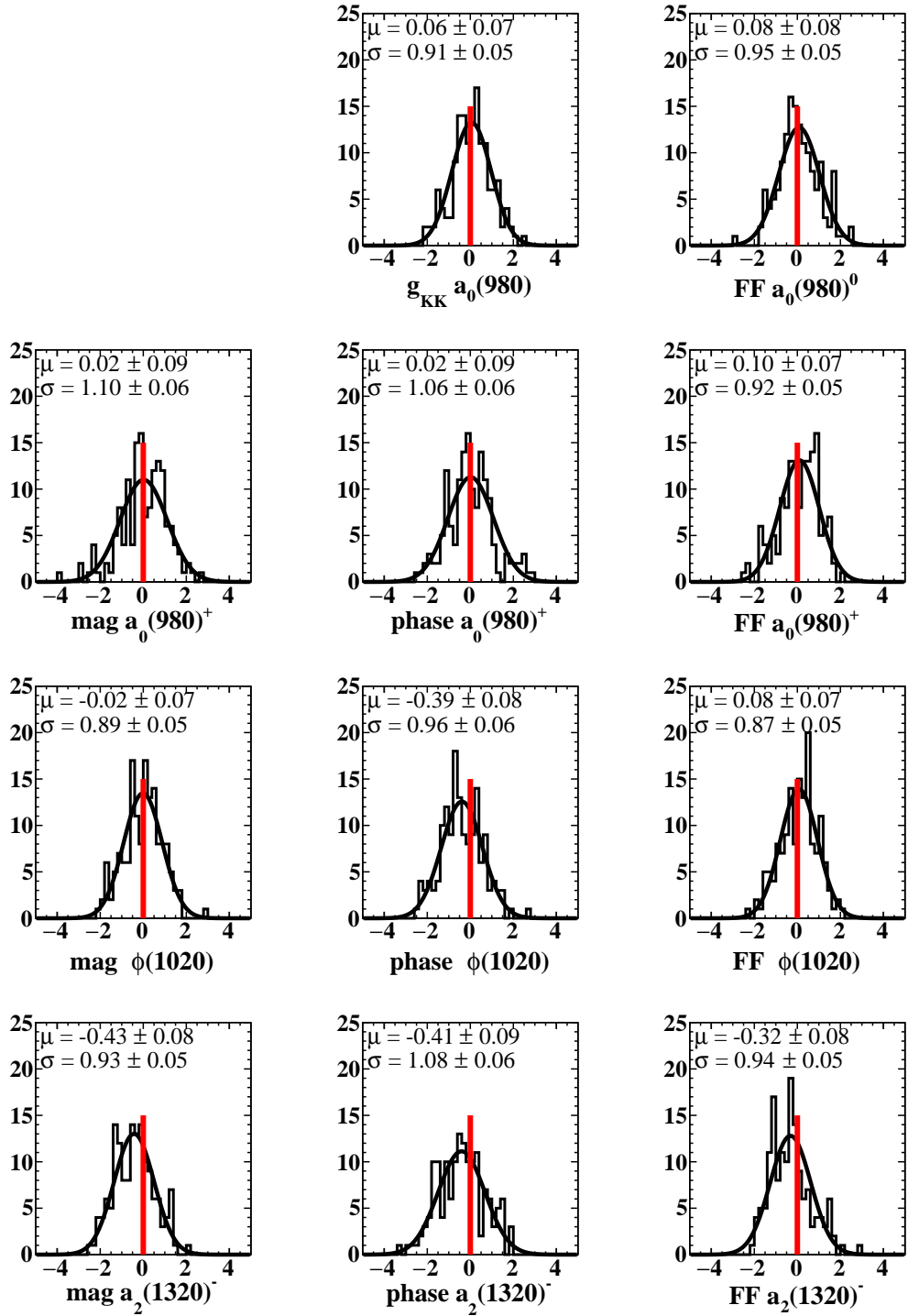


Figure B.3: Input/Output check for the Dalitz amplitude model. We fit 150 independent samples which have passed detector simulation, reconstruction and selection. The difference between the nominal fit and each fit result are given in units of the statistical uncertainty. An unbiased fit with correct error estimate yields a Gaussian distribution with mean 0 and width 1. For the final result we correct the parameters for the biases.

Table B.3: Detailed overview of systematic uncertainties for the Dalitz amplitude model. For further explanations see section 12.8.

Parameter	g_{KK} [GeV]	$a_0(980)^0$ FF[%]	$a_0(980)^+$			$\phi(1020)$			$a_2(1320)^-$			
			c	ϕ [rad]	FF[%]	c	ϕ [rad]	FF[%]	c	ϕ [rad]	FF[%]	
Nominal values	2.870	0.730	0.660	-2.930	0.320	0.810	1.760	0.480	0.100	0.240	0.008	
Stat.	σ^+	0.230	0.060	0.040	0.090	0.050	0.030	0.060	0.020	0.030	0.230	0.000
	σ^-	0.280	0.060	0.070	0.210	0.050	0.040	0.060	0.020	0.030	0.250	0.000
	Scale factor	1.000	1.000	1.000	1.000	1.000	1.000	1.000	1.000	1.000	1.000	1.000
	Mean $\bar{\sigma}$	0.250	0.060	0.060	0.150	0.050	0.040	0.060	0.020	0.030	0.240	0.000
Background	data sideband	2.900	0.720	0.680	-2.870	0.330	0.810	1.760	0.470	0.100	0.270	0.010
	MC sideband	2.960	0.700	0.700	-2.850	0.340	0.820	1.750	0.470	0.110	0.310	0.010
	fit fraction (high)	2.850	0.740	0.640	-2.970	0.310	0.810	1.780	0.480	0.100	0.250	0.010
	fit fraction (low)	2.920	0.710	0.690	-2.860	0.330	0.810	1.750	0.470	0.100	0.280	0.010
	Uncertainty [$\bar{\sigma}$]	0.450	0.590	0.900	0.770	0.750	0.370	0.420	0.600	0.230	0.380	0.180
Model	Meson radius 0 GeV ⁻¹	2.895	0.726	0.668	-2.911	0.324	0.808	1.753	0.474	0.102	0.193	0.008
	Meson radius 1 GeV ⁻¹	2.869	0.728	0.661	-2.927	0.318	0.808	1.764	0.475	0.104	0.237	0.008
	Meson radius 2 GeV ⁻¹	2.871	0.728	0.662	-2.926	0.319	0.808	1.764	0.475	0.104	0.234	0.008
	Meson radius 3 GeV ⁻¹	2.872	0.728	0.662	-2.925	0.319	0.808	1.762	0.475	0.104	0.227	0.008
	Meson radius 4 GeV ⁻¹	2.873	0.728	0.662	-2.924	0.319	0.808	1.761	0.475	0.104	0.218	0.008
	Meson radius 5 GeV ⁻¹	2.875	0.728	0.662	-2.923	0.319	0.808	1.760	0.475	0.104	0.209	0.008
	QC $\delta_{tag} = 0$	2.875	0.724	0.663	-2.920	0.318	0.812	1.791	0.477	0.106	0.232	0.008
	QC $\delta_{tag} \times 2$	2.872	0.725	0.662	-2.924	0.317	0.811	1.785	0.477	0.106	0.229	0.008
	QC $r_D(K^- \pi^+ \pi^0)$	2.877	0.731	0.675	-2.869	0.332	0.792	1.781	0.458	0.101	0.326	0.007
	QC $r_D \times 2$	2.849	0.740	0.618	-3.083	0.283	0.822	1.759	0.500	0.105	0.142	0.008
	$\Gamma_{\phi(1020)}$ free	2.806	0.761	0.615	-3.070	0.288	0.794	1.764	0.480	0.111	0.166	0.009
	Uncertainty [$\bar{\sigma}$]	0.290	0.630	1.120	1.440	1.040	0.690	0.640	1.950	0.300	0.660	0.430
	External	$g_{\eta\pi}$ free	2.846	0.718	0.656	-2.922	0.309	0.813	1.772	0.475	0.106	0.237
$M_{a_0(980)} \uparrow$		3.301	0.748	0.710	-2.919	0.377	0.800	1.629	0.478	0.080	0.256	0.005
$M_{a_0(980)} \downarrow$		2.645	0.766	0.594	-3.102	0.270	0.788	1.857	0.476	0.116	0.173	0.010
$M_{a_2(1320)} \uparrow$		2.870	0.728	0.662	-2.926	0.319	0.808	1.763	0.475	0.104	0.244	0.008
$M_{a_2(1320)} \downarrow$		2.870	0.729	0.661	-2.927	0.318	0.808	1.765	0.475	0.103	0.229	0.008
$\Gamma_{a_2(1320)} \uparrow$		2.867	0.729	0.660	-2.929	0.318	0.808	1.765	0.475	0.104	0.229	0.008
$\Gamma_{a_2(1320)} \downarrow$		2.872	0.728	0.662	-2.924	0.319	0.808	1.763	0.475	0.103	0.242	0.008
$M_{\phi(1020)} \uparrow$		2.875	0.729	0.662	-2.926	0.320	0.807	1.769	0.475	0.103	0.240	0.008
$M_{\phi(1020)} \downarrow$		2.865	0.728	0.661	-2.927	0.318	0.808	1.759	0.475	0.105	0.232	0.008
$\Gamma_{\phi(1020)} \uparrow$		2.868	0.729	0.660	-2.929	0.318	0.807	1.763	0.475	0.104	0.233	0.008
$\Gamma_{\phi(1020)} \downarrow$		2.871	0.728	0.662	-2.924	0.319	0.808	1.765	0.475	0.103	0.238	0.008
Uncertainty [$\bar{\sigma}$]	1.930	0.770	1.450	1.150	1.620	0.570	2.600	0.210	0.950	0.280	0.990	
Fitting	Bias [$\bar{\sigma}$]	0.058	0.081	0.017	0.016	0.100	-0.015	-0.391	0.076	-0.426	-0.407	-0.319
	Bias absolute	0.013	0.005	0.001	0.002	0.005	-0.001	-0.025	0.001	-0.011	-0.102	-0.001
	Uncertainty [$\bar{\sigma}$]	0.030	0.040	0.010	0.000	0.050	0.010	0.190	0.040	0.200	0.210	0.160
Corrected values	2.880	0.730	0.660	-2.920	0.320	0.810	1.740	0.480	0.090	0.130	0.007	
Mean stat. uncertainty $\bar{\sigma}$	0.250	0.060	0.060	0.150	0.050	0.040	0.060	0.020	0.030	0.240	0.000	
Sys. uncertainty [$\bar{\sigma}$]	2.000	1.300	2.190	2.210	2.170	1.030	2.720	2.070	1.070	0.890	1.170	
Sys. uncertainty	0.510	0.070	0.130	0.340	0.100	0.040	0.170	0.030	0.030	0.210	0.005	
Total uncertainty	0.560	0.090	0.140	0.370	0.110	0.050	0.180	0.040	0.040	0.320	0.006	

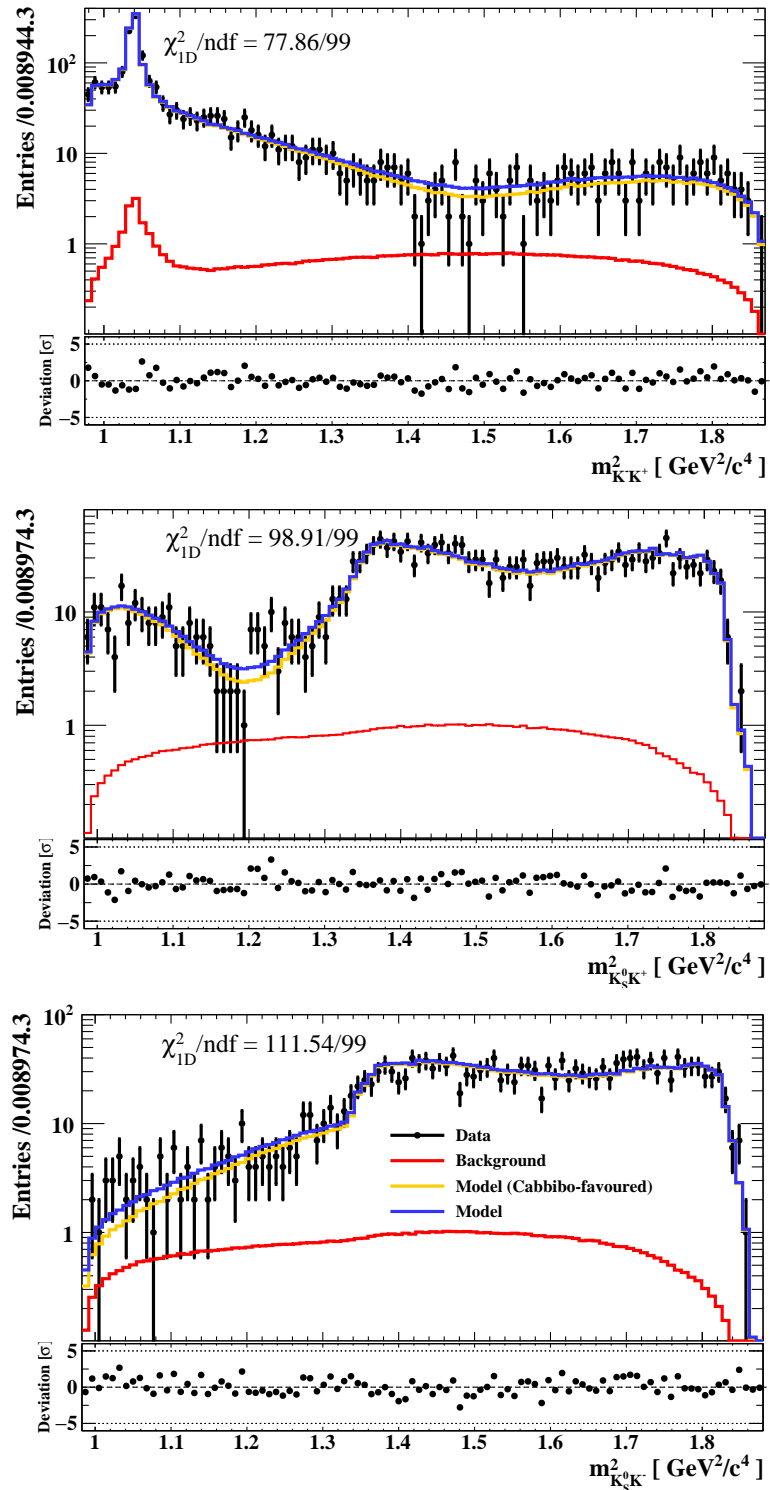


Figure B.4: Dalitz plot projections of data sample and amplitude model in logarithmic scale. The Cabibbo-favored component (orange), the background component (red) and the full amplitude (blue) are shown.

Table B.4: Interference terms of the Dalitz amplitude model. The largest interference occurs between the neutral and charged $a_0(980)$.

Interference [%]	$a_0(980)^0$	$a_0(980)^+$	$\phi(1020)$	$a_2(1320)^-$
$a_0(980)^0$	98.66	-71.09	0.15	1.80
$a_0(980)^+$		43.72	-2.17	-0.92
$\phi(1020)$			65.01	-0.57
$a_2(1320)^-$				1.05

Table B.5: Correlation matrix of the Dalitz amplitude model. The global correlation coefficient denotes the maximum correlation with any possible linear combination of all other parameters.

Correlation [%]		Global Coefficient	g_{KK}	$a_0(980)^+$		$\phi(1020)$		$a_2(1320)^-$	
				c	ϕ	c	ϕ	c	ϕ
g_{KK}		87.11	100	57.03	21.30	-19.16	-16.87	-50.33	11.59
$a_0(980)^+$	c	96.50		100	87.84	48.18	-11.40	-36.66	62.24
	ϕ	94.98			100	67.43	-5.08	-20.36	66.81
$\phi(1020)$	c	78.09				100	0.52	16.49	45.11
	ϕ	40.70					100	-19.69	9.86
$a_2(1320)^-$	c	62.57						100	-18.59
	ϕ	70.36							100

 Table B.6: Result from the Dalitz amplitude model using the nominal set of resonances but without considering the quantum entanglement of $D^0\bar{D}^0$. Uncertainties are statistical only. The coupling constant $a_0(980) \rightarrow K\bar{K}$ is determined to be $g_{K\bar{K}} = (2.82 \pm 0.22)$ GeV.

Final state	Magnitude	Phase [rad]	Fit fraction [%]
$a_0(980)^0 K_S^0$	1	0	75 ± 4
$a_0(980)^+ K^-$	0.67 ± 0.03	-2.81 ± 0.06	34 ± 4
$\phi(1020) K_S^0$	0.75 ± 0.03	1.82 ± 0.07	42 ± 1
$a_2(1320)^- K^+$	0.10 ± 0.03	0.45 ± 0.22	0.7 ± 0.4
Total			152 ± 6

Table B.7: Shape parameters for the untagged sample. The minimization succeeds and the covariance matrix is correctly estimated.

m_{KS}		m_{BC}	
Parameter	Final value	Parameter	Final value
CB2 α_L	1.54 ± 0.02	CB2 α_L	2.01 ± 0.02
CB2 α_R	1.76 ± 0.02	CB2 α_R	1.316 ± 0.007
CB2 m_0	$(497.89 \pm 0.01) \text{ MeV}/c^2$	CB2 m_0	$(1865.000 \pm 0.003) \text{ MeV}/c^2$
CB2 n_L	3.05 ± 0.09	CB2 n_L	2.16 ± 0.05
CB2 n_R	2.22 ± 0.05	CB2 n_R	2.44 ± 0.03
CB2 σ	$(2.138 \pm 0.009) \text{ MeV}$	CB2 σ	$(1.161 \pm 0.003) \text{ MeV}$
f_{comb}^{KS}	0.304 ± 0.003	E_{beam}	1.8865 GeV
s_{comb}	-1.36 ± 0.06	f_{comb}^{BC}	0.80 ± 0.02
$f_{nonK_S^0}^{KS}$	0.91 ± 0.02	p_{argus}	-2.0 ± 0.5
$s_{nonK_S^0}$	-1.4 ± 0.1	μ_{comb}	$(1864.5 \pm 0.4) \text{ MeV}/c^2$
		σ_{comb}	$(10.0 \pm 0.5) \text{ MeV}$
		$f_{nonK_S^0}^{BC}$	0.75 ± 0.02

Table B.8: Correlation matrix for the determination of the signal yield on data. The data sample and the fit model are shown in fig. 13.6. The number of signal events N_{signal} has only a small correlation to other parameters.

Correlation [%]	K_S^0 mass	K_S^0 width	N_{comb}	$N_{nonK_S^0}$	N_{signal}
K_S^0 mass	1	2.332	0.2967	-0.5069	0.1686
K_S^0 width		1	29.24	-52.4	18.22
N_{comb}			1	-63.23	5.741
$N_{nonK_S^0}$				1	-30.61
N_{signal}					1

C

SYSTEMATIC STUDIES OF DISPLACED VERTEX RECONSTRUCTION

C.1 INTRODUCTION

The reconstruction efficiency in most analyses is determined using Monte-Carlo simulation. Therefore, an accurate simulation of particle interaction and reconstruction is crucial and the uncertainty of the simulation is one of the largest systematic uncertainties in most analyses.

At BESIII Λ 's as well as K_s^0 's have a significant flight distance from the interaction point but still decay within the fiducial volume of the detector. Tracks originating from such secondary decay vertices can pose problems to the reconstruction procedure. We investigate this by measuring the reconstruction efficiency of $\Lambda \rightarrow \pi^- p$ and compare the results between data and simulation. We reconstruct Λ from J/ψ decays since the decay $J/\psi \rightarrow \Lambda \bar{\Lambda}$ offers constraint kinematics and essentially background free conditions.

At the time when this study was performed a significant difference of the K_s^0 reconstruction efficiency were observed and the measurement of the Λ reconstruction efficiency was intended as a cross-check. Nowadays these problems are solved and the K_s^0 reconstruction efficiency is simulated with an accuracy of about 1.5% [96].

Decay topology

The decay $J/\psi \rightarrow \Lambda \bar{\Lambda}$ provides good conditions to measure the Λ reconstruction efficiency. The recoiling Λ decays are illustrated in fig. C.1 and a reconstructed event in the detector is shown in fig. C.2. Both Λ 's are reconstructed in the channel $\Lambda \rightarrow \pi^- p$ and the final state is therefore $(\pi^- p)(\pi^+ \bar{p})$. The four charged tracks can be selected nearly background free. We also consider the decay $J/\psi \rightarrow \Lambda \bar{\Lambda} \gamma$ with a photon from initial or final state radiation as signal. The available phase-space of the decay $J/\psi \rightarrow \Lambda \bar{\Lambda}$ allows to measure the Λ reconstruction efficiency in the momentum range from 1.02 GeV to 1.14 GeV.

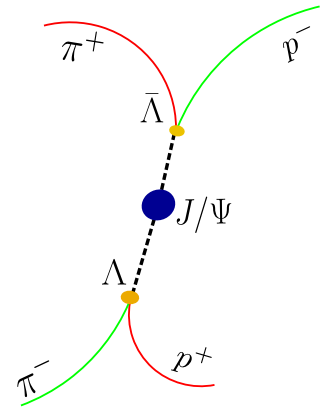


Figure C.1: $J/\psi \rightarrow \Lambda \bar{\Lambda}$ decay topology.

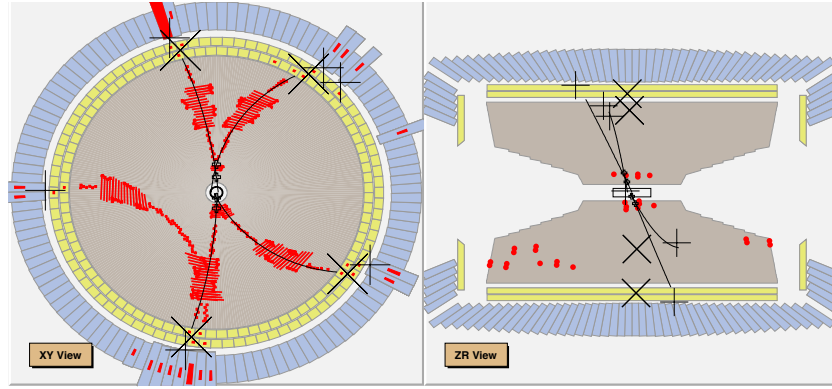


Figure C.2: $J/\psi \rightarrow \Lambda \bar{\Lambda}$ reaction in the detector with the line of sight along (left) and perpendicular (right) of the beam axis. Black lines are reconstructed charged tracks and red clusters are signals in the drift chamber, the time-of-flight system and the calorimeter.

Analysis strategy

Each signal event contains a pair of Λ decays. One Λ is used as tag candidate (Λ_{tag}) and we can calculate the missing four-momentum using the four-momenta of the tag and of the e^+e^- system:

$$\mathbf{p}_{miss}^{\Lambda_{recoil}} = \mathbf{p}^{e^+e^-} - \mathbf{p}^{tag}. \quad (\text{C.1})$$

On data the four-momentum of the e^+e^- system is calculated from the center-of-mass energy measurement and the crossing angle of the e^+e^- beams (11 mrad). In case that the missing mass is in the range of the Λ mass we assume that the event contains a $J/\psi \rightarrow \Lambda \bar{\Lambda}$ decay. The number of events satisfying this condition gives us the number of predicted Λ decays. Now we check if a second recoiling Λ can be reconstructed in the event. With the number of events with a pair of reconstructed Λ decays we can calculate the efficiency:

$$\epsilon_{rec}^{\Lambda} = \frac{\# \Lambda \text{ found}}{\# \Lambda \text{ predicted}}. \quad (\text{C.2})$$

The efficiency includes the detector acceptance for the Λ decay products. For comparing data and simulation we calculate the relative difference $\left(\frac{\epsilon_{data}}{\epsilon_{mc}} - 1\right)$. The detector acceptance cancels in this ratio.

The total Λ efficiency can be separated into efficiencies for the track reconstruction and for the vertex fit:

$$\epsilon_{rec}^{\Lambda} = \epsilon_{fit}^{vtx} \times \epsilon_{rec}^{\pi} \times \epsilon_{rec}^{proton}. \quad (\text{C.3})$$

The total Λ reconstruction efficiency and its dependence on vertex fit and flight distance are studied in appendix C.4. The efficiencies for pion and proton reconstruction from a displaced vertex are given in appendix C.4.

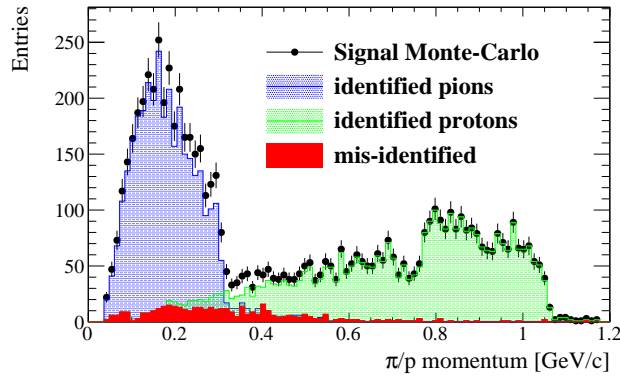


Figure C.3: Momentum of π/p tracks from Monte-Carlo simulation. Tracks identified as pions (blue) and tracks identified as protons (green) as well as mis-identified tracks (red) are shown. The Λ decay products are well separated by kinematics.

Data samples and software version

We use the J/ψ dataset which was taken during the 2009/10 data taking period. The J/ψ sample from the 2012/13 data taking is not taken into account. According to [102] the number of J/ψ decays in our data sample is $(225.0 \pm 2.8) \times 10^6$. As Monte-Carlo sample we use a generic J/ψ sample with 225×10^6 events. Data and Monte-Carlo samples were reconstructed using BOSS version 6.5.5 and analyzed using version 6.6.o.

C.2 SELECTION

Track selection

The momentum distribution for pions and protons from Λ decays is shown in fig. C.3. Pions have low momenta around 0.2 GeV and protons have larger momenta. The daughters of Λ decays are well separated by kinematics. We use particle identification to categorize charged tracks as pions or protons. Information from the dE/dx measurement in the drift chamber and from the energy measurement in the calorimeter is used to calculate probabilities for each particle hypothesis. For pion candidates we require the probability for the pion hypothesis to be large than for the proton hypothesis. Proton candidates must fulfill the inverted requirement. The mis-identification rate using this requirement is 6.9 % for pions and 4.5 % for protons. Another possibility to separate pion from proton tracks would be a requirement on the track momentum.

Table C.1: Selection requirements for the tag candidate.

Variable	min	max
Λ mass (3σ)	1.111 53 GeV	1.120 47 GeV
ΔE	-0.02 GeV	0.1 GeV
p	1.05 GeV	1.2 GeV
χ_{vtx}^2	0	30
χ_{secVtx}^2	0	30
flight distance	0.3 cm	200 cm
missing mass	1 GeV	1.2 GeV
cos(opening angle)	0.5	0.95

$\Lambda\bar{\Lambda}$ reconstruction and selection

We combine proton and pion candidates to form tag candidates of the Λ . The tag candidates must pass vertex (χ_{vtx}^2) and secondary vertex fit (χ_{secVtx}^2) with a χ^2 better than 30. The secondary vertex fit constrains the combined momentum of proton and pion to point back to the interaction region. In case of multiple candidates we select the candidate with the energy closest to the beam energy $E_{beam} = 1.549$ GeV. Figure C.4 shows variables of the tag candidate after a loose preselection. The signal is characterized by a peak in Λ_{tag} mass and the missing mass distributions around the Λ mass $m_\Lambda = 1.115$ GeV[7]. Due to the back-to-back kinematics of the $J/\psi \rightarrow \Lambda\bar{\Lambda}$ decay the signal distributions in ΔE and the momentum are also very narrow. The signal distribution has tails in missing mass, ΔE and the momentum which come from $J/\psi \rightarrow \Lambda\bar{\Lambda} + \gamma$ decays.

The selection requirements are listed in table C.1 and the regions excluded by the selection are marked in fig. C.4. The selection is optimized for a good background suppression and we obtain a sample with a background impurity of

$$B/(S + B) = (0.40 \pm 0.03) \%. \quad (\text{C.4})$$

The resulting Λ_{tag} mass distribution after the selection is shown in fig. C.5(a). The efficiency for reconstruction and preselection of the tag decay is $\epsilon_{pre}^{rec} = 0.741 \pm 0.002$ and the selection requirements reduce signal events by $\epsilon_{sel} = 0.910 \pm 0.003$. This gives a total efficiency for reconstruction of the tag decay of $\epsilon_{pre}^{rec} = 0.675 \pm 0.002$. The efficiency we want to determine is the reconstruction efficiency of the recoiling Λ .

In the next step we combine the remaining pion and proton candidates to reconstruct the recoiling Λ decay. In case of multiple candidates we use again the energy difference to the beam energy to select the best candidate. On the recoil side, vertex and secondary vertex fit are required to succeed. No further selection is applied. The mass distribution for Λ_{recoil} candidates is shown in fig. C.5(b)

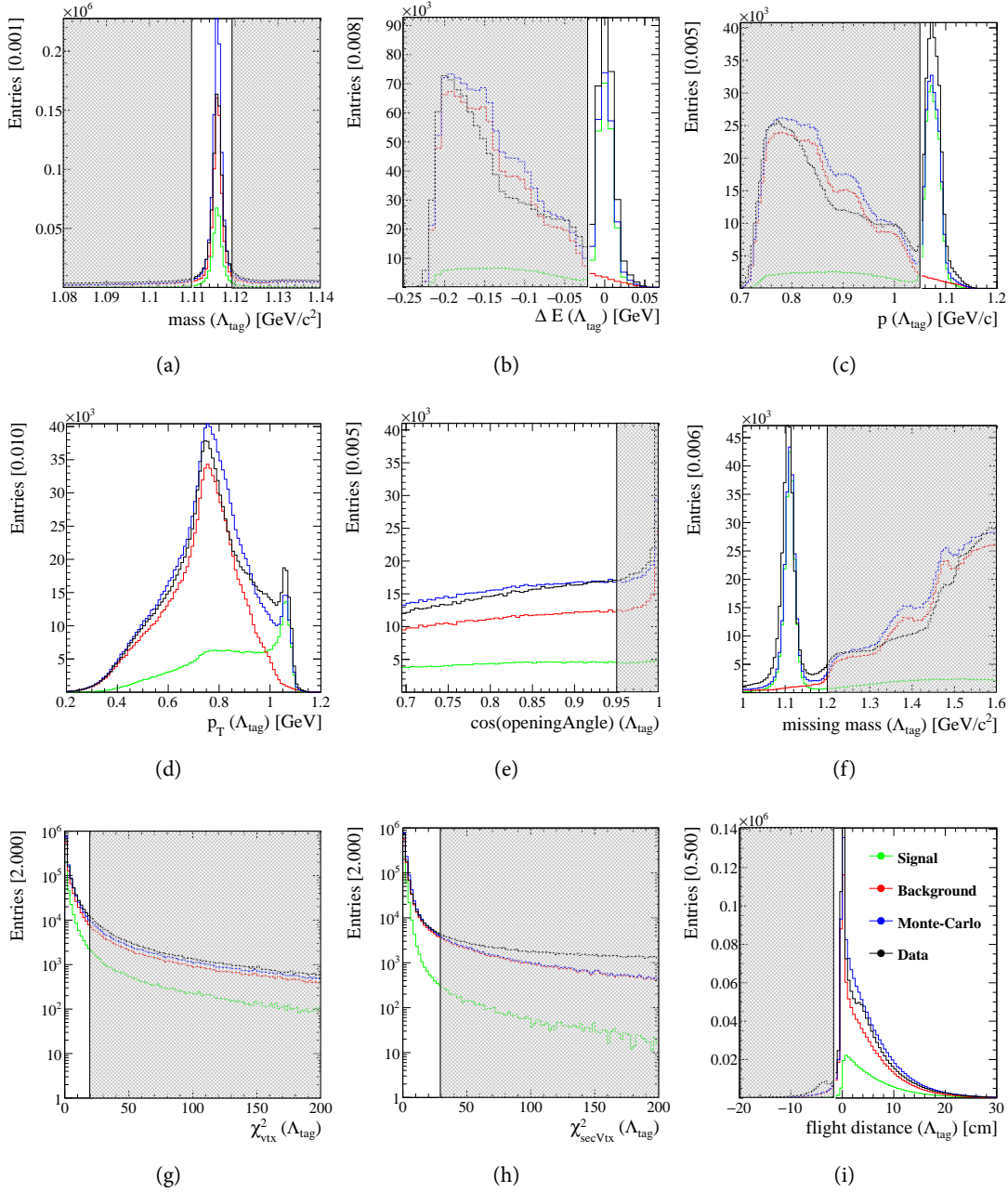


Figure C.4: Variables of the Λ tag decay after a loose preselection. The data sample is shown in black and the Monte-Carlo sample (blue) is separated into signal (green) and background (red). Regions excluded by the selection (table C.1) are marked.

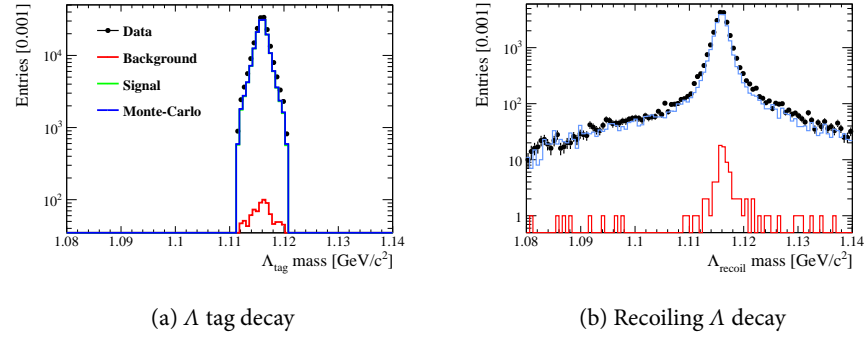


Figure C.5: Mass distributions of the tag and recoil decay.

Background

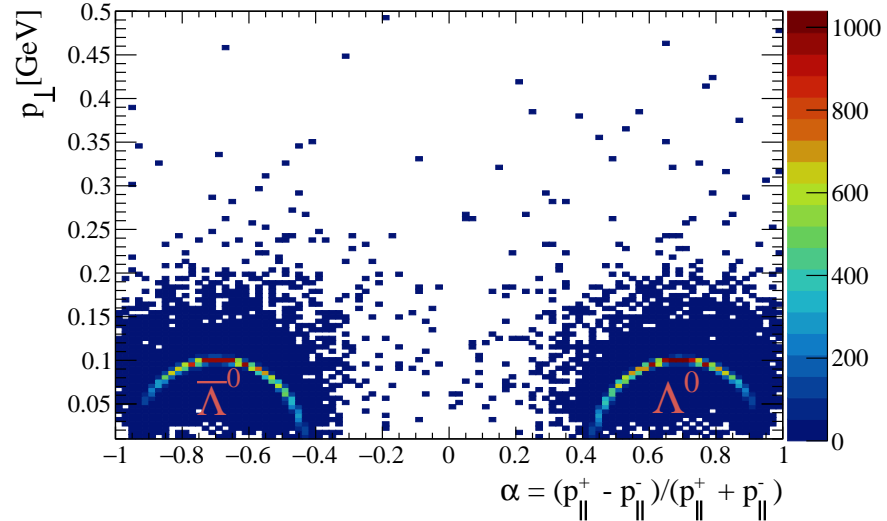


Figure C.6: The Armenteros-Podolanski diagram shows the asymmetry of the parallel momenta (α) versus the transversal momentum of π/p . Momenta are measured in the laboratory frame with respect to the Λ flight direction. The topology is illustrated in fig. C.7.

The decay $J/\psi \rightarrow \Lambda \bar{\Lambda}$ provides a clean sample of Λ decays. We will neglect the remaining background in the analysis but first we want to give an overview which background decays survive our selection. In fig. C.8 we show the missing mass of the recoil decay (left) and the mass of the reconstructed recoil decay (right) versus an event ID. The event ID is a unique identifier for the event topology. Channels that contribute to the background are labeled. Some channels classified as background have the final state $\Lambda \bar{\Lambda} + \gamma$ or have at least a $\Lambda \bar{\Lambda}$ pair in the final state. These channels could also be classified as signal, but might have a different reconstruction efficiency.

In fig. C.6 we show the Armenteros-Podolanski (AP) diagram. It shows the transversal momentum component of the Λ daughter particle versus the

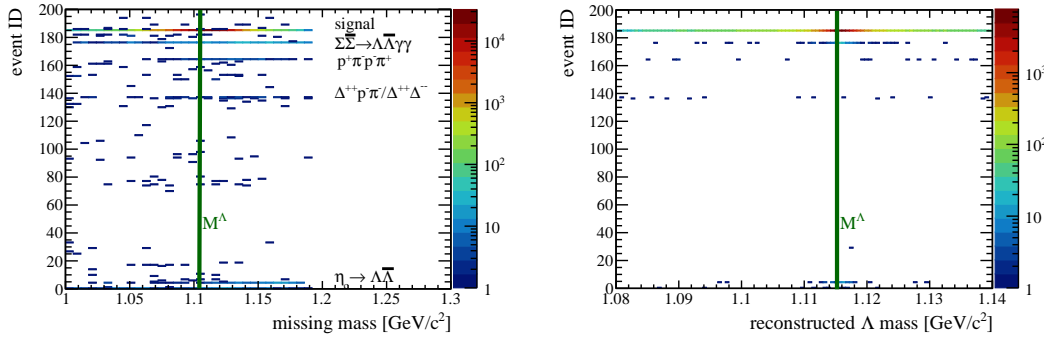


Figure C.8: Missing mass and reconstructed mass of the Λ recoil decay versus event topology ID. Prominent channels are labeled, and the Λ mass is marked.

asymmetry of the parallel component (see also fig. C.7). The momenta are calculated in the laboratory frame with respect to the Λ flight distance. This diagram is correlated to the opening angle and can discriminate between K_s^0 and Λ decays. K_s^0 decays would appear as symmetric distribution around $\alpha = 0$. Λ decays have positive and $\bar{\Lambda}$ decays negative values of α .

In general AP diagrams can be used to obtain clean samples of pions, protons and photons which can be used to calibrate the particle identification system.

C.3 BRANCHING FRACTION

We measure the branching fraction $J/\psi \rightarrow \Lambda \bar{\Lambda}$ as a cross-check. It is given by:

$$\mathcal{B}(J/\psi \rightarrow \Lambda \bar{\Lambda}) = \frac{N^{\text{signal}}}{\epsilon_{\text{rec}} \times N_{J/\psi}}. \quad (\text{C.5})$$

The signal yield N^{signal} is corrected for the background impurity given in eq. (C.4). The background impurity as well as the reconstruction efficiency ϵ_{rec} is obtained from simulation. $N_{J/\psi}$ is the total number of J/ψ decays in our data sample [102]. The parameters for the branching fraction are summarized in table C.2 and we obtain a result of

$$\mathcal{B}(J/\psi \rightarrow \Lambda \bar{\Lambda}) = (2.07 \pm 0.03 \text{ (stat.)} \pm 0.08 \text{ (sys.)}) \times 10^{-3}. \quad (\text{C.6})$$

The total uncertainty is 4.1 %.

The systematic uncertainty involves the efficiency difference for a pair of reconstructed Λ 's. We use the result from appendix C.4 and assign a uncertainty of 4 %. Since in the efficiency determination no selection requirements were applied, we have to study this influence separately by varying the selection criteria in a suitable range. We find a variation below 0.02 % and neglect this source of uncertainty. We assign a conservative uncertainty to the background correction of 50 % of the correction itself. Due to the small background contamination this source of uncertainty is also negligible. Since this measurement is intended

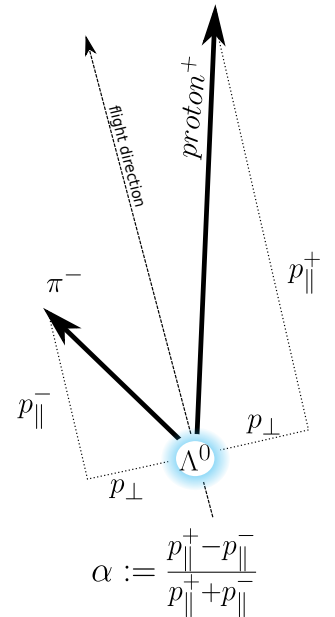


Figure C.7: Illustration of the decay $\Lambda \rightarrow \pi^- p$. The asymmetry of the longitudinal momenta (α) is shown in fig. C.6.

Table C.2: Parameters for branching fraction measurement.

Simulation	Number of J/ψ decays	225×10^6
	Generated decays	362 250
	Yield (S+B)	44 310
	Signal yield (S)	44 118
	Background yield (B)	192
Purity S/(S+B)		$(99.60 \pm 0.03) \%$
Efficiency		$(12.18 \pm 0.06) \%$
Data	Number of J/ψ decays	$(225.0 \pm 2.8) \times 10^6$
	Signal yield (w/ background)	$56\,813 \pm 238$
	Signal yield (w/o background)	$56\,565 \pm 237$ (stat.) ± 124 (sys.)

to be a cross-check we do not further investigate the systematic uncertainties (e. g. the influence of the decay $J/\psi \rightarrow \Lambda\bar{\Lambda} + \gamma$).

The current average values of the particle data group is $(1.61 \pm 0.15) \times 10^{-3}$ [7]. This value is used for Monte-Carlo simulation. It is an average value which includes results from old experiments. The newest results from *BABAR* and *BESII* are $(1.93 \pm 0.21$ (stat.) ± 0.05 (sys.)) $\times 10^{-3}$ [99] and $(2.03 \pm 0.03$ (stat.) ± 0.15 (sys.)) $\times 10^{-3}$ [100]. There is a tension between our result and the PDG average but it is in good agreement with the measurements from *BABAR* and *BESII*.

C.4 RECONSTRUCTION EFFICIENCY

The reconstruction efficiency can be calculated using the number reconstructed tag decays (predicted Λ decays) and the number of reconstructed $\Lambda\bar{\Lambda}$ pairs (see appendix C.1). We find that the Λ reconstruction efficiencies for data and simulation are consistent on a level of about 2 %. An overview is given in table C.3.

In order to do a more detailed comparison we calculate ϵ_{rec}^{Λ} in bins of kinematic variables of the recoil decay. The predicted variables are shown in fig. C.9. The results for the differential Λ reconstruction efficiency in bins of p , p_T , $\cos(\Theta)$ and ϕ are shown in fig. C.10. The distribution of the efficiency for data and simulation is shown above their relative deviation $\left(\frac{\epsilon_{data}}{\epsilon_{mc}} - 1\right)$ per bin. The red line marks the total deviation between data and simulation.

The $\cos(\Theta)$ efficiency distributions drops close to ± 1 . This is the region where the decay products are likely to go into the beam pipe. The distribution in ϕ is not flat. This originates from the reference frame in which the momenta are measured. Since we do not boost the momenta to the J/ψ rest frame, the boost of the e^+e^- system in x -direction causes a non-flat efficiency distribution in ϕ . The agreement between data and simulation is fairly good.

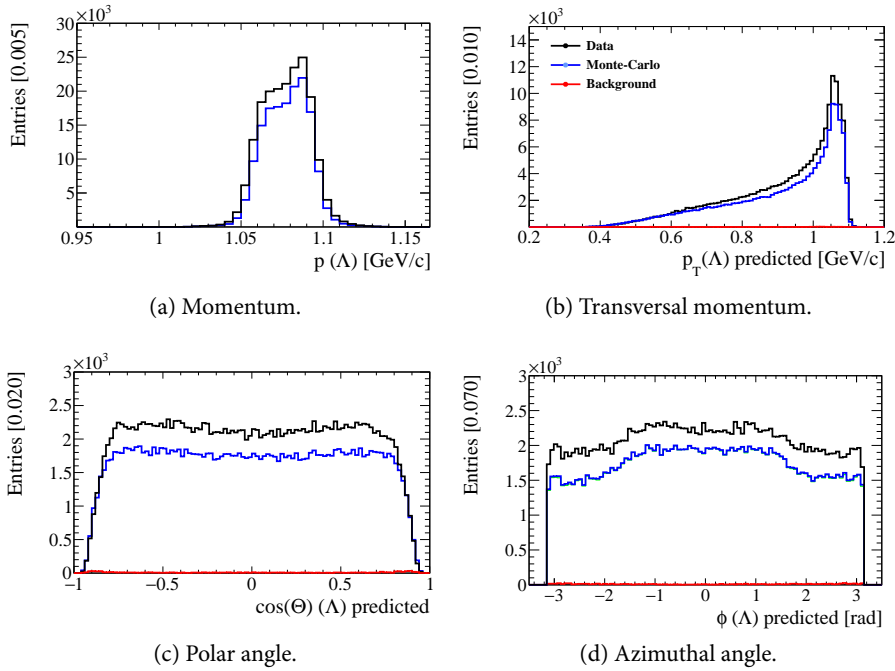


Figure C.9: Kinematic variables for the Λ recoil decay predicted from four-momentum conservation. The branching fraction in the simulation is different from data, therefore different yields are observed.

Furthermore we measure the Λ reconstruction efficiency without vertex and/or secondary vertex fit. The deviation between simulation and data is similar. Vertex and secondary vertex fit have a efficiency in data of 92.2 % and 98.8 %, respectively.

Pion and proton reconstruction efficiency

The Λ reconstruction efficiency can be factorized into efficiencies of the vertex fit and the tracking efficiencies, see eq. (C.3). We want to study the reconstruction efficiencies of pions (ϵ_{rec}^{π}) and protons (ϵ_{rec}^{proton}) from Λ decays. We require a Λ_{tag} and a good pion or proton track for the proton and pion efficiency, respectively. We remove events with more than one good track. Then we can calculate the missing four-momentum:

$$\mathbf{p}_{miss}^{p/\pi} = \mathbf{p}^{e^+e^-} - \mathbf{p}^{tag} - \mathbf{p}^{\pi/p}. \quad (\text{C.7})$$

We reconstruct the Λ_{recoil} candidate without vertex and secondary vertex fit and then the efficiency is calculated according to eq. (C.2).

The reconstruction efficiencies for pions and protons from a displaced vertex are compared between data and simulation in table C.4. Both agree on a level of (-1.7 ± 0.3) and (-0.7 ± 0.2) , respectively. The differential efficiency in bins of momentum, transversal momentum, polar angle, azimuthal angle and flight distance of the Λ for pions as well as for protons are shown in fig. C.11. The

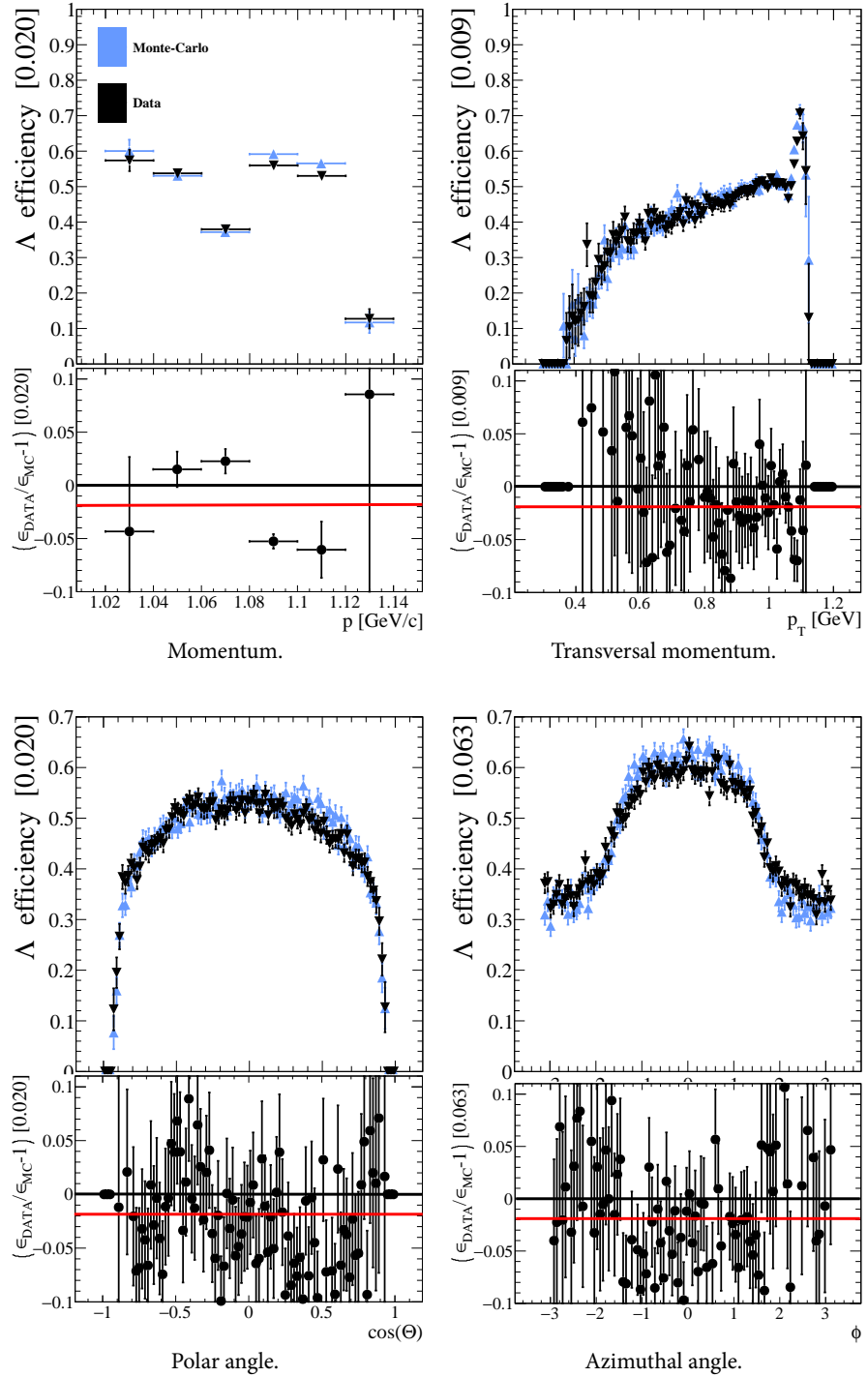


Figure C.10: Reconstruction efficiency for Λ decays to $\pi^+ p$ in data (black) and simulation (blue). The relative deviation is shown below each distribution. The red line indicates the integrated difference.

Table C.3: Λ reconstruction efficiency. Efficiencies with a requirement on the Λ flight distances are calculated using an additional good pion track. This is necessary to estimate the Λ decay vertex (see appendix C.4).

	Data [%]	Simulation [%]	$\left(\frac{\epsilon_{data}}{\epsilon_{mc}} - 1\right)$ [%]
Nominal	47.9 ± 0.2	48.8 ± 0.2	-1.9 ± 0.6
no fit	52.6 ± 0.6	53.3 ± 0.7	-1.32 ± 0.16
no secondary vertex fit	48.5 ± 0.6	49.3 ± 0.7	-1.68 ± 0.18
flight distance >8 mm	14.9 ± 0.1	15.0 ± 0.1	-0.45 ± 1.33
flight distance $>50 \sigma$	18.1 ± 0.1	17.8 ± 0.2	1.8 ± 1.2

Table C.4: Reconstruction efficiencies of π/p .

Track	Data [%]	Simulation [%]	$\left(\frac{\epsilon_{data}}{\epsilon_{mc}} - 1\right)$ [%]
π^+	73.3 ± 0.2	73.6 ± 0.2	-0.4
π^-	74.4 ± 0.2	76.8 ± 0.2	-3.1
Combined	73.9 ± 0.2	75.2 ± 0.2	-1.7 ± 0.3
p	88.6 ± 0.2	89.7 ± 0.2	-1.2
\bar{p}	86.1 ± 0.2	86.3 ± 0.2	-0.2
Combined	87.4 ± 0.1	88.0 ± 0.1	-0.7 ± 0.2

efficiency distributions agree well. A small systematic deviation can be observed in the ϕ distribution for pions.

In a last check we separate the efficiencies for pions and protons by their charge. The integrated efficiencies are listed in table C.4 and in bins of p_T the efficiency is shown in fig. C.12. Some dependence of the reconstruction efficiency on the charge is expected. Data and simulation agree well in general but for π^- the deviation between data and simulation is significant (3.1%). The discrepancy can also be see in fig. C.12(b) in the high momentum region.

C.5 CONCLUSION

We study the reconstruction efficiency in data and simulation for Λ decays and for pions and protons from displaced Λ vertices. The decay $J/\psi \rightarrow \Lambda \bar{\Lambda}$ offers constraint kinematics and is almost background free. In general the Λ reconstruction efficiency is overestimated by 1.9% in simulation. From detailed studies of the dependence on flight distance and the charge of the final state tracks we find that:

- Λ decays with a large flight distance are better simulated.
- The pion efficiency distribution in the azimuthal angle shows a small systematic deviation between data and simulation.

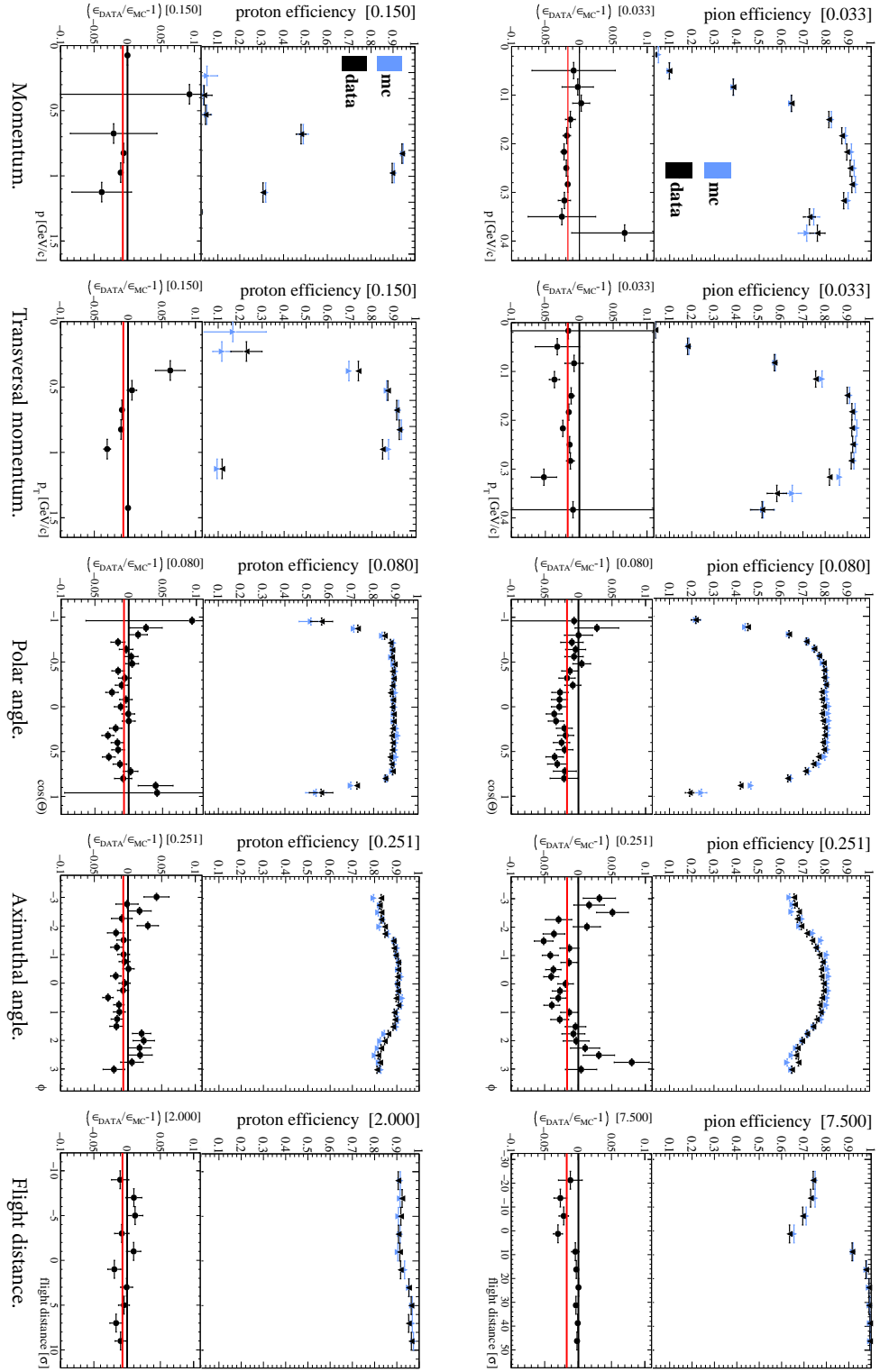


Figure C.11: Reconstruction efficiency for pions and protons from Λ decays in data (black) and simulation (blue). The relative deviation is shown below each distribution. The red line indicates the integrated relative difference.

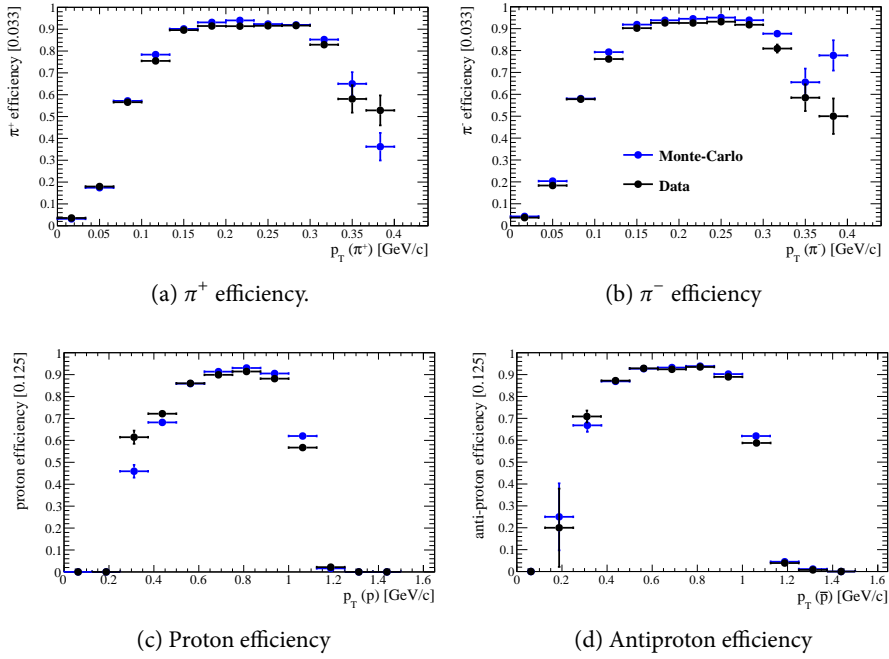


Figure C.12: Efficiency in bins of transversal momentum for π/p separated by charge.

- The efficiency of negative pion tracks show a significant deviation.

We conclude that the Λ reconstruction is well simulated and no general problems were found in the reconstruction of a displaced vertex.

Within this analysis we measured the branching fraction $J/\psi \rightarrow \Lambda\bar{\Lambda}$:

$$\mathcal{B}(J/\psi \rightarrow \Lambda\bar{\Lambda}) = (2.07 \pm 0.03 \text{ (stat.)} \pm 0.08 \text{ (sys.)}) \times 10^{-3}. \quad (\text{C.6})$$

This result is in good agreement with results from *BABAR* [99] and *BESII*[100].

This work is provided to the collaboration [98].

BIBLIOGRAPHY

1. Popper, K. 'Logik der Forschung' (J. Springer, 1935).
2. Aad, G. *et al.* 'Observation of a new particle in the search for the Standard Model Higgs boson with the ATLAS detector at the LHC'. *Physics Letters B* **716**, 1–29 (2012).
3. Chatrchyan, S. *et al.* 'Observation of a new boson at a mass of 125 GeV with the CMS experiment at the LHC'. *Physics Letters B* **716**, 30–61 (2012).
4. Wikimedia Commons. *Constituents of the Standard Model* <https://commons.wikimedia.org/wiki/File:Standard_Model_of_Elementary_Particles.svg>.
5. Yukawa, H. 'On the Interaction of Elementary Particles I'. *Progress of Theoretical Physics Supplement* **1**, 1–10 (1955).
6. Alekseev, M. G. *et al.* 'Observation of a $J^{PC} = 1^{-+}$ exotic resonance in diffractive dissociation of 190 GeV/c π^{-} into $\pi^{-}\pi^{-}\pi^{+}$ '. *Physical Review Letters* **104**, 1–7 (2010).
7. Olive, K. 'Review of Particle Physics'. *Chinese Physics C* **38**, 090001 (2014).
8. Ablikim, M. *et al.* 'Observation of a Charged Charmoniumlike Structure in $e^{+}e^{-} \rightarrow \pi^{+}\pi^{-}J/\Psi$ at $\sqrt{s} = 4.26$ GeV'. *Physical Review Letters* **110**, 252001 (2013).
9. Ablikim, M. *et al.* 'Observation of a Charged $(D\bar{D}^{*})^{\pm}$ Mass Peak in $e^{+}e^{-} \rightarrow \pi D\bar{D}^{*}$ at $\sqrt{s} = 4.26$ GeV'. *Physical Review Letters* **112**, 022001 (2014).
10. Aubert, J. J. *et al.* 'Experimental observation of a heavy particle J '. *Physical Review Letters* **33**, 1404–1406 (1974).
11. Augustin, J. E. *et al.* 'Discovery of a narrow resonance in $e^{+}e^{-}$ annihilation'. *Physical Review Letters* **33**, 1406–1408 (1974).
12. Aubert, B. *et al.* 'Observation of a Narrow Meson State Decaying to $D_s^{+}\pi^0$ at a Mass of 2.32 GeV/c²'. *Physical Review Letters* **90**, 242001 (2003).
13. Aubert, B. *et al.* 'Evidence for $D^0 - \bar{D}^0$ Mixing'. *Physical Review Letters* **98**, 211802 (2007).
14. Starič, M. *et al.* 'Evidence for $D^0 - \bar{D}^0$ Mixing'. *Physical Review Letters* **98**, 211803 (2007).
15. Aaij, R. *et al.* 'Observation of $D^0 - \bar{D}^0$ Oscillations'. *Physical Review Letters* **110**, 101802 (2013).
16. Gersabeck, M. 'Brief Review of Charm Physics'. *Modern Physics Letters A* **27**, 1230026 (2012).

17. Libby, J. *et al.* ‘Model-independent determination of the strong-phase difference between D^0 and $\overline{D^0}$ to $K_{S,L}^0 h^+ h^-$ ($h = \pi, K$) and its impact on the measurement of the CKM angle γ/ϕ_3 ’. *Physical Review D* **82**, 112006 (2010).
18. Aubert, B. *et al.* ‘Dalitz plot analysis of $D^0 \rightarrow \overline{K^0} K^+ K^-$ ’. *Physical Review D* **72**, 052008 (2005).
19. Aubert, B. *et al.* ‘Improved measurement of the CKM angle γ in $B^\mp \rightarrow D^{(*)} K^{(*)\mp}$ decays with a Dalitz plot analysis of D decays to $K_S^0 \pi^+ \pi^-$ and $K_S^0 K^+ K^-$ ’. *Physical Review D* **78**, 034023 (2008).
20. Mandelstam, S. ‘Determination of the Pion-Nucleon Scattering Amplitude from Dispersion Relations and Unitarity. General Theory’. *Physical Review* **112**, 1344–1360 (1958).
21. Martin, A. & Spearman, T. ‘Elementary Particle Theory’ (North-Holland, Amsterdam, 1970).
22. Omnès, R. & Froissart, M. ‘Mandelstam Theory and Regge Poles: An Introduction for Experimentalists’ (Benjamin, 1963).
23. Latham, T. *et al.* *Laura++* <<https://laura.hepforge.org>>.
24. Dalitz, R. H. ‘Decay of τ Mesons of Known Charge’. *Physical Review* **94**, 1046–1051 (1954).
25. Chung, S.-U. ‘Spin Formalisms’. *BNL Preprint GQS* **02-090**, 1–90 (2014).
26. Jacob, M. & Wick, G. ‘On the general theory of collisions for particles with spin’. *Annals of Physics* **7**, 404–428 (1959).
27. Richman, J. ‘An Experimenter’s Guide to the Helicity Formalism’. *DOE Research and Development Report* **CALT-68**, 40 (1984).
28. Peters, K. ‘A Primer in partial wave analysis’. *International Journal of Modern Physics A* **21**, 5618–5624 (2006).
29. Wikimedia Commons. *Euler Angles* <<https://commons.wikimedia.org/wiki/File:Eulerangles.svg>>.
30. Wigner, E. ‘Gruppentheorie und ihre Anwendungen auf die Quantenmechanik der Atomspektren’ (Vieweg, Braunschweig, 1931).
31. Breit, G. & Wigner, E. ‘Capture of Slow Neutrons’. *Physical Review* **49**, 519–531 (1936).
32. Flatté, S. ‘Coupled-channel analysis of the $\pi\eta$ and $K\overline{K}$ systems near $K\overline{K}$ threshold’. *Physics Letters B* **63**, 224–227 (1976).
33. Arfken, G. & Weber, H. ‘Essential Mathematical Methods for Physicists’ 4th ed. (Academic Press, 2003).
34. Blatt, J. M. & Weisskopf, V. F. ‘Theoretical Nuclear Physics’ (Springer New York, New York, NY, 1979).
35. Chung, S. U. *et al.* ‘Partial wave analysis in K-matrix formalism’. *Annalen der Physik* **507**, 404–430 (1995).

36. Pitka, A. $D^0 - \bar{D}^0$ Mischung im Zerfall $D^0 \rightarrow K_S \pi^+ \pi^-$ am PANDA Experiment PhD thesis (Justus-Liebig-Universität Gießen, 2015).
37. Asner, D. M. & Sun, W. M. ‘Time-Independent Measurements of $D^0 - \bar{D}^0$ Mixing and Relative Strong Phases Using Quantum Correlations’. *Physical Review D* **73**, 034024 (2005).
38. Amhis, Y. *et al.* ‘Averages of b -hadron, c -hadron, and τ -lepton properties as of summer 2014’. arXiv: 1412.7515.
39. Fang, S. & Chen, S. ‘The Beijing Electron-Positron collider’. *Particle Accelerators* **26**, 51–61 (1990).
40. BESIII <<http://bes3.ihep.ac.cn>> (visited on 21/07/2016).
41. Zhang, C. & Wang, J. *The Beijing Electron-Positron Collider and its second phase construction* in *Proceedings of EPAC* (Luzern, Switzerland, 2004), 230–232.
42. Yu, C. ‘The Operation Status of BEPCII’. *Talk at BESIII Summer Collaboration meeting* (2016).
43. Harris, F. A. ‘BEPCII and BESIII’. *International Journal of Modern Physics A* **24**, 377–384 (2009).
44. Beijing Synchrotron Radiation Facility <http://english.ihep.cas.cn/rs/fs/srl/aboutbsrf/briefintroduction/201204/t20120417_83958.html> (visited on 21/07/2016).
45. Ulrich, M. *Private Communication* 2013.
46. Bennett, J. *et al.* ‘MDC performance from calibration (T_0 , MDC-tracking, dE/dx)’. *Talk at BESIII Spring meeting* (2015).
47. Ablikim, M. *et al.* ‘Design and construction of the BESIII detector’. *Nuclear Instruments and Methods in Physics Research A* **614**, 345–399 (2010).
48. Sun, S. ‘First glance at the MPRC data’. *Talk at BESIII Spring meeting* (2015).
49. Feldbauer, F. ‘Current Status and Performance of the BESIII Electromagnetic Calorimeter’. *Journal of Physics: Conference Series* **587**, 012046 (2015).
50. Han, J. *et al.* ‘Cosmic ray test results on resistive plate chamber for the BESIII experiments’. *Nuclear Instruments and Methods in Physics Research A* **577**, 552–557 (2007).
51. Clemencic, M. *et al.* ‘Recent developments in the LHCb software framework gaudi’. *Journal of Physics: Conference Series* **219**, 042006 (2010).
52. Ping, R.-G. ‘Event generators at BESIII’. *Chinese Physics C* **32**, 599–602 (2008).
53. Jadach, S. *et al.* ‘The precision Monte Carlo event generator for $K\bar{K}$ two-fermion final states in e^+e^- collisions’. *Computer Physics Communications* **130**, 260–325 (2000).

54. Lange, D. J. ‘The EvtGen particle decay simulation package’. *Nuclear Instruments and Methods in Physics Research A* **462**, 152–155 (2001).
55. Barberio, E. & Was, Z. ‘PHOTOS - a universal Monte Carlo for QED radiative corrections’. *Computer Physics Communications* **79**, 291–308 (1994).
56. Sjöstrand, T. *et al.* ‘PYTHIA 6.4 physics and manual’. *Journal of High Energy Physics* **2006**, 026–026 (2006).
57. Yang, R.-L. *et al.* ‘Tuning and Validation of the Lundcharm Model with J/Ψ Decays’. *Chinese Physics Letters* **31**, 061301 (2014).
58. Balossini, G. *et al.* ‘Matching perturbative and parton shower corrections to Bhabha process at flavour factories’. *Nuclear Physics B* **758**, 227–253 (2006).
59. Jadach, S. *et al.* ‘BHWIDE 1.00: $O(\alpha)$ YFS exponentiated Monte Carlo for Bhabha scattering at wide angles for LEP1/SLC and LEP2’. *Physics Letters B* **390**, 298–308 (1997).
60. Guan, Y.-H. *et al.* ‘Study of the efficiency of event start time determination at BESIII’. *Chinese Physics C* **38**, 016201 (2014).
61. Bevan, a. J. *et al.* ‘The Physics of the B Factories’. *AIP Conference Proceedings* **214**, 928 (2014).
62. He, M. ‘Simulation and reconstruction of the BESIII EMC’. *Journal of Physics: Conference Series* **293**, 012025 (2011).
63. Kalman, R. E. ‘A New Approach to Linear Filtering and Prediction Problems’. *Journal of Basic Engineering* **82**, 35 (1960).
64. Gang, Q. *et al.* ‘Particle identification using artificial neural networks at BESIII’. *Chinese Physics C* **32**, 1–8 (2010).
65. Asner, D. M. *et al.* ‘Physics at BES-III’. *International Journal of Modern Physics A* **24**, 2009 (2008).
66. Michel, M. *et al.* ‘CompPWA: A common amplitude analysis framework for PANDA’. *Journal of Physics: Conference Series* **513**, 022025 (2014).
67. Brun, R. & Rademakers, F. ‘ROOT - An object oriented data analysis framework’. *Nuclear Instruments and Methods in Physics Research A* **389**, 81–86 (1997).
68. Berlich, R. *et al.* *Parametric Optimization with the Geneva Library Collection* 2014. <<http://www.gemfony.eu>>.
69. Ablikim, M. *et al.* ‘Measurement of the $e^+e^- \rightarrow \pi^+\pi^-\pi^-$ cross section between 600 and 900 MeV using initial state radiation’. *Physics Letters B* **753**, 629–638 (2016).
70. Albrecht, H. *et al.* ‘Search for $b \rightarrow s\gamma$ in exclusive decays of B mesons’. *Physics Letters B* **229**, 304–308 (1989).
71. Williams, M. ‘How good are your fits? Unbinned multivariate goodness-of-fit tests in high energy physics’. *Journal of Instrumentation* **5**, 09004 (2010).

72. Aslan, B. & Zech, G. ‘Statistical energy as a tool for binning-free, multivariate goodness-of-fit tests, two-sample comparison and unfolding’. *Nuclear Instruments and Methods in Physics Research A* **537**, 626–636 (2005).
73. Wilks, S. S. ‘The Large-Sample Distribution of the Likelihood Ratio for Testing Composite Hypotheses’. *The Annals of Mathematical Statistics* **9**, 60–62 (1938).
74. Ambrosino, F. *et al.* ‘Dalitz plot analysis of $e^+e^- \rightarrow \pi^0\pi^0\gamma$ events at $\sqrt{s} \simeq M_\phi$ with the KLOE detector’. *The European Physical Journal C* **49**, 473–488 (2007).
75. García-Martín, R. *et al.* ‘Precise determination of the $f_0(600)$ and $f_0(980)$ pole parameters from a dispersive data analysis’. *Physical Review Letters* **107**, 1–5 (2011).
76. Ablikim, M. *et al.* ‘Resonances in $J/\Psi \rightarrow \phi\pi^+\pi^-$ and ϕK^+K^- ’. *Physics Letters B* **607**, 243–253 (2005).
77. Ambrosino, F. *et al.* ‘Study of the $a_0(980)$ meson via radiative decay $\phi \rightarrow \eta\pi^0\gamma$ with the KLOE detector’. *Physics Letters B* **681**, 5–13 (2009).
78. Bugg, D. ‘Reanalysis of data on $a_0(1450)$ and $a_0(980)$ ’. *Physical Review D* **78**, 074023 (2008).
79. Athar, S. B. *et al.* ‘ χ_{cJ} decays to $h^+h^-h^0$ ’. *Physical Review D* **75**, 1–13 (2007).
80. Adams, G. S. *et al.* ‘Amplitude analyses of the decays $\chi_{c1} \rightarrow \eta\pi^+\pi^-$ and $\chi_{c1} \rightarrow \eta'\pi^+\pi^-$ ’. *Physical Review D* **84**, 1–17 (2011).
81. Kornicer, M. ‘Amplitude analysis of $\chi_{c1} \rightarrow \eta\pi^+\pi^-$ decays at BESIII’. *BESIII internal memo* **364** (2016).
82. Abele, A. *et al.* ‘ $\bar{p}p$ annihilation at rest into $K_L K^\pm \pi^\mp$ ’. *Physical Review D* **57**, 3860–3872 (1998).
83. Teige, S. *et al.* ‘Properties of the $a_0(980)$ meson’. *Physical Review D* **59**, 012001 (1998).
84. Lees, J. P. *et al.* ‘Precision measurement of the $e^+e^- \rightarrow K^+K^-(\gamma)$ cross section with the initial-state radiation method at BABAR’. *Physical Review D* **88** (2013).
85. Ablikim, M. *et al.* ‘Partial wave analyses of $J/\Psi \rightarrow \gamma\pi^+\pi^-$ and $\gamma\pi^0\pi^0$ ’. *Physics Letters B* **642**, 441–448 (2006).
86. Cleland, W. *et al.* ‘Resonance production in the reaction $\pi^\pm p \rightarrow K_S^0 K^\pm p$ at 30 and 50 GeV/c’. *Nuclear Physics B* **208**, 228–261 (1982).
87. Vladimirovsky, V. V. *et al.* ‘Analysis of the $K_S K_S$ system from the reaction $\pi p \rightarrow K_S K_S n$ at 40 GeV’. *Physics of Atomic Nuclei* **69**, 493–509 (2006).
88. Amsler, C. *et al.* ‘Coupled channel analysis of p annihilation into $\pi^0\pi^0\pi^0$, $\pi^0\eta\eta$ and $\pi^0\pi^0\eta'$ ’. *Physics Letters B* **355**, 425–432 (1995).
89. Abele, A. *et al.* ‘Antiproton-proton annihilation at rest into $K^+K^-\pi^0$ ’. *Physics Letters B* **468**, 178–188 (1999).

90. Tibshirani, R. 'Regression Shrinkage and Selection via the Lasso'. *Journal of the Royal Statistical Society. Series B (Methodological)* **58**, 267–288 (1996).
91. Guegan, B. *et al.* 'Model selection for amplitude analysis'. *Journal of Instrumentation* **10**, P09002–P09002 (2015).
92. Schwarz, G. 'Estimating the Dimension of a Model'. *The Annals of Statistics* **6**, 461–464 (1978).
93. Akaike, H. 'A new look at the statistical model identification'. *IEEE Transactions on Automatic Control* **19**, 716–723 (1974).
94. Ablikim, M. *et al.* 'Measurement of the integrated luminosities of the data taken by BESIII at $\sqrt{s} = 3.650$ and 3.773 GeV'. *Chinese Physics C* **37**, 123001 (2013).
95. Dobbs, S. *et al.* 'Measurement of absolute hadronic branching fractions of D mesons and $e^+e^- \rightarrow D\bar{D}$ cross sections at the $\Psi(3770)$ '. *Physical Review D* **76**, 112001 (2007).
96. Ma, T. *et al.* 'Determination of K_S^0 Efficiency Systematics'. *BESIII internal memo* **138**, 1–26 (2014).
97. Rong, G. *et al.* 'Measurements of Branching Fractions and Hadronic Form Factors for $D^0 \rightarrow K^- e^+ \nu_e$ and $D^0 \rightarrow \pi^- e^+ \nu_e$ Decays'. *BESIII internal memo* **71** (2014).
98. Gradl, W. & Weidenkaff, P. 'Λ track reconstruction efficiency for Monte-Carlo and data using $J/\Psi \rightarrow \Lambda\bar{\Lambda}$ decays'. *BESIII internal memo* **144**, 1–21 (2012).
99. Aubert, B. *et al.* 'Study of $e^+e^- \rightarrow \Lambda\bar{\Lambda}, \Lambda\bar{\Sigma}^0, \Sigma^0\bar{\Sigma}^0$ using Initial State Radiation with BABAR'. *Physical Review D* **76**, 092006 (2007).
100. Ablikim, M. *et al.* 'Study of J/Ψ decays to $\Lambda\bar{\Lambda}$ and $\Sigma^0\bar{\Sigma}^0$ '. *Physics Letters B* **632**, 181–186 (2006).
101. Gaiser, J. E. *Charmonium Spectroscopy from Radiative Decays of the J/Ψ and Ψ'* PhD thesis (Stanford University, 1982).
102. Ablikim, M. *et al.* 'Determination of the number of J/Ψ events with $J/\Psi \rightarrow$ inclusive decays'. *Chinese Physics C* **36**, 915–925 (2012).